



저작자표시-비영리-변경금지 2.0 대한민국

이용자는 아래의 조건을 따르는 경우에 한하여 자유롭게

- 이 저작물을 복제, 배포, 전송, 전시, 공연 및 방송할 수 있습니다.

다음과 같은 조건을 따라야 합니다:



저작자표시. 귀하는 원저작자를 표시하여야 합니다.



비영리. 귀하는 이 저작물을 영리 목적으로 이용할 수 없습니다.



변경금지. 귀하는 이 저작물을 개작, 변형 또는 가공할 수 없습니다.

- 귀하는, 이 저작물의 재이용이나 배포의 경우, 이 저작물에 적용된 이용허락조건을 명확하게 나타내어야 합니다.
- 저작권자로부터 별도의 허가를 받으면 이러한 조건들은 적용되지 않습니다.

저작권법에 따른 이용자의 권리는 위의 내용에 의하여 영향을 받지 않습니다.

이것은 [이용허락규약\(Legal Code\)](#)을 이해하기 쉽게 요약한 것입니다.

[Disclaimer](#)

공학석사학위논문

Stable, non-Reflective Condition of Perfectly Matched Layer in Computational Aeroacoustics

전산공력음향학에서 Perfectly Matched Layer의
안정적인 흡수조건에 관한 연구

2016 년 2 월

서울대학교 대학원

기계항공공학부

정한아침

Stable, non-Reflective Condition of Perfectly Matched Layer in Computational Aeroacoustics

Hanahchim Choung

Department of Aerospace Engineering

Seoul National University

Abstract

In Computational Aeroacoustics, non-reflective boundary conditions such as radiation or absorbing boundary conditions are critical issues in that they can affect the whole solutions of computation. Among these types of boundary conditions, Perfectly Matched Layer boundary condition which has been widely used in Computational Electromagnetics and Computational Aeroacoustics is developed by augmenting the additional term by an absorption function in the original governing equations so as to stably absorb the outgoing waves. Even if Perfectly Matched Layer is perfectly non-reflective boundary condition analytically, spurious waves at the interface or instability could be shown since the analysis is performed in the discretized space. Hence, the study is focused on factors that affect these numerical instability and accuracy with particular numerical schemes. First, stability analysis preserving the dispersion relation is carried out in order to achieve the stability limit of time-step size. Then, through mathematical approach, stable absorption coefficient and PML width are suggested. In order to validate the prediction of analysis condition, numerical simulations are performed in generalized coordinate system as well as Cartesian coordinate system.

Keyword: High-order Finite Difference, Dispersion-Relation, Stability Analysis,
Computational Aeroacoustics, Perfectly Matched Layer

Student Number : 2014-20665

Contents

Abstract.....	I
Contents	III
List of Tables	V
List of Figures	VI
Nomenclature.....	VIII
Chapter 1. Introduction.....	1
1.1 BACKGROUND	1
1.2 MOTIVATION.....	2
1.3 SCOPE OF PRESENT STUDY	3
Chapter 2. Governing Equations.....	5
2.1 LINEARIZED EULER EQUATIONS.....	5
2.2 DERIVATION OF PML EQUATIONS.....	6
2.2.1 Complex Change of Variables	6
2.2.2 Space-time Transformation	7
2.2.3 Stable PML Equations	9
Chapter 3. Numerical methodology	14
3.1 OPTIMIZED NUMERICAL METHOD	14
3.1.1 Fourier Analysis of High-order Spatial Discretization.....	14
3.1.2 Optimized Time Discretization Scheme	17
3.2 NUMERICAL STABILITY ANALYSIS.....	19

Chapter 4. Non-Reflective PML Conditions	24
4.1 END CONDITION OF PML BOUNDARY	24
4.2 ANALYTICAL APPROACH ON ABSORPTION COEFFICIENT	28
<i>4.2.1 Maximum Absorption Coefficient</i>	<i>28</i>
<i>4.2.2 Minimum Absorption Coefficient</i>	<i>34</i>
Chapter 5. Numerical Tests	38
5.1 STABILITY ANALYSIS RESULTS.....	39
<i>5.1.1 Sound Propagating in Low Mach number Uniform Flow</i>	<i>40</i>
<i>5.1.2 Sound Propagating in High Mach number Uniform Flow</i>	<i>40</i>
5.2 ACCURACY ANALYSIS RESULTS	42
<i>5.2.1 Sound Propagating in Cartesian Grid System</i>	<i>42</i>
<i>5.2.2 Sound Propagating in Curvilinear Grid System.....</i>	<i>44</i>
Chapter 6. Concluding Remarks	51
References	52
Abstract in Korean	56

List of Tables

Table 1 Values of $k_c^* \Delta x$ and $k_{max}^* \Delta x$ of central DRP scheme for different stencils.

Table 2 Optimum PML conditions for various profiles, $\Gamma(x)$.

List of Figures

Fig. 2. 1 The relationship between ω and kx for various modes of ky without mean flow

Fig. 2. 2 The relationship between ω and kx for various modes of ky with mean flow : no transformation (a) and space-time transformed (b)

Fig. 2. 3 Cartesian computational domain governed by the linearized Euler equations enclosed by PMLs

Fig. 3. 1 $k\Delta x$ versus $k * \Delta x$: —, 7-point; ---, 9-point; — — —, 11-point; - - -, 13-point; - - - 15-point stencil.

Fig. 3. 2 (a) Dissipation and (b) dispersion errors of optimized fourth-order multi-step.

Fig. 3. 3 Region of stability in the complex plane.

Fig. 3. 4 Maximum stable absorption coefficients with respect to mean flow.

Fig. 4. 1 Schematic diagram of 7-point central (upper) and upwind (lower) stencils located in the PML region

Fig. 4. 2 The evolution of pressure error at the point (A), (a) and (B), (b)

Fig. 4. 3 An illustration of stencils to be used for derivatives near the interface.

Fig. 4. 4 Wavenumber errors (ϵ) for linear (a), square (b), cubic (c) and quartic (d) absorption profiles.

Fig. 4. 5 The maximum absorption coefficients.

Fig. 4. 6 Pressure value at the end point of the PML domain for linear (a), square (b), cubic (c) and quartic (d) absorption profiles.

Fig. 4. 7 The minimum absorption coefficients.

Fig. 5. 1 Region of stability in the complex plane.

Fig. 5. 2 Pressure contours of case 1 (a) and case 2 (b).

Fig. 5. 3 Pressure contours of case 3 (a) and case 4 (b).

Fig. 5. 4 Contours of the pressure component with the square PML profiles at levels

$\pm 0.1, \pm 0.05$, and ± 0.003 . For figures correspond to the PML conditions of $\sigma = 1.3$ (a), $\sigma = 1.6$ (b), $\sigma = 1.0$ (c) with $D = 13\Delta x$ and $\sigma = 1.3$ with $D = 10\Delta x$ (d).

Fig. 5. 5 Root mean square error (RMSE) of a Cartesian grid for square PML profiles at (49,0).

Fig. 5. 6 A curvilinear grid structure with boundary conditions.

Fig. 5. 7 Contours of the pressure component with the square PML profiles at levels $\pm 0.1, \pm 0.05$, and ± 0.003 . For figures correspond to the PML conditions of $\sigma = 1.3$ (a), $\sigma = 1.6$ (b), $\sigma = 1.0$ (c) with $D = 13\Delta x$ and $\sigma = 1.3$ with $D = 10\Delta x$ (d).

Fig. 5. 8 Root mean square error (RMSE) of pressure in a curvilinear grid for square PML profile at (122,0).

Fig. 5. 9 Contours of the sinusoidal wave propagation with the square PML profiles at levels $\pm 1.0, \pm 0.5, \pm 0.1$, and ± 0.05 .

Fig. 5. 10 Solutions of the scattered acoustic field along the line at $y=0$.

Nomenclature

➤ English

a_j, b_j	optimized stencils
\mathbf{A}, \mathbf{B}	non-conservative matrix of variables
D	PML width
f	solution in the physical domain
$\bar{\mathbf{E}}, \bar{\mathbf{F}}, \bar{\mathbf{H}}$	conservative matrix of variables
J	Jacobian matrix
k_x	wavenumber in x-direction
l	grid point
M_0	Mach number of free stream
n	power of absorption function
p	acoustic pressure
p_0	normalized ambient pressure
p_{pml}	exact solution of PML equations
\mathbf{q}	auxiliary variables inside the PML domain
r	radial coordinate
\mathbf{U}	matrix of physical variables
u, v	particle velocity in 2-dimensional space
(x, y)	Cartesian coordinates

➤ **Greeks**

$\alpha\Delta x$	wavenumber
$\alpha^*\Delta x$	effective wavenumber
β	amplitude of oscillation
γ	specific heat ratio
$\Gamma(x)$	absorption profile
δ_0, δ_l	first and last grid point of the PML region
Δ	increment
ε	error
λ	Eigen value
(ξ, η)	general coordinates
ρ_0	normalized ambient density
σ_x, σ_y	absorption function
$\tilde{\sigma}$	absorption coefficient
φ	solution in the PML region
ω	angular frequency (rad/s)
Ω	angular frequency of source (rad/s)

➤ **Superscripts**

- ~ Fourier-Laplace transformed quantity or indicator of absorption coefficient
- space-time transformation
- ^ transformed value by Complex change of variables
- * corresponding value of effective wavenumber

➤ **Subscripts**

- i, j grid indices in directions of a coordinate
- x, y space derivatives of Cartesian coordinate system
- ξ, η space derivatives of general coordinate system
- c critical value
- max maximum value
- min minimum value
- opt optimum value
- ref reference value
- 0 free stream value or initial values

Chapter 1. Introduction

1.1 Background

Computational aeroacoustics (CAA) is a numerical approach to the problems of aeroacoustics. Even though aeroacoustics includes miscellaneous research topics, the essential components of interest are all generated from the intrinsically unsteady interactions of different scales in the fluid itself (e.g., turbulence and instability waves) or unsteady fluid-boundary interactions. Thus, it is important to understand the complicated mechanism of sound generation, propagation, interaction with bodies, and radiation.

In contrast to computational fluid dynamics (CFD), with its long history and rapid development, CAA has only recently emerged as a separate area of computational approaches, in that the physics of acoustics should be focused on isotropic, nondispersive, and nondissipative characteristics. However, since these are not of primary interest in CFD, its schemes are dispersive, anisotropic, and sometimes highly dissipative. Since numerical dissipation and dispersion are the two primary sources of error in CAA, classical CFD schemes have been found to be unsatisfactory for the study of wave propagation over long distances and large time intervals [1]. CFD schemes, such as the MacCormack [2] scheme, upwind schemes [3, 4], and essentially non-oscillatory schemes [5–7], have been extended to high orders by using more stencil points for application to acoustic problems. In addition to the conventional finite-difference and finite-volume schemes, finite element [8, 9] and spectral methods [10] have been developed for CAA. Recent studies on CAA have been focused on nondissipation and nondispersion, which are desirable for linear wave propagation. Typically, compact and noncompact high-order schemes, such as Lele's schemes [11] and dispersion-relation-preserving (DRP) schemes by Tam and Webb [12], have been developed for CAA studies.

1.2 Motivation

Solving non-reflective boundary problems remains an important issue because they are often attributed as the major source of numerical errors in practical computations. Moreover, as the accuracy of spatial and temporal discretization increases, the need for greater accuracy at the boundaries increases accordingly. In this study, numerical stability analysis of a non-reflective boundary based on perfectly matched layers (PML) will be introduced. Since Berenger [13] first introduced a new absorbing boundary condition, which is the split version of the PML equation in computational electromagnetics, much research has been carried out for the PML equation [14–16]. Unfortunately, those formulations entail exponentially growing solutions in computational aeroacoustics, in which the mean flow that induces discrepancy of the group and phase velocities exists. According to the wave propagation theory [17], group and phase velocities are governed by the dispersion relation, a relation between the angular frequency of the waves and the wave numbers of the spatial variables. Hu [18] succeeded in constructing a stable PML formulation, with a parallel uniform mean flow, by the space-time transformation, which organized the phase and group velocity to be consistent. In [18], he addressed both the stability and the issue of well-posedness so that the PML formulation is analytically stable for the linearized Euler equation. The formulation of the PML was also extended to arbitrary nonuniform mean flow by a parameter study [19] and the spectral collocation method [20], which gives a unique space-time transformation. Recently, many issues related to the PML formulation, on which wave propagation in anisotropic media [21, 22], oblique flow [23, 24], and nonlinear wave [25] depend, have been treated.

The conventional stability issues, however, have been limited to an analytical formulation of the PML equation. Since that equation is only reflectionless or stable for exact solutions, the analytical perfection of the PML equation is no longer valid once the PML equation becomes an approximated form of a discretized equation, which is liable to be unstable. Thus, temporal and spatial discretization schemes should be considered,

in addition to the stable analytical form of the PML equation. For numerical stability, it is important that the parameter be set to the proper numerical range so that the spurious solutions are all heavily damped [12]. However, it is not immediately clear if the conventional stability analysis for linearized Euler equation still works on the PML equation. Since that equation is derived by a complex change of variables, the dispersion relation changes accordingly. While conventional stability analysis focuses solely on the real root of the dispersion relation, now we must consider the complex root to achieve stability of the PML equation, because a complex change of variables forces the dispersion relation of the PML equation to bear the imaginary part. This is why it is necessary to find a new stability criteria for the PML equation that preserves the dispersion relation.

1.3 Scope of Present Study

The main objective of this study is to illuminate the conditions needed to achieve both stability and accuracy of the PML condition. In terms of stability analysis, how the DRP stability criteria of the PML equation can be determined by a numerical scheme, so that the proper time step size as the absorption coefficient and Mach number change is determined analytically, will be presented. The choice of the time step is an important issue since it is directly related to the memory storage problem, where large memory is expected, especially for 3-D problems.

When it comes to the accuracy of the PML, We assume there are two possible factors that generate spurious reflected waves that affect the accuracy. One is that an incident wave entering the PML domain decays so drastic that the numerical scheme cannot preserve the dispersion relation and the other reason is the wave is not sufficiently damped at the endpoint of the PML. From this point of view, the optimum PML width that is sufficient to absorb the solution and its corresponding absorption coefficient is suggested. From this point of view, the optimum PML width that is sufficient to absorb

the solution and its corresponding absorption coefficient will be suggested. Compared with the fact that most previous studies have been done in the context of a parameter study to determine the proper the PML width (or profiles) and its corresponding absorption coefficient in the PML domain, this work has a point in that the factors that affect the accuracy of the PML are illuminated, and proper computational conditions are suggested for more efficient computation in the PML domain. The research is also extended to a generalized coordinate system, as well as Cartesian coordinates, in order to confirm that the criteria are still satisfactory in the PML region with a curvilinear grid.

This paper is organized as follows: In chapter 2, PML equations [18] from linearized Euler equations are elaborately derived in both Cartesian and generalized coordinate systems. In chapter 3, an explicit high-order optimized spatial discretization scheme and two different temporal discretization schemes are briefly reviewed. Then, a numerical stability analysis of the optimized scheme is conducted so as to discover the stability criteria of the PML that has complex eigenvalues. In chapter 4, a boundary closing issue is introduced, in order to apply the isotropic spatial scheme at the end of the PML region. In addition, the optimum PML width that is sufficient to absorb the solution and its corresponding absorption coefficient are discussed. Finally, in chapter 5, numerical examples are reported that demonstrate the validity of the prediction of the analysis condition. Concluding remarks are attached at the last part.

Chapter 2. Governing Equations

2.1 Linearized Euler Equations

For small-amplitude disturbances superimposed on a uniform mean flow of density ρ_0 , pressure p_0 , and velocity M in the x -direction. By assuming that the physical variables are a small, unsteady perturbation, the conventional linearized Euler equations (LEE) normalized by space $\Delta x, \Delta y$ and the speed of sound c for two-dimensional disturbances can be written as follows:

$$\frac{\partial \mathbf{U}}{\partial t} + \frac{\partial \mathbf{E}}{\partial x} + \frac{\partial \mathbf{F}}{\partial y} = 0, \quad (2.1)$$

where

$$\mathbf{U} = \begin{pmatrix} \rho \\ u \\ v \\ p \end{pmatrix}, \quad \mathbf{E} = \begin{pmatrix} \rho_0 u + \rho M \\ Mu + \frac{p}{\rho_0} \\ M_0 v \\ Mp + \gamma p_0 u \end{pmatrix}, \quad \text{and} \quad \mathbf{F} = \begin{pmatrix} \rho_0 v \\ 0 \\ \frac{p}{\rho_0} \\ \gamma p_0 v \end{pmatrix}. \quad (2.2)$$

The vector \mathbf{U} represents the physical variables of the solution vector. By introducing a general coordinate transformation $(x, y, t) \rightarrow (\xi, \eta, \tau)$, the LEEs are given by:

$$\frac{\partial \bar{\mathbf{U}}}{\partial \tau} + \frac{\partial \bar{\mathbf{E}}}{\partial \xi} + \frac{\partial \bar{\mathbf{F}}}{\partial \eta} = 0, \quad (2.3)$$

where

$$\bar{\mathbf{U}} = \frac{\mathbf{U}}{j}, \quad \bar{\mathbf{E}} = \frac{1}{j} [\xi_t \mathbf{U} + \xi_x \mathbf{E} + \xi_y \mathbf{F}], \quad \text{and} \quad \bar{\mathbf{F}} = \frac{1}{j} [\eta_t \mathbf{U} + \eta_x \mathbf{E} + \eta_y \mathbf{F}]. \quad (2.4)$$

After taking the Fourier-Laplace transform $\tilde{f}(k_x, k_y, \omega)$ of a function $f(x, y, t)$ on Eq. (2.1), and organizing the transformed equation into a system of linear algebraic equations, we can calculate the eigenvalues, from which the well-known dispersion relations for LEEs are derived. The dispersion relations for plane waves of the form $\mathbf{u}_0 e^{i(k_x x + k_y y - \omega t)}$ are

$$(\omega - Mk_x)^2 - k_x^2 - k_y^2 = 0 \quad (2.5)$$

for the acoustic waves, and

$$\omega - Mk_x = 0 \quad (2.6)$$

for the vorticity and entropy waves.

2.2 Derivation of PML Equations

2.2.1 Complex Change of Variables

In this research, the PML equations constructed by a complex change of variables [27, 28] are used. If we consider only the x-direction, the complex change of variable is defined as:

$$x \rightarrow \hat{x} + \frac{i}{\omega} \int_{\hat{x}_0}^{\hat{x}} \sigma_{\hat{x}} d\hat{x}, \quad (2.7)$$

where σ is the absorption function, which is always positive, and x_0 is located at the interface of the Euler and the PML domains. Since it is known that the wave is a function of $e^{i(k_x x - \omega t)}$, under a complex change of variables (Eq. (2.7)), and expressing \bar{x} in terms of the original variable x , it becomes

$$e^{i(k_x x - \omega t)} e^{-\frac{k_x}{\omega} \int_{x_0}^x \sigma_x dx}. \quad (2.8)$$

Thus, this augmented factor $e^{-\frac{k_x}{\omega} \int_{x_0}^x \sigma_x dx}$ plays the role of exponentially damping the wave in the PML zone. In order to reduce the amplitude of the wave in the PML region, k_x/ω and $\int_{x_0}^x \sigma_x dx$ must have the same sign. Here, the sign of $\int_{x_0}^x \sigma_x dx$ is determined by the direction of propagation. Since the direction of propagation of a dispersive wave is the same as that of group velocity, the necessary condition can be expressed as

$$\frac{k_x}{\omega} \frac{d\omega}{dk_x} > 0. \quad (2.9)$$

or equivalently,

$$\frac{\omega}{k_x} \frac{d\omega}{dk_x} > 0. \quad (2.10)$$

That is, the phase velocity (ω/k_x) and group velocity ($d\omega/dk_x$) must be consistent and in the same direction. Otherwise, any wave that propagates into the PML equations will diverge when its phase and group velocities are not in the same direction. Hence, when deriving the PML equation's dispersion relation, a relation between ω and k_x of the spatial variables should be derived.

2.2.2 Space-Time Transformation

From the dispersion relation of Eq. (2.5), the relationship between ω and k_x for various modes of k_y when there is no mean flow is plotted in Fig. 2.1. We can find that ω/k_x and $d\omega/dk_x$ have the same sign for all range of k_x . However, when $M = 0.5$, we can find there is a range in which inconsistent ω/k_x and $d\omega/dk_x$ have different signs in Fig. 2.2(a). Hence, the proper transformation, called the space-time transformation, that allows for a consistency of sign becomes inevitable [18].

The general form of the space-time transformation is expressed as

$$t \rightarrow \bar{t} - \beta x. \quad (2.11)$$

When the solution is a function of $e^{i(k_x x - \omega t)}$, in wavenumber space, Eq. (2.11) can be expressed as

$$\begin{aligned} \omega &\rightarrow \bar{\omega}. \\ k_x &\rightarrow \bar{k}_x - \beta \omega. \end{aligned} \quad (2.12)$$

From [16, 29, 30], β is defined as

$$\beta = \frac{M}{1 - M^2} \quad (2.13)$$

for uniform mean flow.

In Fig. 2.2(b), the relationship between transformed $\bar{\omega}$ and \bar{k}_x for various modes of k_y are plotted with $M = 0.5$. Compared to Fig. 2.1(a), there is no range where inconsistent ω/k_x and $d\omega/dk_x$ values have different signs. The dispersion relation

of the vorticity and entropy waves are not considered since they unconditionally satisfy Eq. (2.10) in the presence of parallel uniform mean flow.

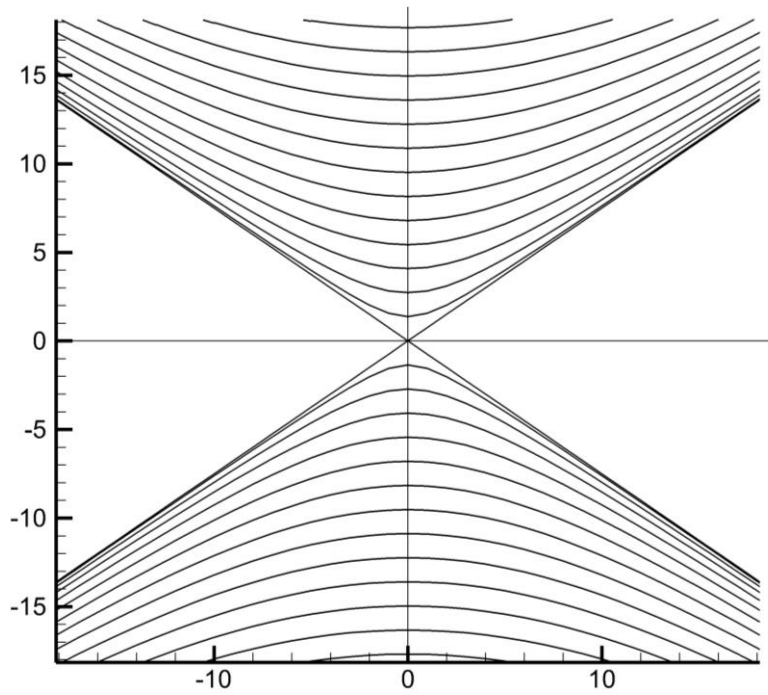


Fig. 2. 1 The relationship between ω and k_x for various modes of k_y without mean flow

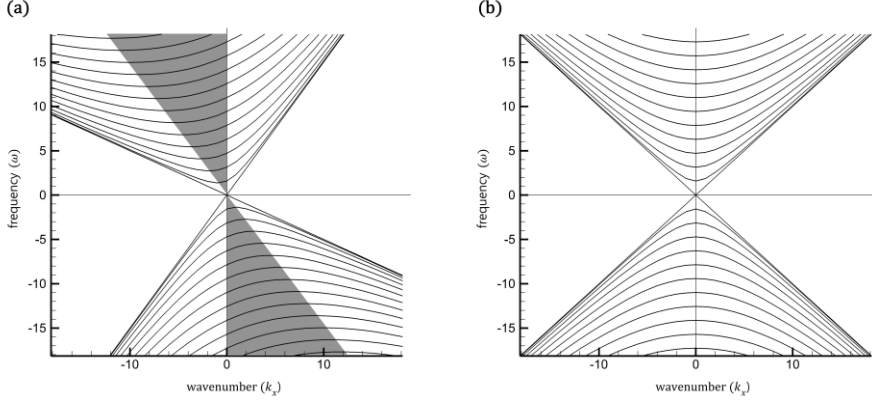


Fig. 2. 2 The relationship between ω and k_x for various modes of k_y with mean flow : no transformation (a) and space-time transformed (b)

2.2.3 Stable PML equations

The LEE in Eq. (2.1) can also be expressed in a non-conservative form as:

$$\frac{\partial \mathbf{U}}{\partial t} + \mathbf{A} \frac{\partial \mathbf{U}}{\partial x} + \mathbf{B} \frac{\partial \mathbf{U}}{\partial y} = \mathbf{0}, \quad (2.14)$$

where

$$\mathbf{A} = \begin{pmatrix} M_0 & \rho_0 & 0 & 0 \\ 0 & M_0 & 0 & 1/\rho_0 \\ 0 & 0 & M_0 & 0 \\ 0 & \gamma p_0 & 0 & M_0 \end{pmatrix} \text{ and } \mathbf{B} = \begin{pmatrix} 0 & 0 & \rho_0 & 0 \\ 0 & 0 & 0 & 0 \\ 0 & 0 & 0 & 1/\rho_0 \\ 0 & 0 & \gamma p_0 & 0 \end{pmatrix}. \quad (2.15)$$

From the complex change of variables, the complex term with the absorption function is added to the spatial variables. The partial derivatives of \hat{x} with respect to the original variables can be obtained from Eq. (2.7) as:

$$\frac{\partial \hat{x}}{\partial x} = \frac{1}{\left(1 + \frac{i}{\omega} \sigma_{\hat{x}}\right)}, \quad \frac{\partial \hat{x}}{\partial y} = 0, \text{ and } \frac{\partial \hat{x}}{\partial t} = 0. \quad (2.16)$$

Using a similar approach in the y-direction,

$$\frac{\partial \hat{y}}{\partial x} = 0, \quad \frac{\partial \hat{y}}{\partial y} = \frac{1}{\left(1 + \frac{i}{\omega} \sigma_{\hat{y}}\right)}, \text{ and } \frac{\partial \hat{y}}{\partial t} = 0. \quad (2.17)$$

The partial derivatives of \bar{t} by space-time transformation Eq. (2.11) can also be expressed as

$$\frac{\partial \bar{t}}{\partial x} = \beta, \quad \frac{\partial \bar{t}}{\partial y} = 0, \text{ and } \frac{\partial \bar{t}}{\partial t} = 1. \quad (2.18)$$

When the total derivative of the solution vector is

$$\begin{aligned} \frac{\partial \mathbf{U}}{\partial x} &= \frac{\partial \mathbf{U}}{\partial \hat{x}} \frac{\partial \hat{x}}{\partial x} + \frac{\partial \mathbf{U}}{\partial \hat{y}} \frac{\partial \hat{y}}{\partial x} + \frac{\partial \mathbf{U}}{\partial \bar{t}} \frac{\partial \bar{t}}{\partial x}, \\ \frac{\partial \mathbf{U}}{\partial y} &= \frac{\partial \mathbf{U}}{\partial \hat{x}} \frac{\partial \hat{x}}{\partial y} + \frac{\partial \mathbf{U}}{\partial \hat{y}} \frac{\partial \hat{y}}{\partial y} + \frac{\partial \mathbf{U}}{\partial \bar{t}} \frac{\partial \bar{t}}{\partial y}, \\ \frac{\partial \mathbf{U}}{\partial t} &= \frac{\partial \mathbf{U}}{\partial \hat{x}} \frac{\partial \hat{x}}{\partial t} + \frac{\partial \mathbf{U}}{\partial \hat{y}} \frac{\partial \hat{y}}{\partial t} + \frac{\partial \mathbf{U}}{\partial \bar{t}} \frac{\partial \bar{t}}{\partial t}, \end{aligned} \quad (2.19)$$

by replacing Eq. (19) into the non-conservative form of the LEE (Eq. (14)), it becomes

$$\frac{\partial \mathbf{U}}{\partial \bar{t}} + \mathbf{A} \left(\frac{1}{\left(1 + \frac{i}{\omega} \sigma_{\hat{x}}\right)} \frac{\partial \mathbf{U}}{\partial \hat{x}} + \beta \frac{\partial \mathbf{U}}{\partial \bar{t}} \right) + \mathbf{B} \left(\frac{1}{\left(1 + \frac{i}{\omega} \sigma_{\hat{y}}\right)} \frac{\partial \mathbf{U}}{\partial \hat{y}} \right) = \mathbf{0}. \quad (2.20)$$

After multiplying Eq. (20) by $(1 + i/\omega\sigma_{\hat{x}})(1 + i/\omega\sigma_{\hat{y}})$, and performing some simple calculations in the frequency domain, it is modified to be

$$\begin{aligned} (\mathbf{I} + \beta \mathbf{A}) \left[\frac{\partial \mathbf{U}}{\partial \bar{t}} + (\sigma_{\hat{x}} + \sigma_{\hat{y}}) \mathbf{U} + \sigma_{\hat{x}} \sigma_{\hat{y}} \mathbf{q} \right] + \mathbf{A} \left(\frac{\partial \mathbf{U}}{\partial \hat{x}} + \sigma_{\hat{y}} \frac{\partial \mathbf{q}}{\partial \hat{x}} \right) \\ + \mathbf{B} \left(\frac{\partial \mathbf{U}}{\partial \hat{y}} + \sigma_{\hat{x}} \frac{\partial \mathbf{q}}{\partial \hat{y}} \right) = \mathbf{0}, \text{ and} \end{aligned} \quad (2.21)$$

$$\frac{\partial \mathbf{q}}{\partial t} = \mathbf{U}, \quad (2.22)$$

where \mathbf{q} is the only auxiliary variable needed inside the PML domain.

Finally, by denoting the changed variables to the original variables, and replacing the transformed variables with the original variables, the stable PML equation is expressed as:

$$\begin{aligned} \frac{\partial \mathbf{U}}{\partial t} + \mathbf{A} \frac{\partial \mathbf{U}}{\partial x} + \mathbf{B} \frac{\partial \mathbf{U}}{\partial y} + \sigma_y \mathbf{A} \frac{\partial \mathbf{q}}{\partial x} + \sigma_x \mathbf{B} \frac{\partial \mathbf{q}}{\partial y} + (\sigma_x + \sigma_y) \mathbf{U} + \sigma_x \sigma_y \mathbf{q} \\ + \sigma_x \beta \mathbf{A} (\mathbf{U} + \sigma_y \mathbf{q}) = \mathbf{0}. \end{aligned} \quad (2.23)$$

Cartesian computational domain with PML regions is illustrated in Fig 2.3.

In generalized coordinates, $(x, y, t) \rightarrow (\xi, \eta, \tau)$, the conservative form of the PML equations for uniform mean flow takes the following form:

$$\frac{\partial \bar{\mathbf{U}}}{\partial \tau} + \frac{\partial \bar{\mathbf{E}}}{\partial \xi} + \frac{\partial \bar{\mathbf{F}}}{\partial \eta} + \bar{\mathbf{H}} = 0, \quad (2.24)$$

where

$$\bar{\mathbf{U}} = \frac{\mathbf{U}}{J}, \quad \bar{\mathbf{E}} = \frac{1}{J} \begin{bmatrix} \xi_x (M_0 \rho + u + \sigma_\eta (M_0 q_\rho + q_u)) + \xi_y (v + \sigma_\eta q_v) \\ \xi_x (M_0 u + p + \sigma_\eta (M_0 q_u + q_p)) + \xi_y (v + \sigma_\xi q_v) \\ \xi_x (M_0 v + u + \sigma_\eta (M_0 q_v + q_u)) + \xi_y (p + \sigma_\eta q_p) \\ \xi_x (M_0 p + u + \sigma_\eta (M_0 q_p + q_u)) + \xi_y (v + \sigma_\eta q_v) \end{bmatrix},$$

$$\bar{\mathbf{F}} = \frac{1}{J} \begin{bmatrix} \eta_x (M_0 \rho + u + \sigma_\xi (M_0 q_\rho + q_u)) + \eta_y (v + \sigma_\xi q_v) \\ \eta_x (M_0 u + p + \sigma_\xi (M_0 q_u + q_p)) + \xi_y (v + \sigma_\xi q_v) \\ \eta_x (M_0 v + u + \sigma_\xi (M_0 q_v + q_u)) + \eta_y (p + \sigma_\xi q_p) \\ \eta_x (M_0 p + u + \sigma_\xi (M_0 q_p + q_u)) + \eta_y (v + \sigma_\xi q_v) \end{bmatrix}, \text{ and} \quad (2.25)$$

$$\bar{\mathbf{H}} = \frac{1}{J} \begin{bmatrix} (\sigma_\xi + \sigma_\eta) \rho + \sigma_\xi \sigma_\eta q_\rho + \beta \sigma_\xi (M_0 \rho + u + \sigma_\eta (M_0 q_\rho + q_u)) \\ (\sigma_\xi + \sigma_\eta) u + \sigma_\xi \sigma_\eta q_u + \beta \sigma_\xi (M_0 u + p + \sigma_\eta (M_0 q_u + q_p)) \\ (\sigma_\xi + \sigma_\eta) v + \sigma_\xi \sigma_\eta q_v + \beta \sigma_\xi (M_0 v + u + \sigma_\eta (M_0 q_v + q_u)) \\ (\sigma_\xi + \sigma_\eta) p + \sigma_\xi \sigma_\eta q_p + \beta \sigma_\xi (M_0 p + u + \sigma_\eta (M_0 q_p + q_u)) \end{bmatrix}.$$

To obtain the corresponding dispersion relation of the PML equation, the transformed variables should be expressed in wavenumber space first. Since $\partial/\partial x = ik_x$, the complex change of variables in wavenumber space can be written as

$$k_x \rightarrow \frac{k_x}{1 + \frac{i}{\omega} \sigma_x}. \quad (2.26)$$

Using the similar approach in the y-direction,

$$k_y \rightarrow \frac{k_y}{1 + \frac{i}{\omega} \sigma_y}. \quad (2.27)$$

By replacing the space-time transformation in Eq. (2.12) to Eqs. (2.26) and (2.27), we get

$$k_x \rightarrow \frac{k_x}{1 + \frac{i}{\omega} \sigma_x} \left(k_x + \frac{M}{1 - M^2} \omega \right) - \frac{M}{1 - M^2} \omega \text{ and } k_y \rightarrow \frac{k_y}{1 + \frac{i}{\omega} \sigma_y}. \quad (2.28)$$

The dispersion relation for Eq. (2.23) can be found, equivalently, by replacing k_x and k_y in Eq. (2.28), which becomes

$$\begin{aligned} & \frac{(\omega + i\sigma_x)^2 (\omega + i\sigma_y)^2}{(1 - M^2)^2} - (\omega + i\sigma_y)^2 \left(k_x + \frac{M}{1 - M^2} \omega \right)^2 \\ & - \frac{(\omega + i\sigma_x)^2}{1 - M^2} k_y^2 = 0 \end{aligned} \quad (2.29)$$

for the acoustic wave, and

$$\omega + \frac{i\sigma_x}{1 - M^2} - M k_x = 0 \quad (2.30)$$

for the vorticity and entropy waves. It is found that the root of the dispersion relations of the PML equations have complex value. Hence, from Eqs. (2.29) and (2.30), we can confirm that the phase velocity and group velocity are consistent. The details on the stability analysis can be found in [18].

$\sigma_x \neq 0$ $\sigma_y \neq 0$	$\sigma_x = 0,$ $\sigma_y \neq 0$ PML	$\sigma_x \neq 0$ $\sigma_y \neq 0$
$\sigma_x \neq 0$ $\sigma_y = 0$ PML	Linearized Euler Equations	$\sigma_x \neq 0$ $\sigma_y = 0$ PML
$\sigma_x \neq 0$ $\sigma_y \neq 0$	$\sigma_x = 0,$ $\sigma_y \neq 0$ PML	$\sigma_x \neq 0$ $\sigma_y \neq 0$

Fig. 2. 3 Cartesian computational domain governed by the linearized Euler equations enclosed by PMLs

Chapter 3. Numerical Methodology

3.1 Optimized Numerical Method

If the computational scheme and the governing equations have the same dispersion relation, then the numerical and exact solutions will have the same wave propagation characteristics, such as group and phase velocities. Accordingly, the so-called DRP scheme by Tam and Webb [12] has been developed for CAA, which preserves the wave propagation of the governing equations. In this chapter, a fourth-order DRP scheme will be discussed in wavenumber space, and an optimized Adams-Bashford fourth-order time discretization scheme will be reviewed in view of stability. Finally, numerical stability analysis will be introduced to preserve the dispersion relation in the PML equations.

3.1.1 Fourier Analysis of High-order Spatial Discretization

In aeroacoustics problems, what is needed for numerical stability is a finite difference scheme in space that has almost the same dispersion relation as the original partial differential equations [31]. For spatial discretization, we consider an optimized finite difference scheme, one which is broadly used for CAA. The optimized scheme, also known as the dispersion-relation-preserving (DRP) scheme [12], is expressed as:

$$\left(\frac{\partial f}{\partial x}\right)_i \cong \frac{1}{\Delta x} \sum_{j=-N_0}^N a_j f_{i+j}. \quad (3.1)$$

Now, by applying a Fourier transform to the above equation, and making use of the derivative and shifting theorems,

$$k^* \cong \frac{-i}{\Delta x} \sum_{j=-N_0}^N a_j e^{ij\alpha\Delta x} \quad (3.2)$$

where k^* is the effective wavenumber of the partial derivative and a_j is an optimized stencil that can be obtained by minimizing the integrated error E over a certain wave

number range e , where

$$E = \int_0^e |k^* \Delta x - k \Delta x| d(k \Delta x). \quad (3.3)$$

The conditions for E to be at a minimum are,

$$\frac{dE}{db_j} = 0 \quad \text{and } j = 1, 2, 3 \dots, N. \quad (3.4)$$

More optimization methods for the minimization of error can be found in [32, 33]. $N_0 = N$ for the central scheme, and $2N + 1$ is the number of stencils to be used. In Eq. (3.2), k^* represents the effective wavenumber. The maximum k^* the scheme can preserve depends on N , and the computational cost rises dramatically as the stencil size gets larger. Fig. 3.1 shows the effective wavenumbers ($k^* \Delta x$) versus the wavenumber ($k \Delta x$) of the partial derivative relations for several explicit optimized schemes [34]. A list of the maximum resolvable wavenumber ($k_c^* \Delta x$) and the maximum effective wavenumber ($k_{max}^* \Delta x$) are given in Table 1. $k_c^* \Delta x$ is found using the criterion: $|\alpha^* \Delta x - \alpha \Delta x| < 0.005$, $k_{max}^* \Delta x$ is the extremal value that affects the stability consideration, and $2\pi / \alpha_c^* \Delta x$ is a resolution, i.e., the minimum resolvable grid points per wavelength.

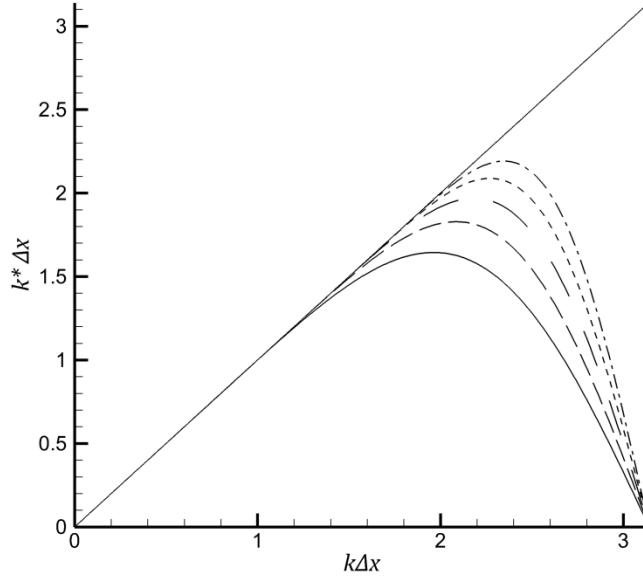


Fig. 3. 1 $k\Delta x$ versus $k^*\Delta x$: —, 7-point; - - -, 9-point; — — —, 11-point; - - -, 13-point; - . - 15-point stencil.

Table 1 Values of $k_c^*\Delta x$ and $k_{max}^*\Delta x$ of central DRP scheme for different stencils

Spatial discretization	$k_c^*\Delta x$	$k_{max}^*\Delta x$	Resolution
7-point	1.16	1.64	5.4
9-point	1.42	1.82	4.4
11-point	1.63	1.97	3.9
13-point	1.80	2.08	3.5
15-point	1.96	2.19	3.2

3.1.2 Optimized Time Discretization Scheme

Since the DRP property is desirable for computing wave propagation problems, we focus on a particular time integration scheme that leads to the DRP property by an optimization process, and then calculate the stability diagram for the complex domain. Here, an optimized four-level time discretization multi-step (Adams–Bashford) method is used as the explicit time marching scheme.

Suppose the time evolution equation is written as

$$\frac{\partial \mathbf{u}}{\partial t} = \mathbf{F}(\mathbf{u}), \quad (3.5)$$

where \mathbf{u} is a vector of physical values and operator \mathbf{F} contains the discretization of the spatial derivatives. The time level is divided uniformly into time step Δt .

If the values of \mathbf{u} and du/dt are known at time $t, t - \Delta t, t - 2\Delta t$, and $t - 3\Delta t$, the four-level finite difference approximation can be written as

$$\mathbf{u}^{n+1} = \mathbf{u}^n + \Delta t \sum_{j=0}^3 b_j \left(\frac{\partial \mathbf{u}}{\partial t} \right)^{n-j}, \quad (3.6)$$

where b_j are constants to be determined for optimization. By applying the Laplace transform and shifting theorem to Eq. (3.6), we obtain:

$$-i \frac{i(e^{-i\omega\Delta t} - 1)}{\Delta t \sum_{j=0}^3 b_j e^{ij\omega\Delta t}} \tilde{\mathbf{u}} \cong \frac{d\tilde{\mathbf{u}}}{dt}. \quad (3.7)$$

Since the Laplace transform of the time derivative of \mathbf{u} is $i\omega\mathbf{u}$, by comparing the two sides of Eq. (3.7), it becomes:

$$\bar{\omega} \cong \frac{i(e^{-i\omega\Delta t} - 1)}{\Delta t \sum_{j=0}^3 b_j e^{ij\omega\Delta t}}, \quad (3.8)$$

where $\bar{\omega}$ is the effective angular frequency of Eq. (3.6). When the weighted integrated error E_w is defined as

$$E_w = \int_{-\zeta}^{\zeta} \{\lambda [Re(\bar{\omega}\Delta t - \omega\Delta t)]^2 + (1 - \lambda) [Im(\bar{\omega}\Delta t - \omega\Delta t)]^2\} d(\omega\Delta t), \quad (3.9)$$

where λ is the weight and ζ is the frequency range, we expect $\bar{\omega}$ to be a good approximation of ω . In order to minimize the weighted integrated error of Eq. (3.9) for a particular b_j , we let

$$\frac{dE_w}{db_j} = 0 \text{ and } j = 0,1,2,3. \quad (3.10)$$

Thus, Eq. (3.10) provides four equations for four coefficients b_j as a function of λ and ζ . Based on a consideration of the range of useful frequencies and numerical damping rate, the values $\lambda = 0.36$ and $\zeta = 0.5$ are recommended. As a result, the optimized values of the coefficients are

$$\begin{aligned} b_0 &= 2.30255809, \quad b_1 = -2.49100760, \\ b_2 &= 1.57434093, \text{ and } b_3 = -0.38589142. \end{aligned} \quad (3.11)$$

3.2 Numerical Stability Analysis

In this chapter, we will perform a stability analysis on the optimized multi-step method in order to find the stability criteria for the PML equations. To analyze the numerical errors, we consider the amplification factor in the wavenumber domain. Applying the model problem to Eq. (3.5) leads to

$$\frac{\partial \mathbf{u}}{\partial t} = \lambda \mathbf{u}, \quad (3.12)$$

where λ is the eigenvalue of the operator $\mathbf{F}(\mathbf{u})$, which can be replaced by $-i\omega$ from the exact solution. If we replace the partial derivative term of Eq. (3.6) with Eq. (3.12), the Eq. (3.6) becomes

$$\mathbf{u}^{n+1} = \mathbf{u}^n - i\omega\Delta t \sum_{j=0}^3 b_j \mathbf{u}^{n-j}. \quad (3.13)$$

Reorganizing the equation (3.13) with respect to amplification factor, $\gamma = \mathbf{u}^{n+1}/\mathbf{u}^n$, it can be written in the form as follows:

$$i \frac{\gamma^4}{\omega\Delta t} - \left(\frac{i}{\omega\Delta t} + b_0 \right) \gamma^3 - b_1 \gamma^2 - b_2 \gamma - b_3 = 0. \quad (3.14)$$

Solving this biquadratic equation, we get four different roots γ_j ($j = 1, 2, 3, 4$), three of which are spurious roots. Since the exact amplification factor is found to be

$$\gamma_e = e^{-i\omega\Delta t}, \quad (3.15)$$

we can compare the numerical and exact amplification factors as

$$\frac{\gamma}{\gamma_e} = \varepsilon e^{i\delta}. \quad (3.16)$$

In this expression, ε represents the dissipation error, which should be 1, and δ is the dispersion error, which should be 0. They are functions of $\omega\Delta t$, and the properties of the scheme are only affected by the coefficients b_j . The dissipation and dispersion errors of the optimized fourth-order multi-step scheme for the real value of $\omega\Delta t$ are plotted in Fig. 3.2.

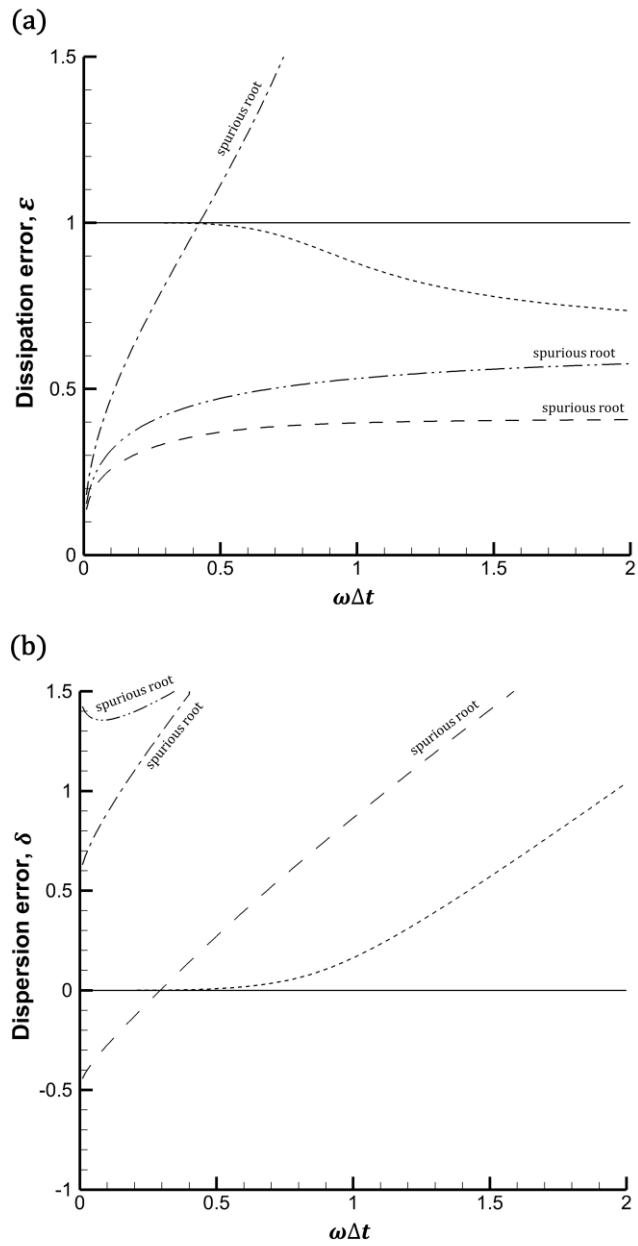


Fig. 3. 2 (a) Dissipation and (b) dispersion errors of optimized fourth-order multi-step.

In the range $\omega\Delta t \leq 0.41$, the dissipation error of all solutions are less than 1, which is called the stability limit. For accuracy, we take the criterion $|\varepsilon - 1| < 0.005$ for dissipation accuracy and $|\delta| < 0.005$ for dispersion accuracy. In the range $\omega\Delta t \leq 0.44$, it is shown that the numerical solution is time-accurate. Hence, we find that the stability limit encompasses the accuracy limit in this case.

However, comparing that the roots of the dispersion relations for the LEEs have only real values of angular frequency, the dispersion relation of the PML equation has complex roots because of the complex change of variables. In case $\omega\Delta t$ is a complex value, we need to consider both real and imaginary parts of the eigenvalue in Eq. (3.12). To include the general case of the stability condition, the stability diagram can be drawn in the complex plane. The stability diagram of the optimized fourth-order multi-step method is numerically calculated for $\omega\Delta t = \text{Re}(\omega\Delta t) + i\text{Im}(\omega\Delta t)$ in Fig. 3.3. Only the negative imaginary part is plotted, since the solution having time dependence of the form $e^{-i\omega\Delta t}$ will diverge in the range $\text{Im}(\omega\Delta t) > 0$.

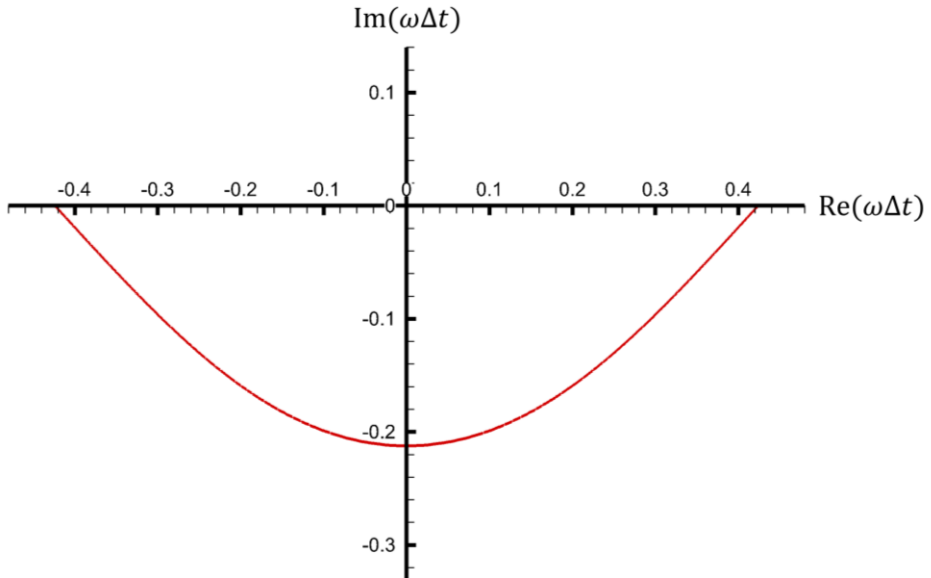


Fig. 3. 3 Region of stability in the complex plane.

From the roots of the dispersion relation of the PML equations in Eq. (2.29), a root that satisfies the condition $\text{Re}(\omega) \geq 0$ is expressed as

$$\omega = \text{Re}(\omega) + i\text{Im}(\omega), \quad (3.17)$$

where the complex value ω becomes a maximum for a given σ_x , σ_y , Δx , Δy , and M when

$$k_x = k_{x,max} \text{ and } k_y = k_{y,max}. \quad (3.18)$$

Thus, the inequality

$$|\omega| \leq \omega_{max}(M, \sigma_{max}, k_{max}, \Delta x, \Delta y) \quad (3.19)$$

holds true. Here, ω_{max} is the maximum physical complex root that qualifies the dispersion relation of the PML equations, which is the function of the Mach number, absorption coefficient, wavenumbers, and grid sizes. By multiplying Δt by the inequality Eq. (3.19), and comparing this with the stability criteria of Fig.3.3, it is straightforward that $\omega_{max}\Delta t$ should be located on the upper side of the stability footprint. This consideration will lead to the condition of determining Δt , not only for the Euler domain, but also for the PML region.

Now we can deduce the relationship between Mach number and maximum absorption coefficient for stability, $\tilde{\sigma}$. Regardless of the profile of absorption function, σ_x or σ_y , the maximum value of it becomes $\sigma_{max} = \tilde{\sigma}(1 - M^2)$ at the end of the PML domain since it smoothly increases. A factor of $(1 - M^2)$ is multiplied since the absorption rate in x-direction is increased by a factor of $1/(1 - M^2)$. For a given Δt , maximum absorption coefficients ($\tilde{\sigma}$) are plotted with respect to Mach number in Fig. 3.4.

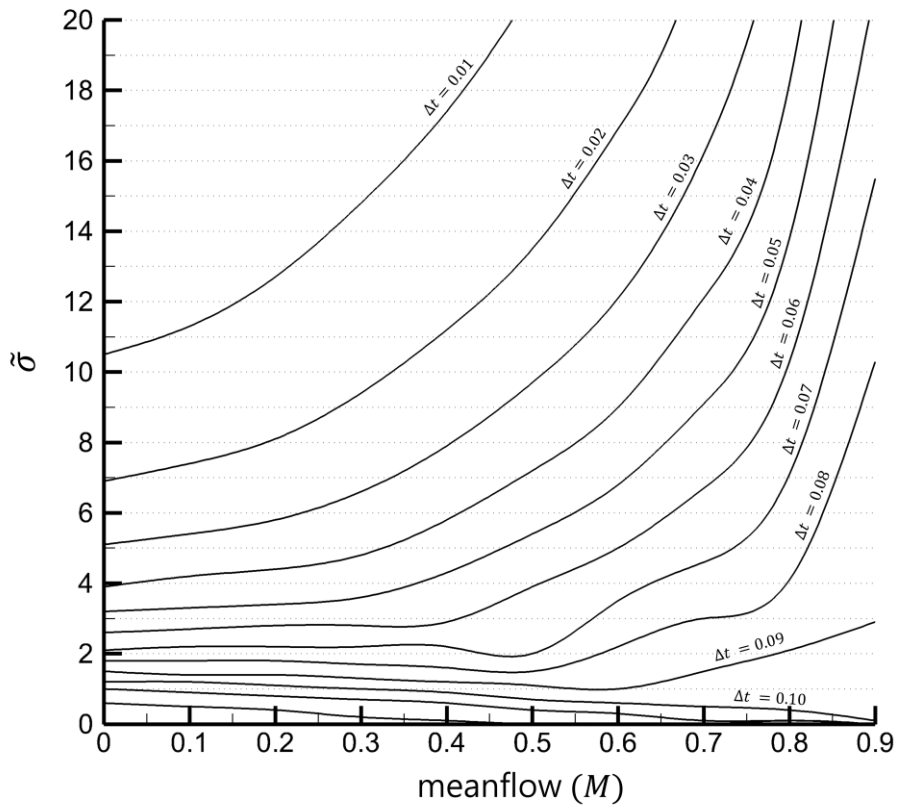


Fig. 3. 4 Maximum stable absorption coefficients with respect to mean flow.

Chapter 4. Non-reflective PML Conditions

4.1 End Condition of PML Boundary

Since there is an apparent discontinuity at the border of the computational domain where the PML region ends, it is inevitable to apply boundary-closure treatment. One way is to use anisotropic schemes [35, 36], which is the method generally adopted for end conditions. In the case of the upwind scheme, however, the imaginary part of the effective wavenumber remains. In the case of a 7-point optimized upwind DRP scheme [4], the imaginary part pertains when $k\Delta x$ is 2.1, which is where $k^*\Delta x$ becomes the maximum wavenumber. Thus, the maximum wavenumber with an imaginary part cannot formulate the inequality $|k^*\Delta x - k\Delta x| < 0.005$ that is necessary for the stability criteria in Fig. 3. Here, we suggest an alternative, so that the stability of the PML is not affected by the imaginary wavenumber of the anisotropic scheme. Since the amount of absorption by the PML in the x-direction is defined as

$$e^{-\int_{x_0}^x \sigma_x dx}, \quad (4.1)$$

the physical value in the PML region will eventually be damped to zero for sufficient PML width. The proper PML width to damp out the solution will be discussed later. If we assume that we provide the proper PML width that makes the value at the endpoint of the PML region to be approximately zero in the numerical calculation, we can say the points after the endpoint are always zero. Actually, this assumption is straightforward because spurious waves would be reflected unless they were sufficiently decayed in the PML region. From this assumption, we can now apply an isotropic scheme at the end of the boundary by setting $(N - 1)/2$ auxiliary null ghost points for an N-point central spatial discretization scheme. The schematic diagrams of the 7-point central and upwind stencils are illustrated in Fig. 4.1. For the conventional way of using the upwind method at the boundary, the stencils stay inside the PML region. In the case of the central stencil,

we set three null-ghost points that have zero values to be extended from the border of the PML region to the outside.

This null-ghost point approach is verified by numerical simulation in the PML region. The following Gaussian pulse, which is $20\Delta x$ away from the PML region, is propagated to the PML:

$$p = \rho = \exp\left[(-\ln 2)\frac{(x - 20)^2 + y^2}{9}\right], u = v = 0. \quad (4.2)$$

In Fig. 4.2, the pressure error of the numerical solution p , and the reference solution p_{ref} , as a function of time is plotted for two selected points located at **(A)** and **(B)** of Fig. 4.1. The pressure error is written as $|p_{ref} - p|$, normalized by p_0 . The reference solution is obtained by using a larger computational domain so that it is not affected by any boundary effects. The absorption function is defined as $\sigma_x = (x/D)^2$ in the PML region, with a width of D . The 7-point DRP central and upwind scheme for the spatial derivatives are used. We find that the pressure error with the central scheme shows even better accuracy than the optimized upwind scheme for both points. This simple but powerful assumption reveals that there is no need to use any other boundary closing treatment, since the acoustic pressure converges into an infinitesimal value at the end of the PML region. Moreover, it reduces the computational cost, since less than $(N + 1)/2$ points are calculated at the endpoints. As a result, by using this approach, we can implement the stability analysis for the PML region without considering the imaginary part of the wavenumber.

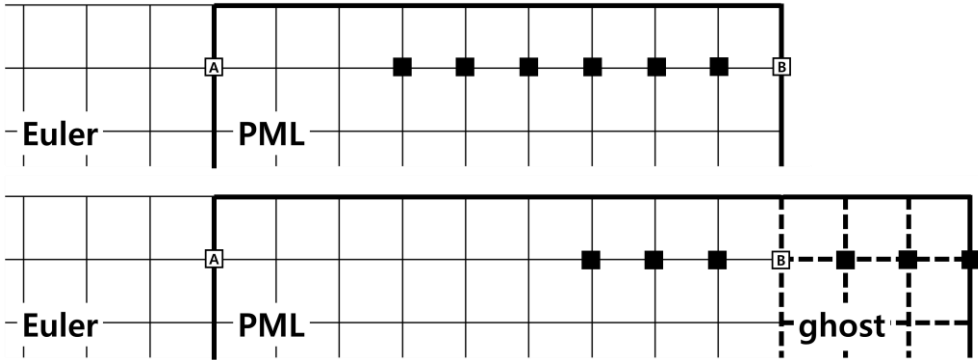


Fig. 4. 1 Schematic diagram of 7-point central (upper) and upwind (lower) stencils located in the PML region

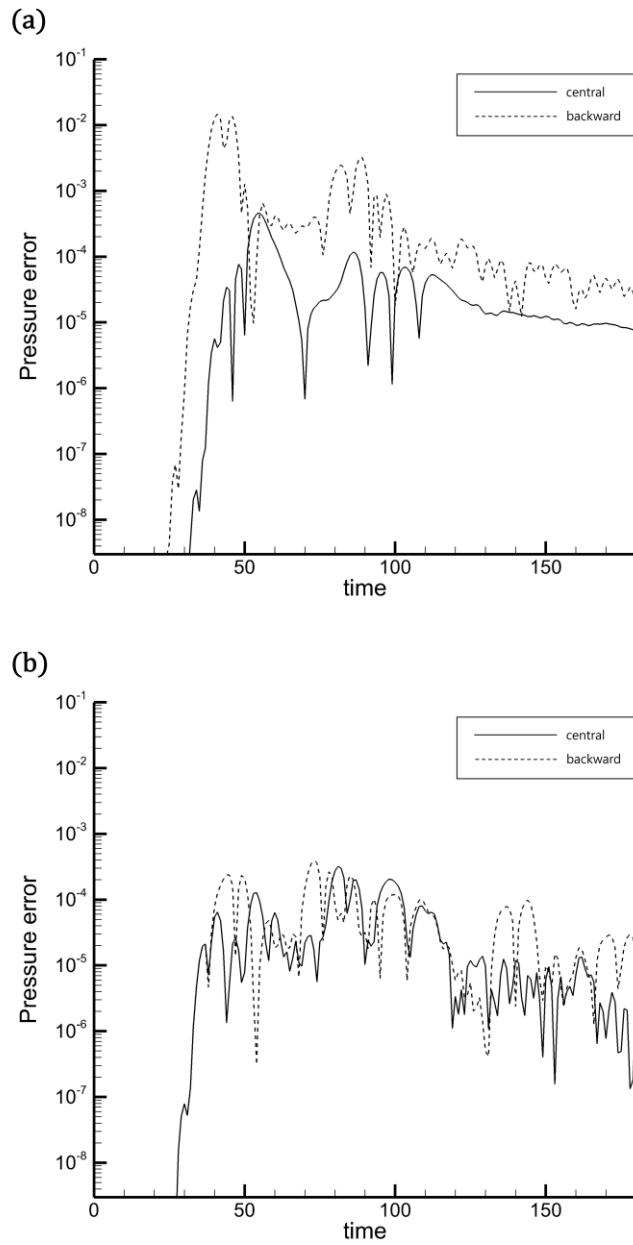


Fig. 4. 2 The evolution of pressure error at the point (A), (a) and (B), (b)

4.2 Analytical Approach on Absorption Coefficient

There are two possible factors that generate spurious reflected waves that affect the accuracy of the PML. One occurs when the decaying rate in the PML domain is too drastic to make the absorption increase smoothly in numerical discretization, and the other occurs when the wave is not sufficiently damped at the endpoint of the PML. From Eq. (2.7), it is shown that the solution in the PML domain is damped by a factor of

$$e^{-\int_{x_0}^x \sigma_x dx}, \quad \sigma_x = \tilde{\sigma}\Gamma(x), \quad (4.3)$$

where $\tilde{\sigma}$ is the absorption coefficient which is a constant value, and $\Gamma(x)$ is the absorption profile. The profile of this absorption function should be such that $\sigma_x(x_0) = \frac{d\sigma_x(x_0)}{dx} = 0$ to be matched at the interface of physical domain and the PML domain.

In this chapter, we will investigate the absorption function that plays an important role in the performance of the PML such that the optimum PML width for the efficiency of computation is determined. There are variety of commonly used absorption profiles such as power-law [37,38] and sine power-law profiles [39] as follows:

$$\Gamma(x) = \left(\frac{x}{D}\right)^n \quad \text{and} \quad \Gamma(x) = \sin^n\left(\frac{\pi}{2D}\right), \quad (4.4)$$

where D is the PML width and n is the positive real value. Thus, we can determine the minimum PML width by appropriate choice of $\tilde{\sigma}$ and n . The power-law profiles are considered in this research for various $\tilde{\sigma}$.

4.2.1 Maximum Absorption Coefficient

Since the Euler equations and the PML equations are different governing equations, they have different analytical solutions. In Fig. 4.3, several points for a 7-point central scheme that use both the Euler and the PML solutions to get partial derivatives are illustrated. If each point is denoted as l , and the solutions to the Euler equations and a set of different solutions to the PML equations with respect to grid point i are f and φ_i , respectively, the gradient at l can be expressed as

$$\left(\frac{\partial \varphi}{\partial x}\right)_l \cong \frac{1}{\Delta x} \left(\sum_{j=-N}^{-l} a_j f_{l+j} + \sum_{j=-l+1}^N a_j \varphi_{l+j} \right), \quad (4.5)$$

where the solution of the PML equations, φ_j , can be analytically expressed as

$$\varphi_j = f_j e^{-\int_0^{j\Delta x} \sigma_{j\Delta x} d(j\Delta x)}. \quad (4.6)$$

By replacing φ_j of Eq. (4.6) into Eq. (4.5),

$$\begin{aligned} \left(\frac{\partial f}{\partial x}\right)_l e^{-\int_0^{l\Delta x} \sigma_{j\Delta x} d(j\Delta x)} \\ \cong \frac{1}{\Delta x} \left(\sum_{j=-N}^{-l} a_j f_{l+j} + \sum_{j=-l+1}^N a_j f_{l+j} e^{-\int_0^{(l+j)\Delta x} \sigma_{j\Delta x} d(j\Delta x)} \right), \end{aligned} \quad (4.7)$$

and applying the Fourier transform,

$$\begin{aligned} i\alpha \tilde{f}(\alpha) &\cong \frac{1}{\Delta x} \left(\sum_{j=-N}^{-l} a_j e^{ij\alpha\Delta x} \right. \\ &\quad \left. + \sum_{j=-l+1}^N a_j e^{ij\alpha\Delta x - \int_0^{(l+j)\Delta x} \sigma_{j\Delta x} d(j\Delta x)} \right) e^{\int_0^{l\Delta x} \sigma_{j\Delta x} d(j\Delta x)} \tilde{f}(\alpha) \\ &\equiv i\alpha_l^* \tilde{f}(\alpha), \end{aligned} \quad (4.8)$$

where α_k^* is denoted as effective wavenumber at grid point k .

In the Euler domain ($\sigma_{j\Delta x} = 0$),

$$\alpha_l^* = \alpha_{l+1}^* = -\frac{i}{\Delta x} \left(\sum_{j=-N}^N a_j e^{ij\alpha\Delta x} \right), \quad (4.9)$$

where, the effective wavenumber is consistent regardless of the positions.

In the PML domain, on the other hand, α_k^* and α_{k+1}^* are

$$\alpha_l^* = -\frac{i}{\Delta x} \left(\sum_{j=-N}^{-l} a_j e^{ij\alpha\Delta x} + \sum_{j=-l+1}^N a_j e^{ij\alpha\Delta x - \int_0^{(l+j)\Delta x} \sigma_{j\Delta x} d(j\Delta x)} \right) e^{\int_0^{l\Delta x} \sigma_{j\Delta x} d(j\Delta x)}. \quad (4.10)$$

and

$$\alpha_{l+1}^* = -\frac{i}{\Delta x} \left(\sum_{j=-N}^{-l-1} a_j e^{ij\alpha\Delta x} + \sum_{j=-l}^N a_j e^{ij\alpha\Delta x - \int_0^{(l+1+j)\Delta x} \sigma_{j\Delta x} d(j\Delta x)} \right) e^{\int_0^{(l+1)\Delta x} \sigma_{j\Delta x} d(j\Delta x)}, \quad (4.11)$$

where α_k^* is not consistent with α_{k+1}^* since the absorption function varies with respect to the grid points. For the consistency of the effective wavenumbers, we assume that the absorption at each grid should be small enough to minimize the discrepancy of α_l^* and α_{l+1}^* . Thus, the maximum discrepancy of effective wavenumbers between two adjacent grid point is denoted as wavenumber error, ε and it is expressed as

$$\varepsilon = \mu \max(|\alpha_{l+1}^* \Delta x - \alpha_l^* \Delta x|), \quad (4.12)$$

where a damping factor, $\mu = e^{-\int_0^{l\Delta x} \sigma_{j\Delta x} d(j\Delta x)}$ is multiplied since the error decreases by a factor of the absorption by PML. To ensure accuracy in the discretized space with the optimized 7-point stencil, we define the value of ε should provide an approximation as good as $\varepsilon \leq 0.005$ up to $\alpha\Delta x = 1.16$. Otherwise, the incident wave will show non-physical solutions at the interface. ε for various absorption profiles are plotted for $0 \leq \alpha\Delta x \leq 1.16$ in Fig. 4.4. We should note that the error becomes larger as the absorption coefficient increases, and an overly large absorption at a grid point that incurs the sharp change of solution can be attributed to the discretization errors. This implies that there is a maximum value of $\tilde{\sigma}$ with respect to the PML width (D) that guarantees

the accuracy at each grid point. Hence, the numerical calculation is conducted to obtain the corresponding maximum absorption coefficient $\tilde{\sigma}_{max}$ for various PML widths. In Fig. 4.5, the allowable maximum absorption coefficients are plotted. It might seem that any size of width is possible as long as $\tilde{\sigma}$ is less than the maximum value, $\tilde{\sigma}_{max}$, but the minimum absorption coefficient exists that sufficiently damp out the solution and it will restrict the width.

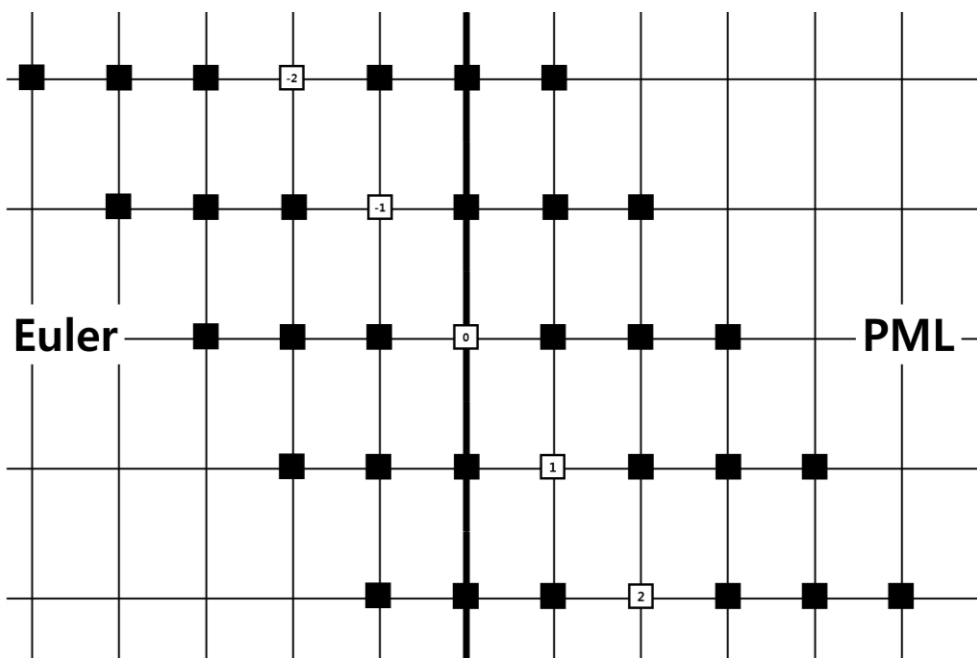


Fig. 4. 3 An illustration of stencils to be used for derivatives near the interface.

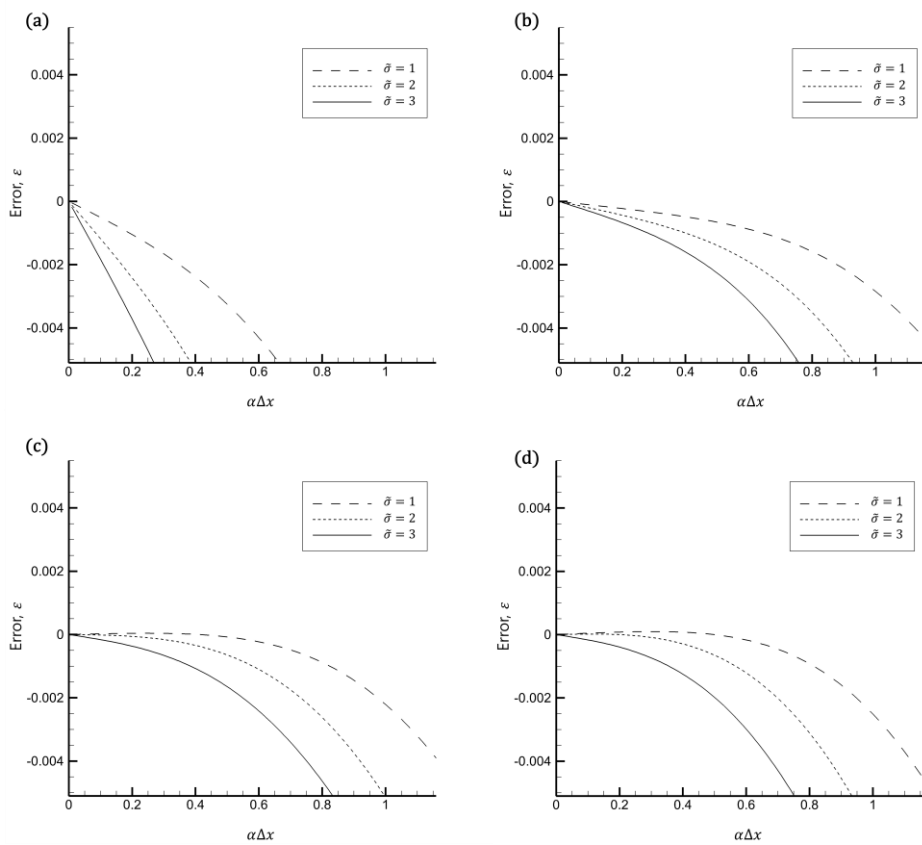


Fig. 4. 4 Wavenumber errors (ϵ) for linear (a), square (b), cubic (c) and quartic (d) absorption profiles.

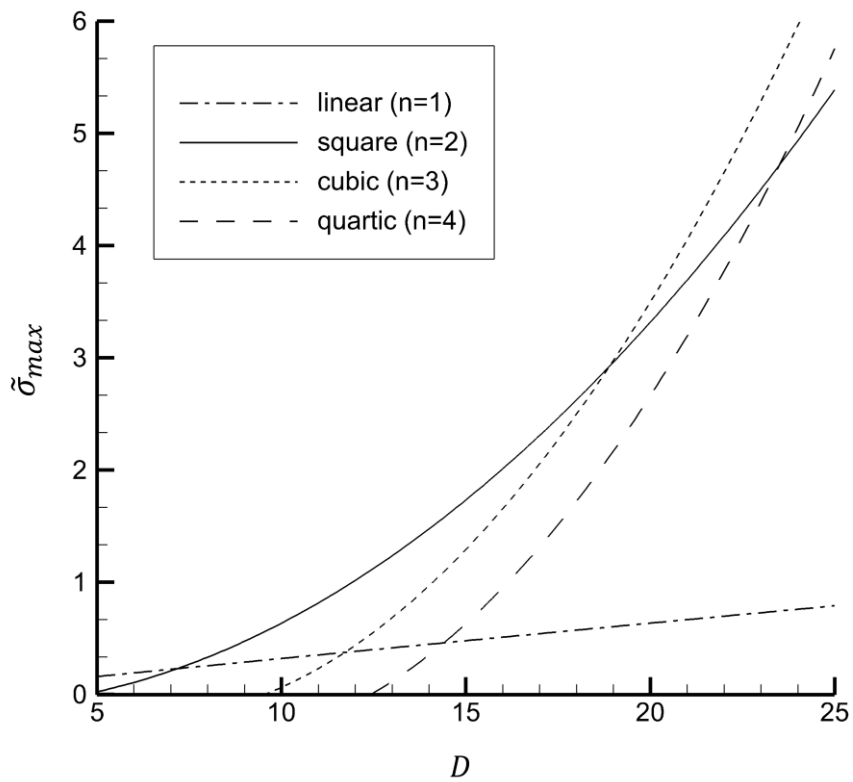


Fig. 4. 5 The maximum absorption coefficients.

4.2.2 Minimum Absorption Coefficient

When the exact solution of acoustic wave of the two-dimensional LEE is written as

$$p(x, y, t) = \frac{p_0}{2\alpha} \int_0^\infty e^{-\xi^2/4\alpha} \cos(\xi t) J_0(\xi \eta) \xi d\xi, \quad (4.13)$$

where $\alpha = (ln2)/9$, $\eta = [(x - Mt)^2 + y^2]^{1/2}$, and J_0 is the Bessel functions of 0, we can also derive the exact solution of the PML equation in the x-direction as

$$p_{pml}(x, y, t) = p(x, y, t) e^{-\int_{\delta_0}^x \sigma_x dx}, \quad (4.14)$$

where σ_x is the absorption coefficient and δ_0 is the first grid point of the PML domain. In general, the absorption coefficient is defined as a smooth function. If we let $\sigma_x = \tilde{\sigma}(x/D)^n$ in which D is the PML width, Eq. (4.14) becomes

$$p_{pml}(x, y, t) = p(x, y, t) e^{-\frac{\tilde{\sigma} x^{n+1}}{(n+1)D^n}}. \quad (4.15)$$

At the endpoint $x = \delta_l$, p_{pml} normalized by p_0 , which is a value at δ_0 , can be written as

$$\frac{p_{pml}(\delta_l, y, t)}{p_0} = \frac{p(\delta_l, y, t)}{p_0} e^{-\frac{\tilde{\sigma} \delta_l^{n+1}}{(n+1)D^n}}. \quad (4.16)$$

From the geometric spreading law of plane wave propagation, the value of p/p_0 can be expressed as $r^{-1/2}$. The results of Eq. (4.16) for various absorption profiles with respect to the PML width (D) are plotted in Fig. 4.6. From this analytical solution, we find that at the endpoint of the PML domain, the wave converges to zero differently with respect to $\tilde{\sigma}$. Since we are dealing with a fourth-order spatial discretization scheme, the perfectly absorbing condition can be defined as $p_{pml}/p_0 < 0.001$. Hence, the minimum value of $\tilde{\sigma}$ that satisfies the perfectly absorbing condition at the end of the boundary can be obtained by numerical calculation. In Fig. 4.7, the minimum absorption coefficient $\tilde{\sigma}_{min}$ is plotted for various PML widths. It is shown that a short width requires a large absorption coefficient since there is not enough length to absorb the outgoing waves and this varies with the power n .

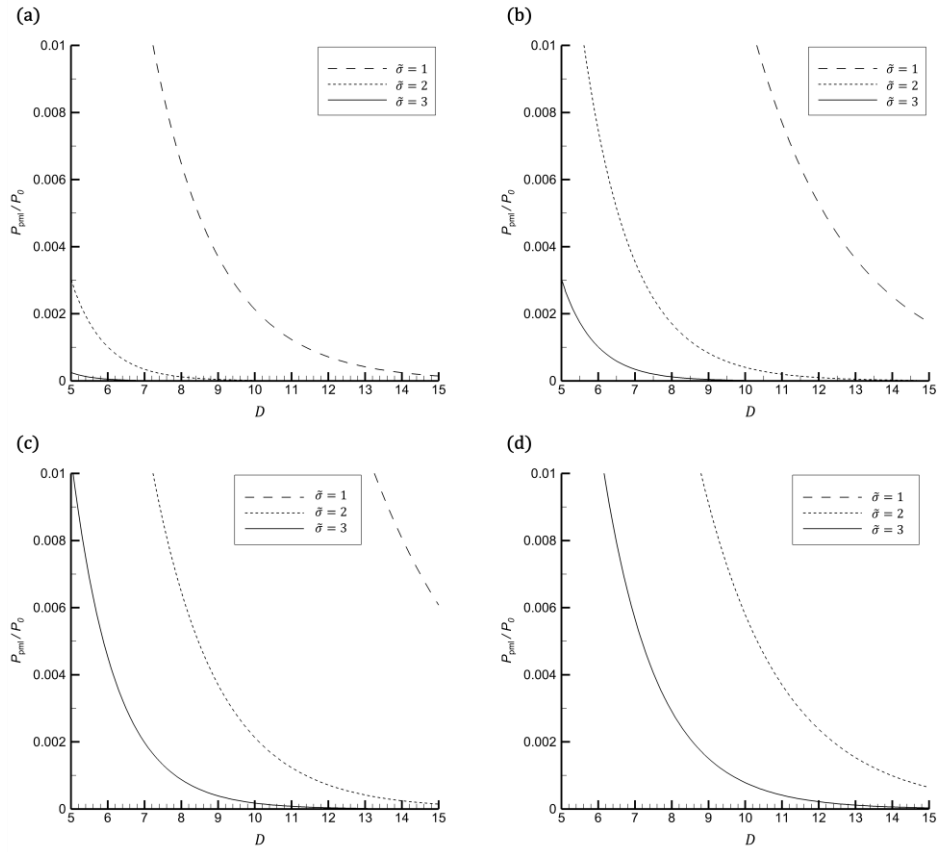


Fig. 4. 6 Pressure value at the end point of the PML domain for linear (a), square (b), cubic (c) and quartic (d) absorption profiles.

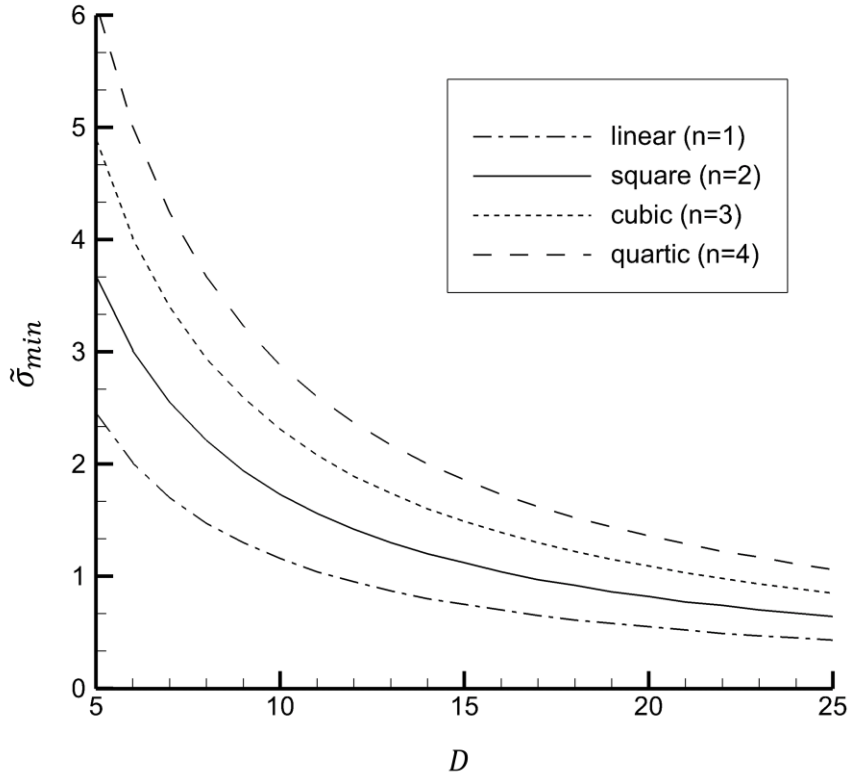


Fig. 4. 7 The minimum absorption coefficients.

Now we can combine the results of the maximum and minimum absorption coefficients in order to deduce the proper range of absorption coefficient in the PML domain. By superimposing Fig. 4.5 on Fig. 4.7, the non-reflective PML conditions for the absorption profiles can be obtained. The optimum PML width that minimizes the width and the range of absorption coefficients are tabulated in table 2. It is found that the square profile has the minimum PML width. The non-reflective PML condition is when the PML width is larger than optimum width and the absorption coefficient is in between $\tilde{\sigma}_{min}$ and $\tilde{\sigma}_{max}$. In the case $\tilde{\sigma} > \tilde{\sigma}_{max}$, it is called over-damped, and there is a discontinuous effect that brings about a spurious wave at the interface of the Euler and the PML domains. In the case of $\tilde{\sigma} < \tilde{\sigma}_{min}$, it is called under-damped, and the solution is reflected, since it is not fully absorbed in the PML domain. Hence, it is recommended to choose D and $\tilde{\sigma}$ inside the non-reflective condition.

Table 2 Optimum PML conditions for various profiles, $\Gamma(x)$

$\Gamma(x)$	Optimum width, $D_{opt}/\Delta x$	Range of $\tilde{\sigma}$
Linear (n=1)	19	$0.50 \leq \tilde{\sigma} \leq 0.52$
Square (n=2)	13	$1.30 \leq \tilde{\sigma} \leq 1.32$
Cubic (n=3)	16	$1.39 \leq \tilde{\sigma} \leq 1.78$
Quartic (n=4)	18	$1.50 \leq \tilde{\sigma} \leq 1.76$

Chapter 5. Numerical Tests

In order to demonstrate the theoretical approach of stability analysis and effectiveness of optimum width prediction put forward so far, numerical examples of acoustic wave absorption are presented in the PML region with predicted PML width (D), absorption coefficient ($\tilde{\sigma}$) and time-step size (Δt).

Two dimensional linearized Euler equations and PML equations in (2.1) and (2.23) are used as governing equations and solved numerically by a finite difference scheme. In particular, 4th order 7-point central difference scheme is used for the entire domain, combined with null-ghost points introduced in chapter 4.1. As time integration, optimized 4-level time discretization method is used. Acoustic source is decayed in PML domain by gradually varying absorption coefficient that is,

$$\sigma_x = \tilde{\sigma}(1 - M^2)\left(\frac{x - \delta_0}{D}\right)^n, \quad \sigma_y = \tilde{\sigma}\left(\frac{y - \delta_0}{D}\right)^n, \quad (5.1)$$

where δ_0 and δ_l refer to the point where PML starts and the thickness of PML domain respectively. A factor of $(1 - M^2)$ is included in σ_x since the absorption rate in x-direction is increased by a factor of $1/(1 - M^2)$, which means it will be larger than that in the y-direction for the same $\tilde{\sigma}$. Specifically, n is 2 for entire simulations. Any artificial damping or filter is not applied in the present work. Unless noted otherwise, the Euler domain is initialized with the following Gaussian pulse:

$$p = \rho = \exp\left[(-\ln 2)\frac{x^2 + y^2}{9}\right], \quad u = v = 0. \quad (5.2)$$

5.1 Stability Analysis Results

In order to demonstrate the stability criteria of PML in chapter 3, the wave propagation in a uniform mean flow is tested. In Fig. 5.1, which is the enlarged curves of Fig. 3.4, the maximum absorption coefficients with respect to mean flow are plotted. Cases 1 and 2 are tested for low Mach number, and Cases 3 and 4 are tested for high Mach number mean flow conditions. The Euler domain is discretized by equidistant $[-40,40] \times [-40,40]$ grids, where $\Delta x = \Delta y = 1$ and $20 \Delta x$ more grids are extended further for PML domains.

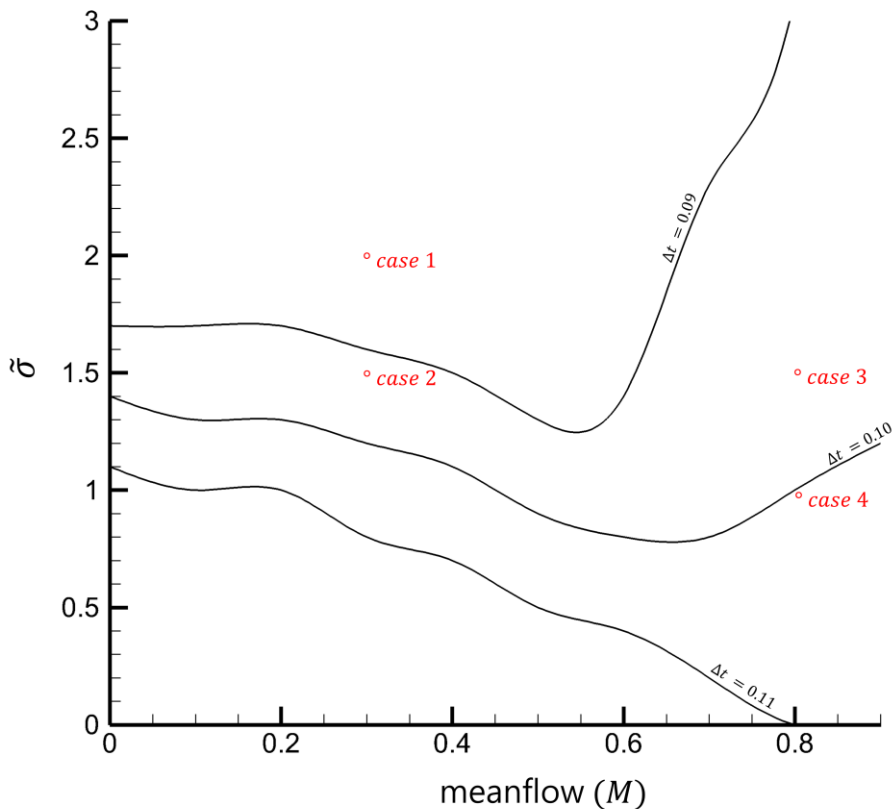


Fig. 5. 1 Region of stability in the complex plane.

5.1.1 Sound Propagating in Low Mach number Uniform Flow

The first example is to show the effect of the absorption coefficient on the stability of PML in low Mach number Uniform flow, $M = 0.3$. We let the time step size $\Delta t = 0.09$ and absorption coefficient of case 1 be $\tilde{\sigma} = 2.0$ while case 2 is $\tilde{\sigma} = 1.5$. According to the stability analysis in Fig. 5.1, the solution of case 1 should diverge while the solution of case 2 should show stable solution. Fig. 5.2 (a) and (b) show the pressure contours of case 1 and 2, respectively. Compared that case 2 shows the stable solution, the spurious waves are detected in the PML domain of case 1.

5.1.2 Sound Propagating in High Mach number Uniform Flow

In the second example, high Mach number Uniform flow, $M = 0.8$ is simulated. Here, we let the time step size be $\Delta t = 0.1$ and absorption coefficient of case 3 be $\tilde{\sigma} = 1.5$ which is higher than the maximum value while case 4 is $\tilde{\sigma} = 1.0$ which is in the stable region from Fig. 5.1. Fig. 5.3 show the pressure contours of case 3 and 4. Compared that case 4 shows the stable solution, the spurious waves are detected in the PML domain of case 3. Thus, it can be said that excellent agreement is observed with the prediction of the time step size.

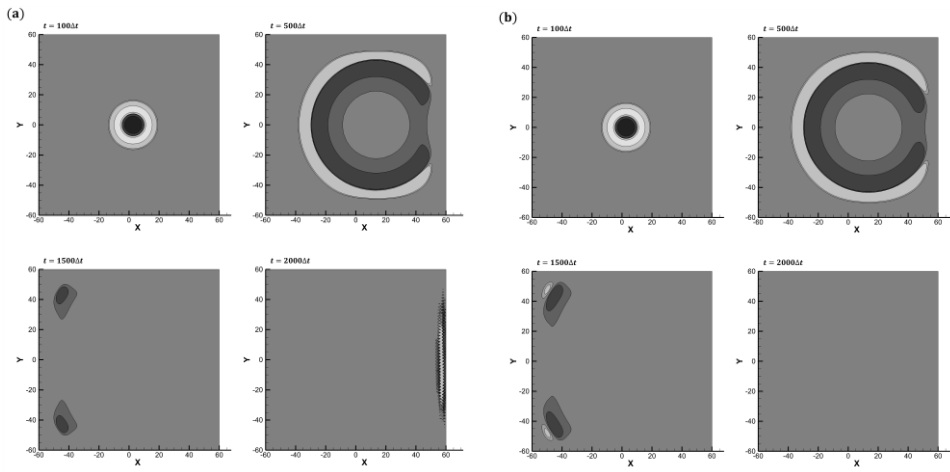


Fig. 5. 2 Pressure contours of case 1 (a) and case 2 (b).

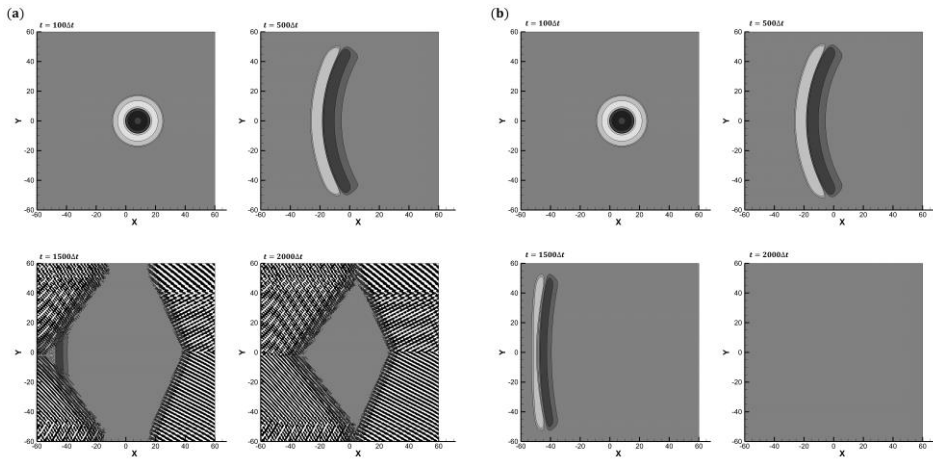


Fig. 5. 3 Pressure contours of case 3 (a) and case 4 (b).

5.2 Accuracy Analysis Results

In order to demonstrate the effectiveness of the optimum-width and absorption coefficient prediction put forward in chapter 4, numerical examples of acoustic wave absorption are presented in the PML domain with a predicted PML width (D) and absorption coefficient ($\tilde{\sigma}$). Simulations are presented in both Cartesian and curvilinear coordinate systems in order to show the effects of absorption coefficients on the performance of PML with the optimum PML width. The simulations are conducted with the square profile in Table 2. For examples of each particular case, over-damped ($\tilde{\sigma} > \tilde{\sigma}_{max}$), under-damped ($\tilde{\sigma} < \tilde{\sigma}_{min}$) conditions and shorter width ($D < D_{opt}$) will be presented.

5.2.1 Sound Propagating in Cartesian Grid System

The wave propagation in a uniform mean flow is tested to validate the optimum PML condition. The Euler domain is discretized by equidistant $[-50,50] \times [-50,50]$ grids, where $\Delta x = \Delta y = 1$ with $D/\Delta x$ more grids extended further for the PML domains and initialized with the following Gaussian pulse:

$$p = \rho = \varepsilon \exp \left[-\frac{(x - x_0)^2 + (y - y_0)^2}{r_0} \right] \quad \text{and} \quad u = v = 0, \quad (5.3)$$

where ε is the pressure perturbation amplitude, $\varepsilon = 1$, r_0 is the characteristic dimension of the pulse, $r_0 = 9/\ln(2)$, and the source position (x_0, y_0) is the centroid of the computational domain. Here, Mach number of the mean flow is $M = 0.5$ and the time step size $\Delta t = 0.05$.

The contour of propagation in the PML domain with square profile at $1000\Delta t$ is shown in Fig. 5.4. The wave is stably absorbed in the PML domain without noticeable reflection at the interface for $\tilde{\sigma} = 1.3$ and $D = 13\Delta x$. Meanwhile, spurious waves are observed in the over-damped ($\tilde{\sigma} = 1.6$) and under-damped ($\tilde{\sigma} = 1.0$) conditions with the same PML width. When the PML width becomes smaller ($D = 10\Delta x$), the solution seems to

be similar to the over-damped case. To further assess the accuracy of optimization as time marches, we plot root mean square error (RMSE) at the position (49,0) in Fig. 5.5. The graph includes four cases of numerical solutions with the reference solution. The reference solution is obtained by using a larger computational domain, so that it is not affected by any boundary effects. It is shown that the RMSE is minimized for $\tilde{\sigma} = 1.3$ and $D = 13\Delta x$ which is the predicted conditions in Table 1.

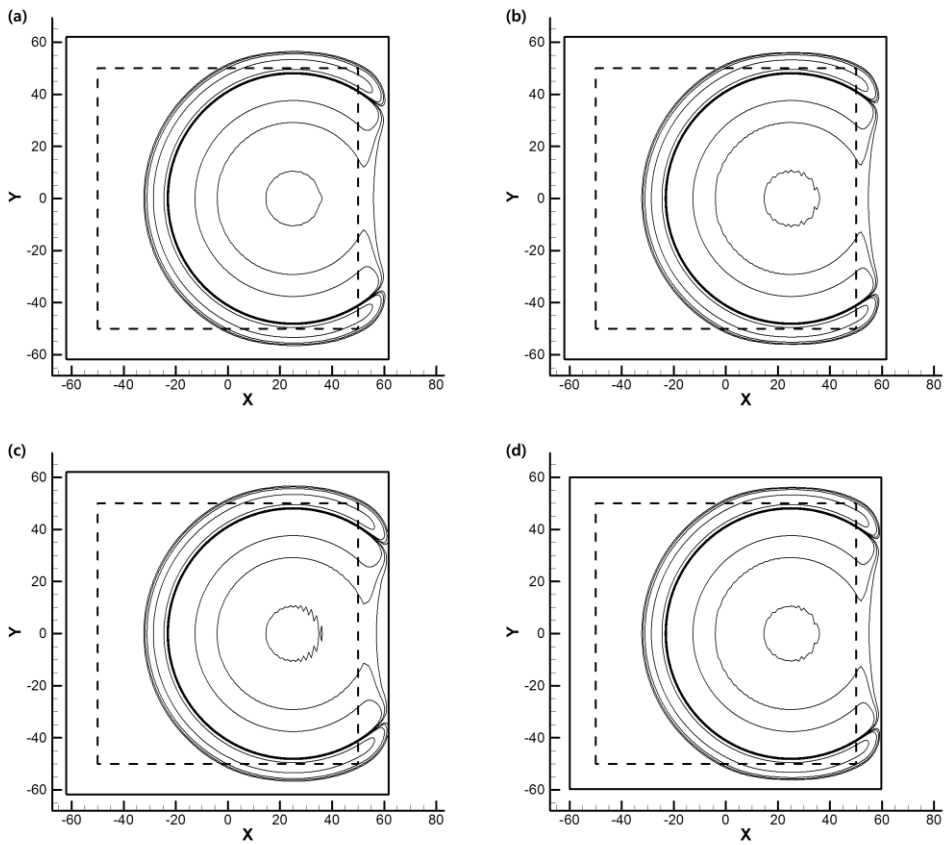


Fig. 5. 4 Contours of the pressure component with the square PML profiles at levels ± 0.1 , ± 0.05 , and ± 0.003 . For figures correspond to the PML conditions of $\tilde{\sigma} = 1.3$ (a), $\tilde{\sigma} = 1.6$ (b), $\tilde{\sigma} = 1.0$ (c) with $D = 13\Delta x$ and $\tilde{\sigma} = 1.3$ with $D = 10\Delta x$ (d).

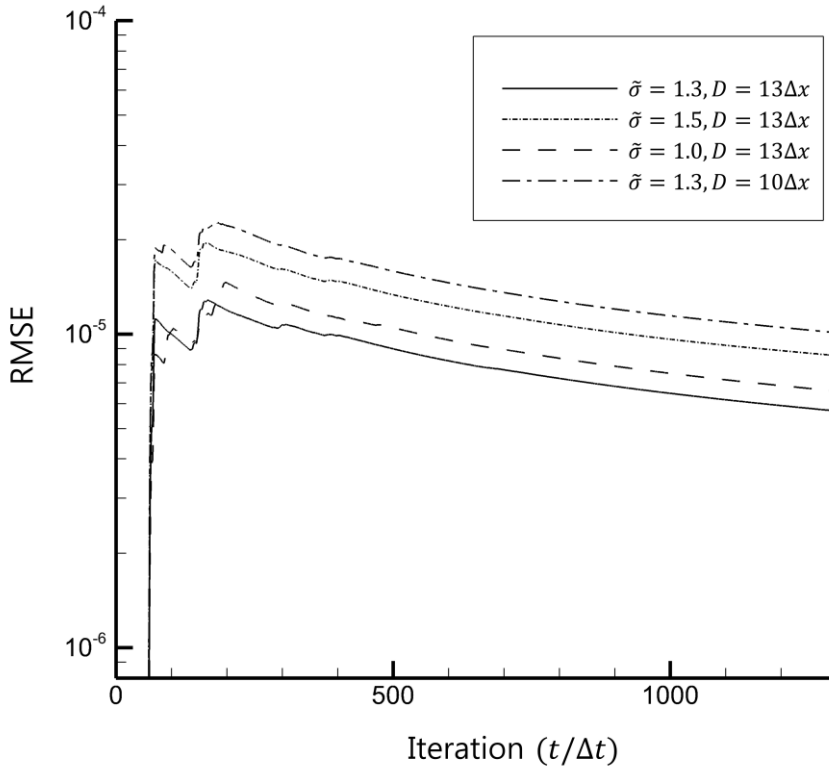


Fig. 5.5 Root mean square error (RMSE) of a Cartesian grid for square PML profiles at (49,0).

5.2.2 Sound Propagating in Curvilinear Grid System

If the computational domain is discretized by curvilinear grids for some particular situations, the PML domain should also be discretized by curvilinear grids accordingly. Thus, we adopt two-dimensional generalized PML equations in Eqs. (2.24) and (2.25). The boundary conditions are described in Fig. 5.6. A detailed analysis of the reflection of acoustic wave from a cylinder wall using solid wall boundary condition by a ghost values has been carried out by Tam and Dong [40]. Since the configuration is symmetric, only the upper half of the domain is considered, and symmetry boundary conditions are

invoked along $\theta = 0^\circ$ and 180° . The dimension of the used computational grid is 50×360 , where $\Delta\xi = \Delta\eta = 1$ with $D/\Delta x$ more grids extended further for the PML domains. The mesh shown in Fig. 5.6 is generated analytically according to the expression:

$$\begin{aligned} r(i) &= x_{min} + \Delta\xi(i - 1) \\ x(i, j) &= r(i)\cos\left(\frac{\pi}{360}j\Delta\eta\right) \\ y(i, j) &= r(i)\sin\left(\frac{\pi}{360}j\Delta\eta\right), \end{aligned} \quad (5.4)$$

where x_{min} determines the diameter of the cylinder and $x_{min} = 20\Delta\xi$ in the simulation.

First, the Gaussian pulse of Eq. (5.3) centered at $(x, y) = (60, 0)$ is initialized without mean flow in the physical domain and the time step size $\Delta t = 0.04$. In Fig. 5.7, an example of the wave propagation in the PML domain with square profiles at $2300\Delta t$ is shown. The wave is stably absorbed in the PML domain without noticeable reflection at the interface for $\tilde{\sigma} = 1.3$ and $D = 13\Delta x$, which is the optimum value in Table 1. Similar to the examples in a Cartesian coordinate system, spurious waves are observed in the over-damped ($\tilde{\sigma} = 1.6$), under-damped ($\tilde{\sigma} = 1.0$) and smaller width ($D = 10\Delta x$) conditions. Root mean square error (RMSE) at the position $(x, y) = (122, 0)$ of numerical solutions for each condition and the reference solution are plotted in Fig. 5.8. It is shown that the RMSE is still minimized for $\tilde{\sigma} = 1.3$ and $D = 13\Delta x$ for curvilinear grid system.

In the second example, we solve the Euler equations with the following source term added to Eq. (5.3):

$$p = \rho = \varepsilon \sin(\Omega t) \exp\left[-\frac{(x - x_0)^2 + (y - y_0)^2}{r_0}\right]. \quad (5.5)$$

Here, the frequency of the source is $\Omega = 0.05\pi$ and other conditions are the same as previous example. The square absorption profile is adopted for this time. Fig. 5.9 shows the pressure contours of the numerical simulation at $t = 5000\Delta t$. The differences

between the numerical and exact solutions [41] along the line $y = 0$ are plotted in Fig. 5.10. Clearly, these two results show that the prediction of accuracy at the interface of the PML domain works well for Gaussian pulse propagation in the curvilinear coordinate system as well.

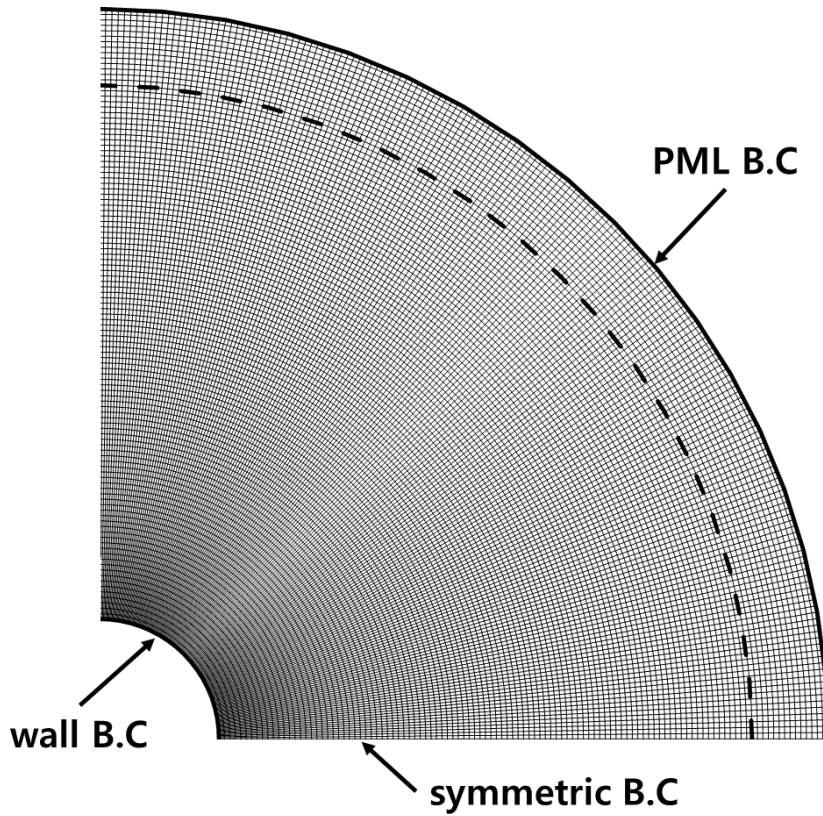


Fig. 5. 6 A curvilinear grid structure with boundary conditions.

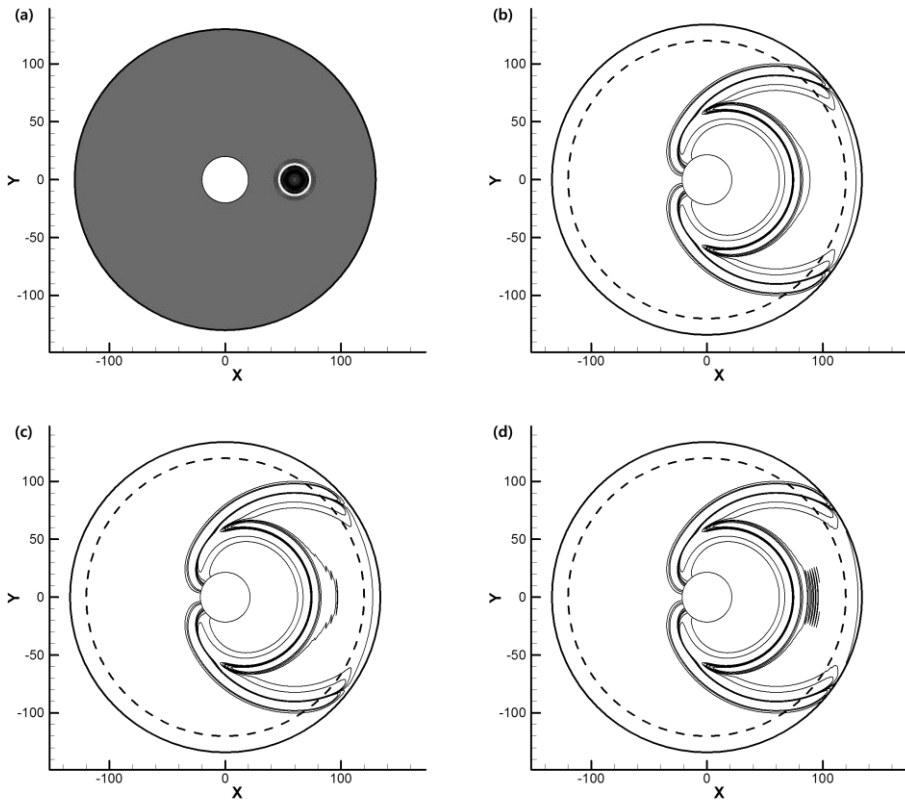


Fig. 5.7 Contours of the pressure component with the square PML profiles at levels ± 0.1 , ± 0.05 , and ± 0.003 . For figures correspond to the PML conditions of $\tilde{\sigma} = 1.3$ (a), $\tilde{\sigma} = 1.6$ (b), $\tilde{\sigma} = 1.0$ (c) with $D = 13\Delta x$ and $\tilde{\sigma} = 1.3$ with $D = 10\Delta x$ (d).

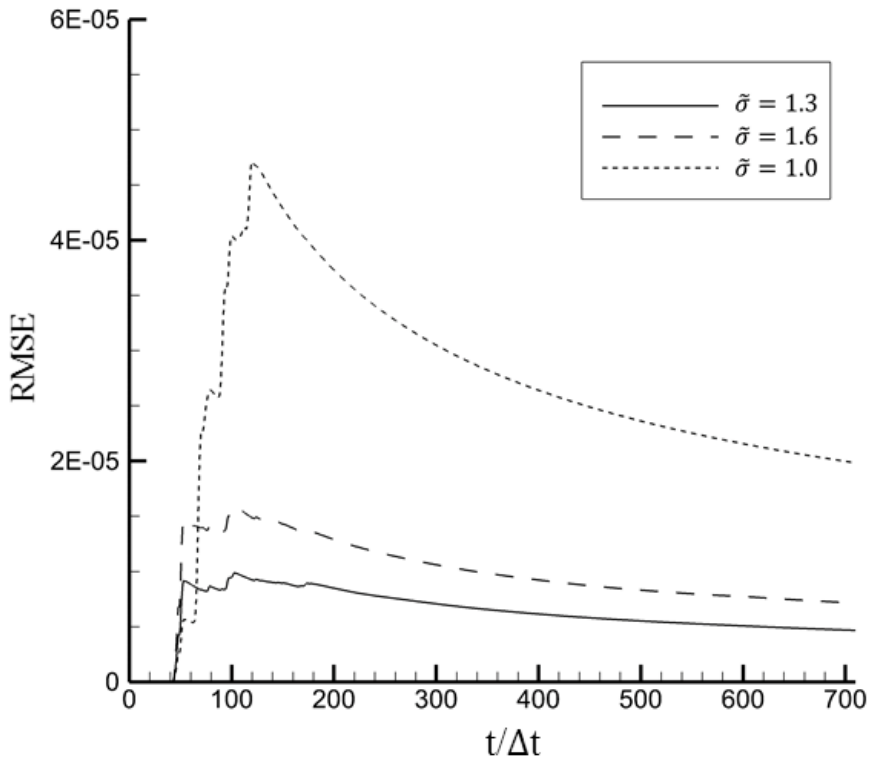


Fig. 5. 8 Root mean square error (RMSE) of pressure in a curvilinear grid for square PML profile at (122,0).

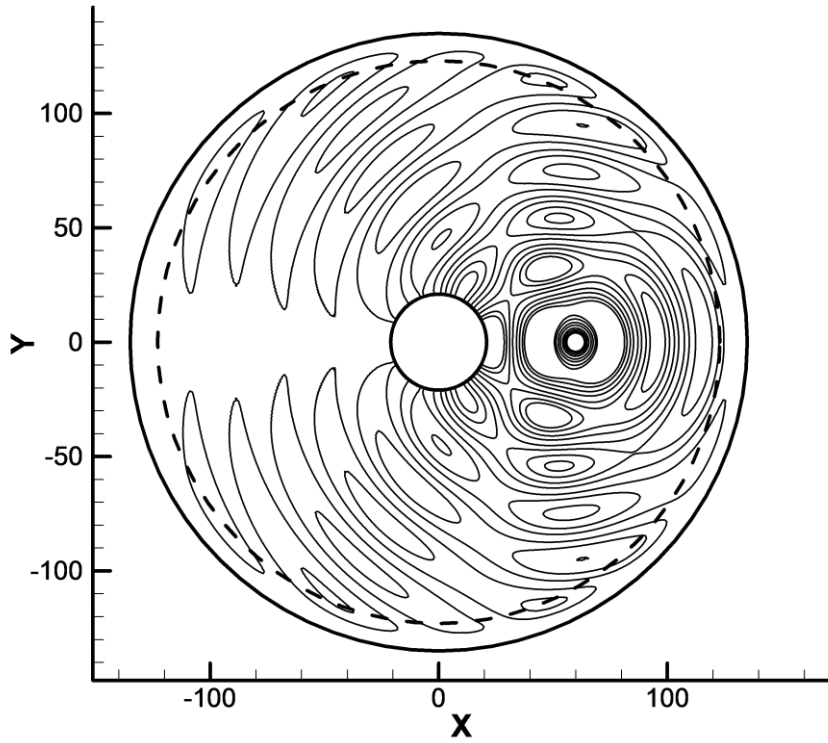


Fig. 5.9 Contours of the sinusoidal wave propagation with the square PML profiles at levels ± 1.0 , ± 0.5 , ± 0.1 , and ± 0.05 .

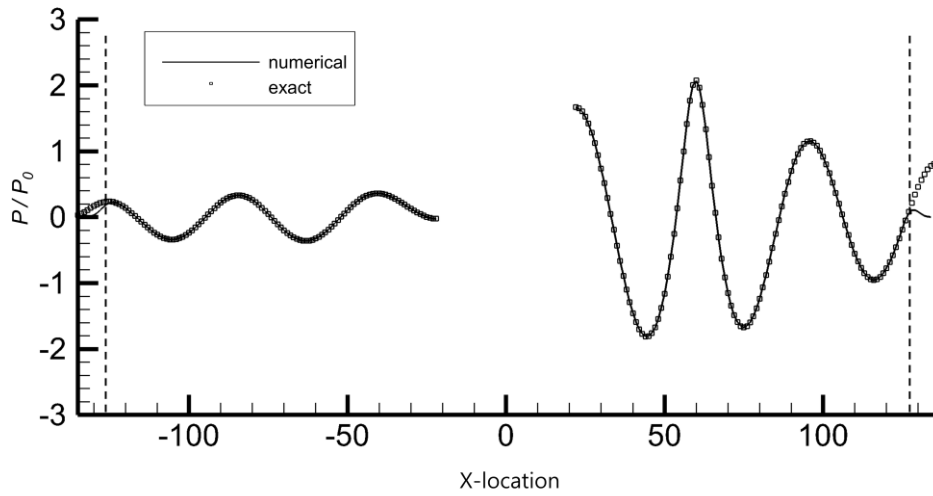


Fig. 5. 10 Solutions of the scattered acoustic field along the line at $y=0$.

Chapter 6. Concluding Remarks

The numerical stability analysis on PML equation by manipulating the dispersion relation of PML equation was discussed. First, we derived the complex stability diagram of particular time integration scheme. Second, the maximum physical root of dispersion relation was found by considering the maximum wavenumber of spatial discretization scheme. Finally, by comparing this two results, the time step limitation was achieved that can ensure the dispersion relation preserving property as well as the convergence. In addition to the stability criteria, we also dealt with the optimum PML width and its corresponding absorption coefficient in order to minimize the computational cost while satisfying the accuracy. In the computational tests reported here, suggested PML width and time step obtained from stability criteria showed a good agreement in the simulation. It was further showed that the stability analysis could also be applied in case of generalized coordinate as well. The proposed stability analysis is expected to be extended to the non-linear PML governing equations in future works.

References

1. Hardin, J. C., and J. R. Ristorcelli. "ICASE/LaRC Workshop on Benchmark Problems in Computational Aeroacoustics." National Aeronautics and Space Administration (1994).
2. Hixon, Ray. "Evaluation of a high-accuracy MacCormack-type scheme using benchmark problems." *Journal of Computational Acoustics* 6.03 (1998): 291-305.
3. Lin, San-Yih, and Yan-Shin Chin. "Comparison of higher resolution Euler schemes for aeroacoustic computations." *AIAA journal* 33.2 (1995): 237-245.
4. Zhuang, M., and R. F. Chen. "Applications of high-order optimized upwind schemes for computational aeroacoustics." *Aiaa Journal* 40.3 (2002): 443-449.
5. Harten, Ami, and Stanley Osher. "Uniformly high-order accurate nonoscillatory schemes. I." *SIAM Journal on Numerical Analysis* 24.2 (1987): 279-309.
6. Ko, D. K., and D. J. Lee. "Development of an efficient fourth-order non-oscillatory scheme for compressible flows." (1998).
7. Shu, Chi-Wang. *Essentially non-oscillatory and weighted essentially non-oscillatory schemes for hyperbolic conservation laws*. Springer Berlin Heidelberg, 1998.
8. Shu, Chi-Wang. *Essentially non-oscillatory and weighted essentially non-oscillatory schemes for hyperbolic conservation laws*. Springer Berlin Heidelberg, 1998.
9. Chang, Sin-Chung. "The method of space-time conservation element and solution element—a new approach for solving the Navier-Stokes and Euler equations." *Journal of computational Physics* 119.2 (1995): 295-324.
10. Stanescu, D., et al. "Multidomain spectral computations of sound radiation from ducted fans." *AIAA journal* 37.3 (1999): 296-302.
11. Lele, Sanjiva K. "Compact finite difference schemes with spectral-like resolution." *Journal of computational physics* 103.1 (1992): 16-42.
12. Tam, Christopher Kw, and Jay C. Webb. "Dispersion-relation-preserving schemes

- for computational aeroacoustics." DGLR/AIAA Aeroacoustics Conference, 14 th, Aachen, Germany. 1992.
13. Berenger, Jean-Pierre. "A perfectly matched layer for the absorption of electromagnetic waves." *Journal of computational physics* 114.2 (1994): 185-200.
 14. Hu, Fang Q. "On absorbing boundary conditions for linearized Euler equations by a perfectly matched layer." *Journal of Computational Physics* 129.1 (1996): 201-219.
 15. Hu, Fang Q. "On perfectly matched layer as an absorbing boundary condition." *AIAA paper* (1996): 96-1664.
 16. Abarbanel, S., D. Gottlieb, and Jan S. Hesthaven. "Well-posed perfectly matched layers for advective acoustics." *Journal of Computational Physics* 154.2 (1999): 266-283.
 17. Whitham, Gerald Beresford. *Linear and nonlinear waves*. Vol. 42. John Wiley & Sons, 2011.
 18. Hu, Fang Q. "A stable, perfectly matched layer for linearized Euler equations in unsplit physical variables." *Journal of Computational Physics* 173.2 (2001): 455-480.
 19. Hagstrom, Thomas, and Igor Nazarov. "Absorbing layers and radiation boundary conditions for shear flow calculations." *AIAA paper* 3298 (2003): 2003.
 20. Hu, Fang Q. "A perfectly matched layer absorbing boundary condition for linearized Euler equations with a non-uniform mean flow." *Journal of Computational Physics* 208.2 (2005): 469-492.
 21. Meza-Fajardo, Kristel C., and Apostolos S. Papageorgiou. "A nonconvolutional, split-field, perfectly matched layer for wave propagation in isotropic and anisotropic elastic media: stability analysis." *Bulletin of the Seismological Society of America* 98.4 (2008): 1811-1836.
 22. Savadatti, Siddharth, and Murthy N. Guddati. "Absorbing boundary conditions for scalar waves in anisotropic media. Part 1: Time harmonic modeling." *Journal of Computational Physics* 229.19 (2010): 6696-6714.
 23. Parrish, Sarah A., and Fang Q. Hu. "PML absorbing boundary conditions for the

- linearized and nonlinear Euler equations in the case of oblique mean flow." *International journal for numerical methods in fluids* 60.5 (2009): 565-589.
24. Nataf, Frédéric. "A new approach to perfectly matched layers for the linearized Euler system." *Journal of Computational Physics* 214.2 (2006): 757-772.
 25. Hu, Fang Q. "Development of PML absorbing boundary conditions for computational aeroacoustics: A progress review." *Computers & Fluids* 37.4 (2008): 336-348.
 26. Velu, Srinivasa Perumal, and Klaus A. Hoffmann. Development and application of perfectly matched layer for numerical boundary treatment. Diss. Wichita State University, College of Engineering, Department of Aerospace Engineering., (2010).
 27. Chew, Weng Cho, and William H. Weedon. "A 3D perfectly matched medium from modified Maxwell's equations with stretched coordinates." *Microwave and optical technology letters* 7.13 (1994): 599-604.
 28. Collino, Francis, and Peter Monk. "The perfectly matched layer in curvilinear coordinates." *SIAM Journal on Scientific Computing* 19.6 (1998): 2061-2090.
 29. Bayliss, Alvin, and Eli Turkel. "Radiation boundary conditions for wave-like equations." *Communications on Pure and applied Mathematics* 33.6 (1980): 707-725.
 30. Hariharan, S. I., J. R. Scott, and K. L. Kreider. "A potential-theoretic method for far-field sound radiation calculations." *Journal of Computational Physics* 164.1 (2000): 143-164.
 31. Tam, Christopher KW. "Computational aeroacoustics: an overview of computational challenges and applications." *International Journal of Computational Fluid Dynamics* 18.6 (2004): 547-567.
 32. Wang, J. L., et al. "Explicit High Accuracy Maximum Resolution Dispersion Relation Preserving Schemes for Computational Aeroacoustics."
 33. Cunha, G., and S. Redonnet. "On the effective accuracy of spectral-like optimized finite-difference schemes for computational aeroacoustics." *Journal of*

- Computational Physics 263 (2014): 222-232.
34. Tam, Christopher KW. Computational aeroacoustics: A wave number approach. Vol. 33. Cambridge University Press, 2012.
 35. Gary, John. "On boundary conditions for hyperbolic difference schemes." *Journal of Computational Physics* 26.3 (1978): 339-351
 36. Li, Yuguo. "Wavenumber-extended high-order upwind-biased finite-difference schemes for convective scalar transport." *Journal of Computational Physics* 133.2 (1997): 235-255
 37. Zhou, D., et al. "The perfectly matched layer boundary condition for scalar finite-difference time-domain method." *Photonics Technology Letters, IEEE* 13.5 (2001): 454-456.
 38. Chew, Weng Cho, and William H. Weedon. "A 3D perfectly matched medium from modified Maxwell's equations with stretched coordinates." *Microwave and optical technology letters* 7.13 (1994): 599-604.
 39. Agrawal, Arti, and Anurag Sharma. "Perfectly matched layer in numerical wave propagation: factors that affect its performance." *Applied optics* 43.21 (2004): 4225-4231.
 40. Tam, Christopher KW, and Zhong Dong. "Wall boundary conditions for high -order finite -difference schemes in computational aeroacoustics." *Theoretical and Computational Fluid Dynamics* 6.5 -6 (1994): 303 -322.
 41. Morris, Philip J. "Scattering of sound from a spatially distributed, spherically symmetric source by a sphere." *The Journal of the Acoustical Society of America* 98.6 (1995): 3536 -3539.

전산공력음향학에서 Perfectly Matched Layer의 안정적인 흡수조건에 관한 연구

서울대학교 대학원

우주항공공학과

정한아침

국문초록

전산공력음향학에서 유출 및 방사 경계조건은 전체 해석결과에 영향을 미칠 수 있다는 면에서 매우 중요하다고 할 수 있다. 이러한 유출 및 방사 경계조건 중 전산전자기학 및 전산공력음향학에서 널리 사용되고 있는 흡수경계조건은 Perfectly Matched Layer(PML)으로, 해석영역의 지배방정식에 흡수계수에 의한 추가적인 항을 더하여 해석영역과 경계영역 사이에서 안정적으로 파동을 흡수할 수 있다. 또한 시간-공간 변환을 통해 음향파의 특성상 기존 PML 조건에서 발생한 다양한 유동조건에서 위상속도(phase velocity)와 군속도(group velocity) 방향의 변화 문제가 해결되었다. 하지만 실제 이산화된 해석영역에서 해석적으로 안정적인 PML 방정식은 시간 및 공간 차분간격과 유동속도 및 흡수계수 변화에 따라 수치적인 불안정성을 발생하는 문제를 갖게 된다.

본 논문에서는 이러한 수치적인 불안정성에 미치는 요인들을 실제 수치기법을 적용하여 연구하였다. 먼저 시간차분간격(time step size)을 위해 PML 방정식의 이산관계(dispersion relation) 관점에서 수치적으로 안정적인 해석

조건을 도출하였다. 또한 유동속도에 따라 PML 영역에서 안정적인 흡수계수 범위 및 최적 너비를 수학적 접근을 통하여 제시하였다. 예측결과를 확인하기 위해 다양한 유동조건뿐 아니라 일반 격자계에서 해석을 진행함으로써 유동속도 및 격자간격의 변화에 따른 시간간격과 흡수계수 및 PML 너비 예측의 정확성을 검증하였다. 이를 통하여 기존에 실험적인 방법에만 의존했던 PML의 해석조건에 대해 차분간격, 유동속도 그리고 흡수계수의 상관관계를 분석하여 PML 해석조건을 예측했다는 점에서 중요한 가치가 있다고 판단된다.

주요 용어: 고해상도 유한차분 (High-order Finite Difference), 이산관계 (Dispersion Relation), 안정성 분석(Stability Analysis), 전산공력음향학 (Computational Aeroacoustics), Perfectly Matched Layer(PML), 이산관계 (Dispersion Relation)

학번 : 2014-20665



저작자표시-비영리-변경금지 2.0 대한민국

이용자는 아래의 조건을 따르는 경우에 한하여 자유롭게

- 이 저작물을 복제, 배포, 전송, 전시, 공연 및 방송할 수 있습니다.

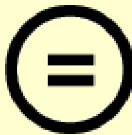
다음과 같은 조건을 따라야 합니다:



저작자표시. 귀하는 원저작자를 표시하여야 합니다.



비영리. 귀하는 이 저작물을 영리 목적으로 이용할 수 없습니다.



변경금지. 귀하는 이 저작물을 개작, 변형 또는 가공할 수 없습니다.

- 귀하는, 이 저작물의 재이용이나 배포의 경우, 이 저작물에 적용된 이용허락조건을 명확하게 나타내어야 합니다.
- 저작권자로부터 별도의 허가를 받으면 이러한 조건들은 적용되지 않습니다.

저작권법에 따른 이용자의 권리는 위의 내용에 의하여 영향을 받지 않습니다.

이것은 [이용허락규약\(Legal Code\)](#)을 이해하기 쉽게 요약한 것입니다.

[Disclaimer](#)

공학석사학위논문

Stable, non-Reflective Condition of Perfectly Matched Layer in Computational Aeroacoustics

전산공력음향학에서 Perfectly Matched Layer의
안정적인 흡수조건에 관한 연구

2016 년 2 월

서울대학교 대학원

기계항공공학부

정한아침

Stable, non-Reflective Condition of Perfectly Matched Layer in Computational Aeroacoustics

Hanahchim Choung

Department of Aerospace Engineering

Seoul National University

Abstract

In Computational Aeroacoustics, non-reflective boundary conditions such as radiation or absorbing boundary conditions are critical issues in that they can affect the whole solutions of computation. Among these types of boundary conditions, Perfectly Matched Layer boundary condition which has been widely used in Computational Electromagnetics and Computational Aeroacoustics is developed by augmenting the additional term by an absorption function in the original governing equations so as to stably absorb the outgoing waves. Even if Perfectly Matched Layer is perfectly non-reflective boundary condition analytically, spurious waves at the interface or instability could be shown since the analysis is performed in the discretized space. Hence, the study is focused on factors that affect these numerical instability and accuracy with particular numerical schemes. First, stability analysis preserving the dispersion relation is carried out in order to achieve the stability limit of time-step size. Then, through mathematical approach, stable absorption coefficient and PML width are suggested. In order to validate the prediction of analysis condition, numerical simulations are performed in generalized coordinate system as well as Cartesian coordinate system.

Keyword: High-order Finite Difference, Dispersion-Relation, Stability Analysis,
Computational Aeroacoustics, Perfectly Matched Layer

Student Number : 2014-20665

Contents

Abstract.....	I
Contents	III
List of Tables	V
List of Figures	VI
Nomenclature.....	VIII
Chapter 1. Introduction.....	1
1.1 BACKGROUND	1
1.2 MOTIVATION.....	2
1.3 SCOPE OF PRESENT STUDY	3
Chapter 2. Governing Equations.....	5
2.1 LINEARIZED EULER EQUATIONS.....	5
2.2 DERIVATION OF PML EQUATIONS.....	6
2.2.1 Complex Change of Variables	6
2.2.2 Space-time Transformation	7
2.2.3 Stable PML Equations	9
Chapter 3. Numerical methodology	14
3.1 OPTIMIZED NUMERICAL METHOD	14
3.1.1 Fourier Analysis of High-order Spatial Discretization.....	14
3.1.2 Optimized Time Discretization Scheme	17
3.2 NUMERICAL STABILITY ANALYSIS.....	19

Chapter 4. Non-Reflective PML Conditions	24
4.1 END CONDITION OF PML BOUNDARY	24
4.2 ANALYTICAL APPROACH ON ABSORPTION COEFFICIENT	28
<i>4.2.1 Maximum Absorption Coefficient</i>	<i>28</i>
<i>4.2.2 Minimum Absorption Coefficient</i>	<i>34</i>
Chapter 5. Numerical Tests	38
5.1 STABILITY ANALYSIS RESULTS.....	39
<i>5.1.1 Sound Propagating in Low Mach number Uniform Flow</i>	<i>40</i>
<i>5.1.2 Sound Propagating in High Mach number Uniform Flow</i>	<i>40</i>
5.2 ACCURACY ANALYSIS RESULTS	42
<i>5.2.1 Sound Propagating in Cartesian Grid System</i>	<i>42</i>
<i>5.2.2 Sound Propagating in Curvilinear Grid System.....</i>	<i>44</i>
Chapter 6. Concluding Remarks	51
References	52
Abstract in Korean	56

List of Tables

Table 1 Values of $k_c^* \Delta x$ and $k_{max}^* \Delta x$ of central DRP scheme for different stencils.

Table 2 Optimum PML conditions for various profiles, $\Gamma(x)$.

List of Figures

Fig. 2. 1 The relationship between ω and kx for various modes of ky without mean flow

Fig. 2. 2 The relationship between ω and kx for various modes of ky with mean flow : no transformation (a) and space-time transformed (b)

Fig. 2. 3 Cartesian computational domain governed by the linearized Euler equations enclosed by PMLs

Fig. 3. 1 $k\Delta x$ versus $k * \Delta x$: —, 7-point; ---, 9-point; — — —, 11-point; - - -, 13-point; - - - 15-point stencil.

Fig. 3. 2 (a) Dissipation and (b) dispersion errors of optimized fourth-order multi-step.

Fig. 3. 3 Region of stability in the complex plane.

Fig. 3. 4 Maximum stable absorption coefficients with respect to mean flow.

Fig. 4. 1 Schematic diagram of 7-point central (upper) and upwind (lower) stencils located in the PML region

Fig. 4. 2 The evolution of pressure error at the point (A), (a) and (B), (b)

Fig. 4. 3 An illustration of stencils to be used for derivatives near the interface.

Fig. 4. 4 Wavenumber errors (ϵ) for linear (a), square (b), cubic (c) and quartic (d) absorption profiles.

Fig. 4. 5 The maximum absorption coefficients.

Fig. 4. 6 Pressure value at the end point of the PML domain for linear (a), square (b), cubic (c) and quartic (d) absorption profiles.

Fig. 4. 7 The minimum absorption coefficients.

Fig. 5. 1 Region of stability in the complex plane.

Fig. 5. 2 Pressure contours of case 1 (a) and case 2 (b).

Fig. 5. 3 Pressure contours of case 3 (a) and case 4 (b).

Fig. 5. 4 Contours of the pressure component with the square PML profiles at levels

$\pm 0.1, \pm 0.05,$ and ± 0.003 . For figures correspond to the PML conditions of $\sigma = 1.3$ (a), $\sigma = 1.6$ (b), $\sigma = 1.0$ (c) with $D = 13\Delta x$ and $\sigma = 1.3$ with $D = 10\Delta x$ (d).

Fig. 5. 5 Root mean square error (RMSE) of a Cartesian grid for square PML profiles at (49,0).

Fig. 5. 6 A curvilinear grid structure with boundary conditions.

Fig. 5. 7 Contours of the pressure component with the square PML profiles at levels $\pm 0.1, \pm 0.05,$ and ± 0.003 . For figures correspond to the PML conditions of $\sigma = 1.3$ (a), $\sigma = 1.6$ (b), $\sigma = 1.0$ (c) with $D = 13\Delta x$ and $\sigma = 1.3$ with $D = 10\Delta x$ (d).

Fig. 5. 8 Root mean square error (RMSE) of pressure in a curvilinear grid for square PML profile at (122,0).

Fig. 5. 9 Contours of the sinusoidal wave propagation with the square PML profiles at levels $\pm 1.0, \pm 0.5, \pm 0.1,$ and ± 0.05 .

Fig. 5. 10 Solutions of the scattered acoustic field along the line at $y=0$.

Nomenclature

➤ English

a_j, b_j	optimized stencils
\mathbf{A}, \mathbf{B}	non-conservative matrix of variables
D	PML width
f	solution in the physical domain
$\bar{\mathbf{E}}, \bar{\mathbf{F}}, \bar{\mathbf{H}}$	conservative matrix of variables
J	Jacobian matrix
k_x	wavenumber in x-direction
l	grid point
M_0	Mach number of free stream
n	power of absorption function
p	acoustic pressure
p_0	normalized ambient pressure
p_{pml}	exact solution of PML equations
\mathbf{q}	auxiliary variables inside the PML domain
r	radial coordinate
\mathbf{U}	matrix of physical variables
u, v	particle velocity in 2-dimensional space
(x, y)	Cartesian coordinates

➤ **Greeks**

$\alpha\Delta x$	wavenumber
$\alpha^*\Delta x$	effective wavenumber
β	amplitude of oscillation
γ	specific heat ratio
$\Gamma(x)$	absorption profile
δ_0, δ_l	first and last grid point of the PML region
Δ	increment
ε	error
λ	Eigen value
(ξ, η)	general coordinates
ρ_0	normalized ambient density
σ_x, σ_y	absorption function
$\tilde{\sigma}$	absorption coefficient
φ	solution in the PML region
ω	angular frequency (rad/s)
Ω	angular frequency of source (rad/s)

➤ **Superscripts**

- ~ Fourier-Laplace transformed quantity or indicator of absorption coefficient
- space-time transformation
- ^ transformed value by Complex change of variables
- * corresponding value of effective wavenumber

➤ **Subscripts**

- i, j grid indices in directions of a coordinate
- x, y space derivatives of Cartesian coordinate system
- ξ, η space derivatives of general coordinate system
- c critical value
- max maximum value
- min minimum value
- opt optimum value
- ref reference value
- 0 free stream value or initial values

Chapter 1. Introduction

1.1 Background

Computational aeroacoustics (CAA) is a numerical approach to the problems of aeroacoustics. Even though aeroacoustics includes miscellaneous research topics, the essential components of interest are all generated from the intrinsically unsteady interactions of different scales in the fluid itself (e.g., turbulence and instability waves) or unsteady fluid-boundary interactions. Thus, it is important to understand the complicated mechanism of sound generation, propagation, interaction with bodies, and radiation.

In contrast to computational fluid dynamics (CFD), with its long history and rapid development, CAA has only recently emerged as a separate area of computational approaches, in that the physics of acoustics should be focused on isotropic, nondispersive, and nondissipative characteristics. However, since these are not of primary interest in CFD, its schemes are dispersive, anisotropic, and sometimes highly dissipative. Since numerical dissipation and dispersion are the two primary sources of error in CAA, classical CFD schemes have been found to be unsatisfactory for the study of wave propagation over long distances and large time intervals [1]. CFD schemes, such as the MacCormack [2] scheme, upwind schemes [3, 4], and essentially non-oscillatory schemes [5–7], have been extended to high orders by using more stencil points for application to acoustic problems. In addition to the conventional finite-difference and finite-volume schemes, finite element [8, 9] and spectral methods [10] have been developed for CAA. Recent studies on CAA have been focused on nondissipation and nondispersion, which are desirable for linear wave propagation. Typically, compact and noncompact high-order schemes, such as Lele’s schemes [11] and dispersion-relation-preserving (DRP) schemes by Tam and Webb [12], have been developed for CAA studies.

1.2 Motivation

Solving non-reflective boundary problems remains an important issue because they are often attributed as the major source of numerical errors in practical computations. Moreover, as the accuracy of spatial and temporal discretization increases, the need for greater accuracy at the boundaries increases accordingly. In this study, numerical stability analysis of a non-reflective boundary based on perfectly matched layers (PML) will be introduced. Since Berenger [13] first introduced a new absorbing boundary condition, which is the split version of the PML equation in computational electromagnetics, much research has been carried out for the PML equation [14–16]. Unfortunately, those formulations entail exponentially growing solutions in computational aeroacoustics, in which the mean flow that induces discrepancy of the group and phase velocities exists. According to the wave propagation theory [17], group and phase velocities are governed by the dispersion relation, a relation between the angular frequency of the waves and the wave numbers of the spatial variables. Hu [18] succeeded in constructing a stable PML formulation, with a parallel uniform mean flow, by the space-time transformation, which organized the phase and group velocity to be consistent. In [18], he addressed both the stability and the issue of well-posedness so that the PML formulation is analytically stable for the linearized Euler equation. The formulation of the PML was also extended to arbitrary nonuniform mean flow by a parameter study [19] and the spectral collocation method [20], which gives a unique space-time transformation. Recently, many issues related to the PML formulation, on which wave propagation in anisotropic media [21, 22], oblique flow [23, 24], and nonlinear wave [25] depend, have been treated.

The conventional stability issues, however, have been limited to an analytical formulation of the PML equation. Since that equation is only reflectionless or stable for exact solutions, the analytical perfection of the PML equation is no longer valid once the PML equation becomes an approximated form of a discretized equation, which is liable to be unstable. Thus, temporal and spatial discretization schemes should be considered,

in addition to the stable analytical form of the PML equation. For numerical stability, it is important that the parameter be set to the proper numerical range so that the spurious solutions are all heavily damped [12]. However, it is not immediately clear if the conventional stability analysis for linearized Euler equation still works on the PML equation. Since that equation is derived by a complex change of variables, the dispersion relation changes accordingly. While conventional stability analysis focuses solely on the real root of the dispersion relation, now we must consider the complex root to achieve stability of the PML equation, because a complex change of variables forces the dispersion relation of the PML equation to bear the imaginary part. This is why it is necessary to find a new stability criteria for the PML equation that preserves the dispersion relation.

1.3 Scope of Present Study

The main objective of this study is to illuminate the conditions needed to achieve both stability and accuracy of the PML condition. In terms of stability analysis, how the DRP stability criteria of the PML equation can be determined by a numerical scheme, so that the proper time step size as the absorption coefficient and Mach number change is determined analytically, will be presented. The choice of the time step is an important issue since it is directly related to the memory storage problem, where large memory is expected, especially for 3-D problems.

When it comes to the accuracy of the PML, We assume there are two possible factors that generate spurious reflected waves that affect the accuracy. One is that an incident wave entering the PML domain decays so drastic that the numerical scheme cannot preserve the dispersion relation and the other reason is the wave is not sufficiently damped at the endpoint of the PML. From this point of view, the optimum PML width that is sufficient to absorb the solution and its corresponding absorption coefficient is suggested. From this point of view, the optimum PML width that is sufficient to absorb

the solution and its corresponding absorption coefficient will be suggested. Compared with the fact that most previous studies have been done in the context of a parameter study to determine the proper the PML width (or profiles) and its corresponding absorption coefficient in the PML domain, this work has a point in that the factors that affect the accuracy of the PML are illuminated, and proper computational conditions are suggested for more efficient computation in the PML domain. The research is also extended to a generalized coordinate system, as well as Cartesian coordinates, in order to confirm that the criteria are still satisfactory in the PML region with a curvilinear grid.

This paper is organized as follows: In chapter 2, PML equations [18] from linearized Euler equations are elaborately derived in both Cartesian and generalized coordinate systems. In chapter 3, an explicit high-order optimized spatial discretization scheme and two different temporal discretization schemes are briefly reviewed. Then, a numerical stability analysis of the optimized scheme is conducted so as to discover the stability criteria of the PML that has complex eigenvalues. In chapter 4, a boundary closing issue is introduced, in order to apply the isotropic spatial scheme at the end of the PML region. In addition, the optimum PML width that is sufficient to absorb the solution and its corresponding absorption coefficient are discussed. Finally, in chapter 5, numerical examples are reported that demonstrate the validity of the prediction of the analysis condition. Concluding remarks are attached at the last part.

Chapter 2. Governing Equations

2.1 Linearized Euler Equations

For small-amplitude disturbances superimposed on a uniform mean flow of density ρ_0 , pressure p_0 , and velocity M in the x -direction. By assuming that the physical variables are a small, unsteady perturbation, the conventional linearized Euler equations (LEE) normalized by space $\Delta x, \Delta y$ and the speed of sound c for two-dimensional disturbances can be written as follows:

$$\frac{\partial \mathbf{U}}{\partial t} + \frac{\partial \mathbf{E}}{\partial x} + \frac{\partial \mathbf{F}}{\partial y} = 0, \quad (2.1)$$

where

$$\mathbf{U} = \begin{pmatrix} \rho \\ u \\ v \\ p \end{pmatrix}, \quad \mathbf{E} = \begin{pmatrix} \rho_0 u + \rho M \\ Mu + \frac{p}{\rho_0} \\ M_0 v \\ Mp + \gamma p_0 u \end{pmatrix}, \quad \text{and} \quad \mathbf{F} = \begin{pmatrix} \rho_0 v \\ 0 \\ \frac{p}{\rho_0} \\ \gamma p_0 v \end{pmatrix}. \quad (2.2)$$

The vector \mathbf{U} represents the physical variables of the solution vector. By introducing a general coordinate transformation $(x, y, t) \rightarrow (\xi, \eta, \tau)$, the LEEs are given by:

$$\frac{\partial \bar{\mathbf{U}}}{\partial \tau} + \frac{\partial \bar{\mathbf{E}}}{\partial \xi} + \frac{\partial \bar{\mathbf{F}}}{\partial \eta} = 0, \quad (2.3)$$

where

$$\bar{\mathbf{U}} = \frac{\mathbf{U}}{j}, \quad \bar{\mathbf{E}} = \frac{1}{j} [\xi_t \mathbf{U} + \xi_x \mathbf{E} + \xi_y \mathbf{F}], \quad \text{and} \quad \bar{\mathbf{F}} = \frac{1}{j} [\eta_t \mathbf{U} + \eta_x \mathbf{E} + \eta_y \mathbf{F}]. \quad (2.4)$$

After taking the Fourier-Laplace transform $\tilde{f}(k_x, k_y, \omega)$ of a function $f(x, y, t)$ on Eq. (2.1), and organizing the transformed equation into a system of linear algebraic equations, we can calculate the eigenvalues, from which the well-known dispersion relations for LEEs are derived. The dispersion relations for plane waves of the form $\mathbf{u}_0 e^{i(k_x x + k_y y - \omega t)}$ are

$$(\omega - Mk_x)^2 - k_x^2 - k_y^2 = 0 \quad (2.5)$$

for the acoustic waves, and

$$\omega - Mk_x = 0 \quad (2.6)$$

for the vorticity and entropy waves.

2.2 Derivation of PML Equations

2.2.1 Complex Change of Variables

In this research, the PML equations constructed by a complex change of variables [27, 28] are used. If we consider only the x-direction, the complex change of variable is defined as:

$$x \rightarrow \hat{x} + \frac{i}{\omega} \int_{\hat{x}_0}^{\hat{x}} \sigma_{\hat{x}} d\hat{x}, \quad (2.7)$$

where σ is the absorption function, which is always positive, and x_0 is located at the interface of the Euler and the PML domains. Since it is known that the wave is a function of $e^{i(k_x x - \omega t)}$, under a complex change of variables (Eq. (2.7)), and expressing \bar{x} in terms of the original variable x , it becomes

$$e^{i(k_x x - \omega t)} e^{-\frac{k_x}{\omega} \int_{x_0}^x \sigma_x dx}. \quad (2.8)$$

Thus, this augmented factor $e^{-\frac{k_x}{\omega} \int_{x_0}^x \sigma_x dx}$ plays the role of exponentially damping the wave in the PML zone. In order to reduce the amplitude of the wave in the PML region, k_x/ω and $\int_{x_0}^x \sigma_x dx$ must have the same sign. Here, the sign of $\int_{x_0}^x \sigma_x dx$ is determined by the direction of propagation. Since the direction of propagation of a dispersive wave is the same as that of group velocity, the necessary condition can be expressed as

$$\frac{k_x}{\omega} \frac{d\omega}{dk_x} > 0. \quad (2.9)$$

or equivalently,

$$\frac{\omega}{k_x} \frac{d\omega}{dk_x} > 0. \quad (2.10)$$

That is, the phase velocity (ω/k_x) and group velocity ($d\omega/dk_x$) must be consistent and in the same direction. Otherwise, any wave that propagates into the PML equations will diverge when its phase and group velocities are not in the same direction. Hence, when deriving the PML equation's dispersion relation, a relation between ω and k_x of the spatial variables should be derived.

2.2.2 Space-Time Transformation

From the dispersion relation of Eq. (2.5), the relationship between ω and k_x for various modes of k_y when there is no mean flow is plotted in Fig. 2.1. We can find that ω/k_x and $d\omega/dk_x$ have the same sign for all range of k_x . However, when $M = 0.5$, we can find there is a range in which inconsistent ω/k_x and $d\omega/dk_x$ have different signs in Fig. 2.2(a). Hence, the proper transformation, called the space-time transformation, that allows for a consistency of sign becomes inevitable [18].

The general form of the space-time transformation is expressed as

$$t \rightarrow \bar{t} - \beta x. \quad (2.11)$$

When the solution is a function of $e^{i(k_x x - \omega t)}$, in wavenumber space, Eq. (2.11) can be expressed as

$$\begin{aligned} \omega &\rightarrow \bar{\omega}. \\ k_x &\rightarrow \bar{k}_x - \beta \omega. \end{aligned} \quad (2.12)$$

From [16, 29, 30], β is defined as

$$\beta = \frac{M}{1 - M^2} \quad (2.13)$$

for uniform mean flow.

In Fig. 2.2(b), the relationship between transformed $\bar{\omega}$ and \bar{k}_x for various modes of k_y are plotted with $M = 0.5$. Compared to Fig. 2.1(a), there is no range where inconsistent ω/k_x and $d\omega/dk_x$ values have different signs. The dispersion relation

of the vorticity and entropy waves are not considered since they unconditionally satisfy Eq. (2.10) in the presence of parallel uniform mean flow.

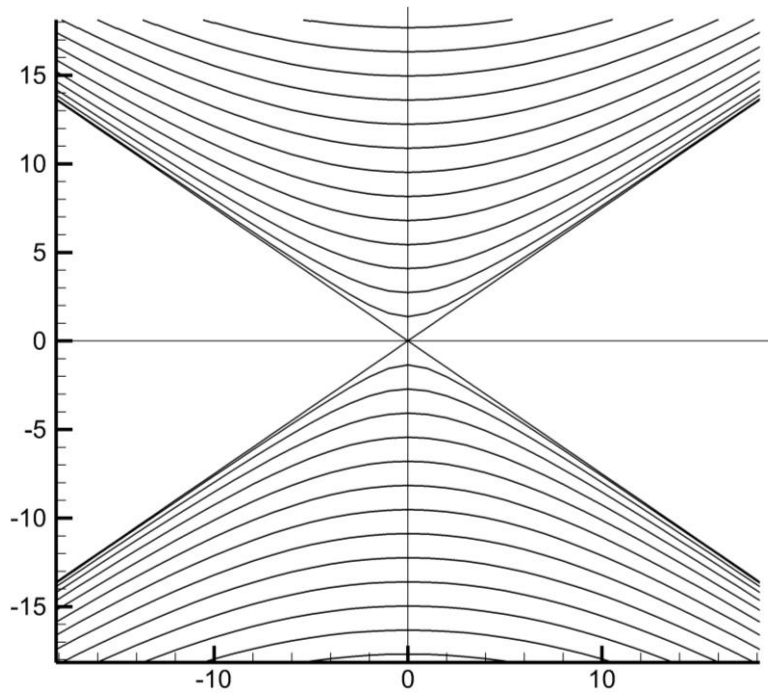


Fig. 2. 1 The relationship between ω and k_x for various modes of k_y without mean flow

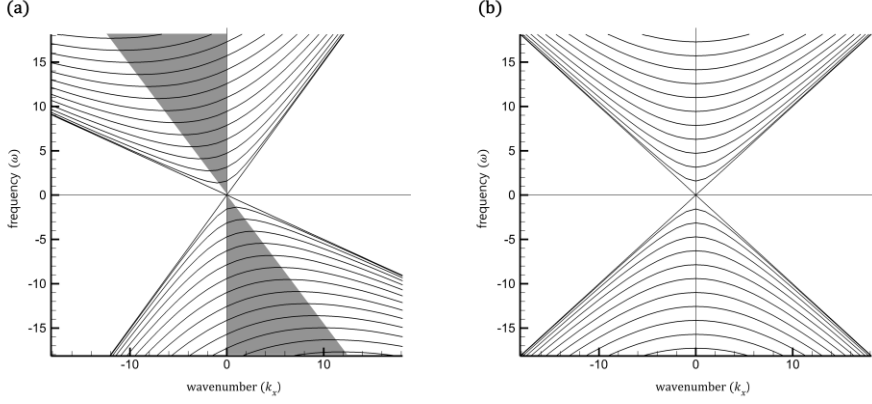


Fig. 2. 2 The relationship between ω and k_x for various modes of k_y with mean flow : no transformation (a) and space-time transformed (b)

2.2.3 Stable PML equations

The LEE in Eq. (2.1) can also be expressed in a non-conservative form as:

$$\frac{\partial \mathbf{U}}{\partial t} + \mathbf{A} \frac{\partial \mathbf{U}}{\partial x} + \mathbf{B} \frac{\partial \mathbf{U}}{\partial y} = \mathbf{0}, \quad (2.14)$$

where

$$\mathbf{A} = \begin{pmatrix} M_0 & \rho_0 & 0 & 0 \\ 0 & M_0 & 0 & 1/\rho_0 \\ 0 & 0 & M_0 & 0 \\ 0 & \gamma p_0 & 0 & M_0 \end{pmatrix} \text{ and } \mathbf{B} = \begin{pmatrix} 0 & 0 & \rho_0 & 0 \\ 0 & 0 & 0 & 0 \\ 0 & 0 & 0 & 1/\rho_0 \\ 0 & 0 & \gamma p_0 & 0 \end{pmatrix}. \quad (2.15)$$

From the complex change of variables, the complex term with the absorption function is added to the spatial variables. The partial derivatives of \hat{x} with respect to the original variables can be obtained from Eq. (2.7) as:

$$\frac{\partial \hat{x}}{\partial x} = \frac{1}{\left(1 + \frac{i}{\omega} \sigma_{\hat{x}}\right)}, \quad \frac{\partial \hat{x}}{\partial y} = 0, \text{ and } \frac{\partial \hat{x}}{\partial t} = 0. \quad (2.16)$$

Using a similar approach in the y-direction,

$$\frac{\partial \hat{y}}{\partial x} = 0, \quad \frac{\partial \hat{y}}{\partial y} = \frac{1}{\left(1 + \frac{i}{\omega} \sigma_{\hat{y}}\right)}, \text{ and } \frac{\partial \hat{y}}{\partial t} = 0. \quad (2.17)$$

The partial derivatives of \bar{t} by space-time transformation Eq. (2.11) can also be expressed as

$$\frac{\partial \bar{t}}{\partial x} = \beta, \quad \frac{\partial \bar{t}}{\partial y} = 0, \text{ and } \frac{\partial \bar{t}}{\partial t} = 1. \quad (2.18)$$

When the total derivative of the solution vector is

$$\begin{aligned} \frac{\partial \mathbf{U}}{\partial x} &= \frac{\partial \mathbf{U}}{\partial \hat{x}} \frac{\partial \hat{x}}{\partial x} + \frac{\partial \mathbf{U}}{\partial \hat{y}} \frac{\partial \hat{y}}{\partial x} + \frac{\partial \mathbf{U}}{\partial \bar{t}} \frac{\partial \bar{t}}{\partial x}, \\ \frac{\partial \mathbf{U}}{\partial y} &= \frac{\partial \mathbf{U}}{\partial \hat{x}} \frac{\partial \hat{x}}{\partial y} + \frac{\partial \mathbf{U}}{\partial \hat{y}} \frac{\partial \hat{y}}{\partial y} + \frac{\partial \mathbf{U}}{\partial \bar{t}} \frac{\partial \bar{t}}{\partial y}, \\ \frac{\partial \mathbf{U}}{\partial t} &= \frac{\partial \mathbf{U}}{\partial \hat{x}} \frac{\partial \hat{x}}{\partial t} + \frac{\partial \mathbf{U}}{\partial \hat{y}} \frac{\partial \hat{y}}{\partial t} + \frac{\partial \mathbf{U}}{\partial \bar{t}} \frac{\partial \bar{t}}{\partial t}, \end{aligned} \quad (2.19)$$

by replacing Eq. (19) into the non-conservative form of the LEE (Eq. (14)), it becomes

$$\frac{\partial \mathbf{U}}{\partial \bar{t}} + \mathbf{A} \left(\frac{1}{\left(1 + \frac{i}{\omega} \sigma_{\hat{x}}\right)} \frac{\partial \mathbf{U}}{\partial \hat{x}} + \beta \frac{\partial \mathbf{U}}{\partial \bar{t}} \right) + \mathbf{B} \left(\frac{1}{\left(1 + \frac{i}{\omega} \sigma_{\hat{y}}\right)} \frac{\partial \mathbf{U}}{\partial \hat{y}} \right) = \mathbf{0}. \quad (2.20)$$

After multiplying Eq. (20) by $(1 + i/\omega\sigma_{\hat{x}})(1 + i/\omega\sigma_{\hat{y}})$, and performing some simple calculations in the frequency domain, it is modified to be

$$\begin{aligned} (\mathbf{I} + \beta \mathbf{A}) \left[\frac{\partial \mathbf{U}}{\partial \bar{t}} + (\sigma_{\hat{x}} + \sigma_{\hat{y}}) \mathbf{U} + \sigma_{\hat{x}} \sigma_{\hat{y}} \mathbf{q} \right] + \mathbf{A} \left(\frac{\partial \mathbf{U}}{\partial \hat{x}} + \sigma_{\hat{y}} \frac{\partial \mathbf{q}}{\partial \hat{x}} \right) \\ + \mathbf{B} \left(\frac{\partial \mathbf{U}}{\partial \hat{y}} + \sigma_{\hat{x}} \frac{\partial \mathbf{q}}{\partial \hat{y}} \right) = \mathbf{0}, \text{ and} \end{aligned} \quad (2.21)$$

$$\frac{\partial \mathbf{q}}{\partial t} = \mathbf{U}, \quad (2.22)$$

where \mathbf{q} is the only auxiliary variable needed inside the PML domain.

Finally, by denoting the changed variables to the original variables, and replacing the transformed variables with the original variables, the stable PML equation is expressed as:

$$\begin{aligned} \frac{\partial \mathbf{U}}{\partial t} + \mathbf{A} \frac{\partial \mathbf{U}}{\partial x} + \mathbf{B} \frac{\partial \mathbf{U}}{\partial y} + \sigma_y \mathbf{A} \frac{\partial \mathbf{q}}{\partial x} + \sigma_x \mathbf{B} \frac{\partial \mathbf{q}}{\partial y} + (\sigma_x + \sigma_y) \mathbf{U} + \sigma_x \sigma_y \mathbf{q} \\ + \sigma_x \beta \mathbf{A} (\mathbf{U} + \sigma_y \mathbf{q}) = \mathbf{0}. \end{aligned} \quad (2.23)$$

Cartesian computational domain with PML regions is illustrated in Fig 2.3.

In generalized coordinates, $(x, y, t) \rightarrow (\xi, \eta, \tau)$, the conservative form of the PML equations for uniform mean flow takes the following form:

$$\frac{\partial \bar{\mathbf{U}}}{\partial \tau} + \frac{\partial \bar{\mathbf{E}}}{\partial \xi} + \frac{\partial \bar{\mathbf{F}}}{\partial \eta} + \bar{\mathbf{H}} = 0, \quad (2.24)$$

where

$$\bar{\mathbf{U}} = \frac{\mathbf{U}}{J}, \quad \bar{\mathbf{E}} = \frac{1}{J} \begin{bmatrix} \xi_x (M_0 \rho + u + \sigma_\eta (M_0 q_\rho + q_u)) + \xi_y (v + \sigma_\eta q_v) \\ \xi_x (M_0 u + p + \sigma_\eta (M_0 q_u + q_p)) + \xi_y (v + \sigma_\xi q_v) \\ \xi_x (M_0 v + u + \sigma_\eta (M_0 q_v + q_u)) + \xi_y (p + \sigma_\eta q_p) \\ \xi_x (M_0 p + u + \sigma_\eta (M_0 q_p + q_u)) + \xi_y (v + \sigma_\eta q_v) \end{bmatrix},$$

$$\bar{\mathbf{F}} = \frac{1}{J} \begin{bmatrix} \eta_x (M_0 \rho + u + \sigma_\xi (M_0 q_\rho + q_u)) + \eta_y (v + \sigma_\xi q_v) \\ \eta_x (M_0 u + p + \sigma_\xi (M_0 q_u + q_p)) + \xi_y (v + \sigma_\xi q_v) \\ \eta_x (M_0 v + u + \sigma_\xi (M_0 q_v + q_u)) + \eta_y (p + \sigma_\xi q_p) \\ \eta_x (M_0 p + u + \sigma_\xi (M_0 q_p + q_u)) + \eta_y (v + \sigma_\xi q_v) \end{bmatrix}, \text{ and} \quad (2.25)$$

$$\bar{\mathbf{H}} = \frac{1}{J} \begin{bmatrix} (\sigma_\xi + \sigma_\eta) \rho + \sigma_\xi \sigma_\eta q_\rho + \beta \sigma_\xi (M_0 \rho + u + \sigma_\eta (M_0 q_\rho + q_u)) \\ (\sigma_\xi + \sigma_\eta) u + \sigma_\xi \sigma_\eta q_u + \beta \sigma_\xi (M_0 u + p + \sigma_\eta (M_0 q_u + q_p)) \\ (\sigma_\xi + \sigma_\eta) v + \sigma_\xi \sigma_\eta q_v + \beta \sigma_\xi (M_0 v + u + \sigma_\eta (M_0 q_v + q_u)) \\ (\sigma_\xi + \sigma_\eta) p + \sigma_\xi \sigma_\eta q_p + \beta \sigma_\xi (M_0 p + u + \sigma_\eta (M_0 q_p + q_u)) \end{bmatrix}.$$

To obtain the corresponding dispersion relation of the PML equation, the transformed variables should be expressed in wavenumber space first. Since $\partial/\partial x = ik_x$, the complex change of variables in wavenumber space can be written as

$$k_x \rightarrow \frac{k_x}{1 + \frac{i}{\omega} \sigma_x}. \quad (2.26)$$

Using the similar approach in the y-direction,

$$k_y \rightarrow \frac{k_y}{1 + \frac{i}{\omega} \sigma_y}. \quad (2.27)$$

By replacing the space-time transformation in Eq. (2.12) to Eqs. (2.26) and (2.27), we get

$$k_x \rightarrow \frac{k_x}{1 + \frac{i}{\omega} \sigma_x} \left(k_x + \frac{M}{1 - M^2} \omega \right) - \frac{M}{1 - M^2} \omega \text{ and } k_y \rightarrow \frac{k_y}{1 + \frac{i}{\omega} \sigma_y}. \quad (2.28)$$

The dispersion relation for Eq. (2.23) can be found, equivalently, by replacing k_x and k_y in Eq. (2.28), which becomes

$$\begin{aligned} \frac{(\omega + i\sigma_x)^2 (\omega + i\sigma_y)^2}{(1 - M^2)^2} - (\omega + i\sigma_y)^2 \left(k_x + \frac{M}{1 - M^2} \omega \right)^2 \\ - \frac{(\omega + i\sigma_x)^2}{1 - M^2} k_y^2 = 0 \end{aligned} \quad (2.29)$$

for the acoustic wave, and

$$\omega + \frac{i\sigma_x}{1 - M^2} - M k_x = 0 \quad (2.30)$$

for the vorticity and entropy waves. It is found that the root of the dispersion relations of the PML equations have complex value. Hence, from Eqs. (2.29) and (2.30), we can confirm that the phase velocity and group velocity are consistent. The details on the stability analysis can be found in [18].

$\sigma_x \neq 0$ $\sigma_y \neq 0$	$\sigma_x = 0,$ $\sigma_y \neq 0$ PML	$\sigma_x \neq 0$ $\sigma_y \neq 0$
$\sigma_x \neq 0$ $\sigma_y = 0$ PML	Linearized Euler Equations	$\sigma_x \neq 0$ $\sigma_y = 0$ PML
$\sigma_x \neq 0$ $\sigma_y \neq 0$	$\sigma_x = 0,$ $\sigma_y \neq 0$ PML	$\sigma_x \neq 0$ $\sigma_y \neq 0$

Fig. 2. 3 Cartesian computational domain governed by the linearized Euler equations enclosed by PMLs

Chapter 3. Numerical Methodology

3.1 Optimized Numerical Method

If the computational scheme and the governing equations have the same dispersion relation, then the numerical and exact solutions will have the same wave propagation characteristics, such as group and phase velocities. Accordingly, the so-called DRP scheme by Tam and Webb [12] has been developed for CAA, which preserves the wave propagation of the governing equations. In this chapter, a fourth-order DRP scheme will be discussed in wavenumber space, and an optimized Adams-Bashford fourth-order time discretization scheme will be reviewed in view of stability. Finally, numerical stability analysis will be introduced to preserve the dispersion relation in the PML equations.

3.1.1 Fourier Analysis of High-order Spatial Discretization

In aeroacoustics problems, what is needed for numerical stability is a finite difference scheme in space that has almost the same dispersion relation as the original partial differential equations [31]. For spatial discretization, we consider an optimized finite difference scheme, one which is broadly used for CAA. The optimized scheme, also known as the dispersion-relation-preserving (DRP) scheme [12], is expressed as:

$$\left(\frac{\partial f}{\partial x}\right)_i \cong \frac{1}{\Delta x} \sum_{j=-N_0}^N a_j f_{i+j}. \quad (3.1)$$

Now, by applying a Fourier transform to the above equation, and making use of the derivative and shifting theorems,

$$k^* \cong \frac{-i}{\Delta x} \sum_{j=-N_0}^N a_j e^{ij\alpha\Delta x} \quad (3.2)$$

where k^* is the effective wavenumber of the partial derivative and a_j is an optimized stencil that can be obtained by minimizing the integrated error E over a certain wave

number range e , where

$$E = \int_0^e |k^* \Delta x - k \Delta x| d(k \Delta x). \quad (3.3)$$

The conditions for E to be at a minimum are,

$$\frac{dE}{db_j} = 0 \quad \text{and } j = 1, 2, 3 \dots, N. \quad (3.4)$$

More optimization methods for the minimization of error can be found in [32, 33]. $N_0 = N$ for the central scheme, and $2N + 1$ is the number of stencils to be used. In Eq. (3.2), k^* represents the effective wavenumber. The maximum k^* the scheme can preserve depends on N , and the computational cost rises dramatically as the stencil size gets larger. Fig. 3.1 shows the effective wavenumbers ($k^* \Delta x$) versus the wavenumber ($k \Delta x$) of the partial derivative relations for several explicit optimized schemes [34]. A list of the maximum resolvable wavenumber ($k_c^* \Delta x$) and the maximum effective wavenumber ($k_{max}^* \Delta x$) are given in Table 1. $k_c^* \Delta x$ is found using the criterion: $|\alpha^* \Delta x - \alpha \Delta x| < 0.005$, $k_{max}^* \Delta x$ is the extremal value that affects the stability consideration, and $2\pi / \alpha_c^* \Delta x$ is a resolution, i.e., the minimum resolvable grid points per wavelength.

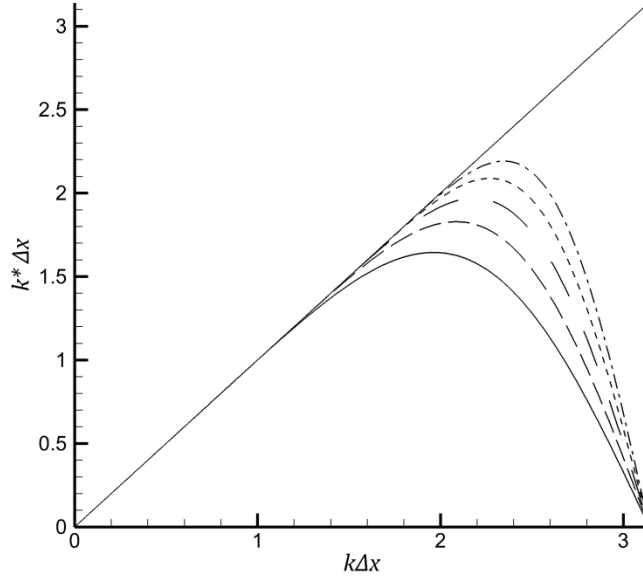


Fig. 3. 1 $k\Delta x$ versus $k^*\Delta x$: —, 7-point; - - -, 9-point; — — —, 11-point; - - -, 13-point; - . - . 15-point stencil.

Table 1 Values of $k_c^*\Delta x$ and $k_{max}^*\Delta x$ of central DRP scheme for different stencils

Spatial discretization	$k_c^*\Delta x$	$k_{max}^*\Delta x$	Resolution
7-point	1.16	1.64	5.4
9-point	1.42	1.82	4.4
11-point	1.63	1.97	3.9
13-point	1.80	2.08	3.5
15-point	1.96	2.19	3.2

3.1.2 Optimized Time Discretization Scheme

Since the DRP property is desirable for computing wave propagation problems, we focus on a particular time integration scheme that leads to the DRP property by an optimization process, and then calculate the stability diagram for the complex domain. Here, an optimized four-level time discretization multi-step (Adams–Bashford) method is used as the explicit time marching scheme.

Suppose the time evolution equation is written as

$$\frac{\partial \mathbf{u}}{\partial t} = \mathbf{F}(\mathbf{u}), \quad (3.5)$$

where \mathbf{u} is a vector of physical values and operator \mathbf{F} contains the discretization of the spatial derivatives. The time level is divided uniformly into time step Δt .

If the values of \mathbf{u} and du/dt are known at time $t, t - \Delta t, t - 2\Delta t$, and $t - 3\Delta t$, the four-level finite difference approximation can be written as

$$\mathbf{u}^{n+1} = \mathbf{u}^n + \Delta t \sum_{j=0}^3 b_j \left(\frac{\partial \mathbf{u}}{\partial t} \right)^{n-j}, \quad (3.6)$$

where b_j are constants to be determined for optimization. By applying the Laplace transform and shifting theorem to Eq. (3.6), we obtain:

$$-i \frac{i(e^{-i\omega\Delta t} - 1)}{\Delta t \sum_{j=0}^3 b_j e^{ij\omega\Delta t}} \tilde{\mathbf{u}} \cong \frac{d\tilde{\mathbf{u}}}{dt}. \quad (3.7)$$

Since the Laplace transform of the time derivative of \mathbf{u} is $i\omega\mathbf{u}$, by comparing the two sides of Eq. (3.7), it becomes:

$$\bar{\omega} \cong \frac{i(e^{-i\omega\Delta t} - 1)}{\Delta t \sum_{j=0}^3 b_j e^{ij\omega\Delta t}}, \quad (3.8)$$

where $\bar{\omega}$ is the effective angular frequency of Eq. (3.6). When the weighted integrated error E_w is defined as

$$E_w = \int_{-\zeta}^{\zeta} \{\lambda [Re(\bar{\omega}\Delta t - \omega\Delta t)]^2 + (1 - \lambda) [Im(\bar{\omega}\Delta t - \omega\Delta t)]^2\} d(\omega\Delta t), \quad (3.9)$$

where λ is the weight and ζ is the frequency range, we expect $\bar{\omega}$ to be a good approximation of ω . In order to minimize the weighted integrated error of Eq. (3.9) for a particular b_j , we let

$$\frac{dE_w}{db_j} = 0 \text{ and } j = 0,1,2,3. \quad (3.10)$$

Thus, Eq. (3.10) provides four equations for four coefficients b_j as a function of λ and ζ . Based on a consideration of the range of useful frequencies and numerical damping rate, the values $\lambda = 0.36$ and $\zeta = 0.5$ are recommended. As a result, the optimized values of the coefficients are

$$\begin{aligned} b_0 &= 2.30255809, \quad b_1 = -2.49100760, \\ b_2 &= 1.57434093, \text{ and } b_3 = -0.38589142. \end{aligned} \quad (3.11)$$

3.2 Numerical Stability Analysis

In this chapter, we will perform a stability analysis on the optimized multi-step method in order to find the stability criteria for the PML equations. To analyze the numerical errors, we consider the amplification factor in the wavenumber domain. Applying the model problem to Eq. (3.5) leads to

$$\frac{\partial \mathbf{u}}{\partial t} = \lambda \mathbf{u}, \quad (3.12)$$

where λ is the eigenvalue of the operator $\mathbf{F}(\mathbf{u})$, which can be replaced by $-i\omega$ from the exact solution. If we replace the partial derivative term of Eq. (3.6) with Eq. (3.12), the Eq. (3.6) becomes

$$\mathbf{u}^{n+1} = \mathbf{u}^n - i\omega\Delta t \sum_{j=0}^3 b_j \mathbf{u}^{n-j}. \quad (3.13)$$

Reorganizing the equation (3.13) with respect to amplification factor, $\gamma = \mathbf{u}^{n+1}/\mathbf{u}^n$, it can be written in the form as follows:

$$i \frac{\gamma^4}{\omega\Delta t} - \left(\frac{i}{\omega\Delta t} + b_0 \right) \gamma^3 - b_1 \gamma^2 - b_2 \gamma - b_3 = 0. \quad (3.14)$$

Solving this biquadratic equation, we get four different roots γ_j ($j = 1, 2, 3, 4$), three of which are spurious roots. Since the exact amplification factor is found to be

$$\gamma_e = e^{-i\omega\Delta t}, \quad (3.15)$$

we can compare the numerical and exact amplification factors as

$$\frac{\gamma}{\gamma_e} = \varepsilon e^{i\delta}. \quad (3.16)$$

In this expression, ε represents the dissipation error, which should be 1, and δ is the dispersion error, which should be 0. They are functions of $\omega\Delta t$, and the properties of the scheme are only affected by the coefficients b_j . The dissipation and dispersion errors of the optimized fourth-order multi-step scheme for the real value of $\omega\Delta t$ are plotted in Fig. 3.2.

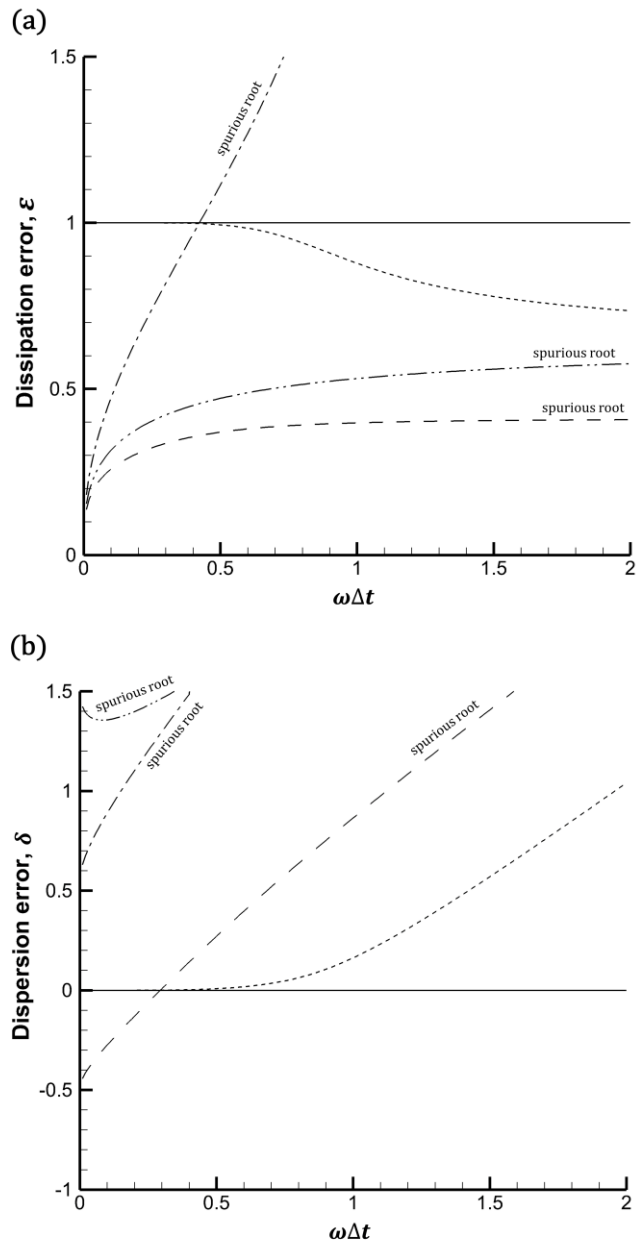


Fig. 3. 2 (a) Dissipation and (b) dispersion errors of optimized fourth-order multi-step.

In the range $\omega\Delta t \leq 0.41$, the dissipation error of all solutions are less than 1, which is called the stability limit. For accuracy, we take the criterion $|\varepsilon - 1| < 0.005$ for dissipation accuracy and $|\delta| < 0.005$ for dispersion accuracy. In the range $\omega\Delta t \leq 0.44$, it is shown that the numerical solution is time-accurate. Hence, we find that the stability limit encompasses the accuracy limit in this case.

However, comparing that the roots of the dispersion relations for the LEEs have only real values of angular frequency, the dispersion relation of the PML equation has complex roots because of the complex change of variables. In case $\omega\Delta t$ is a complex value, we need to consider both real and imaginary parts of the eigenvalue in Eq. (3.12). To include the general case of the stability condition, the stability diagram can be drawn in the complex plane. The stability diagram of the optimized fourth-order multi-step method is numerically calculated for $\omega\Delta t = \text{Re}(\omega\Delta t) + i\text{Im}(\omega\Delta t)$ in Fig. 3.3. Only the negative imaginary part is plotted, since the solution having time dependence of the form $e^{-i\omega\Delta t}$ will diverge in the range $\text{Im}(\omega\Delta t) > 0$.

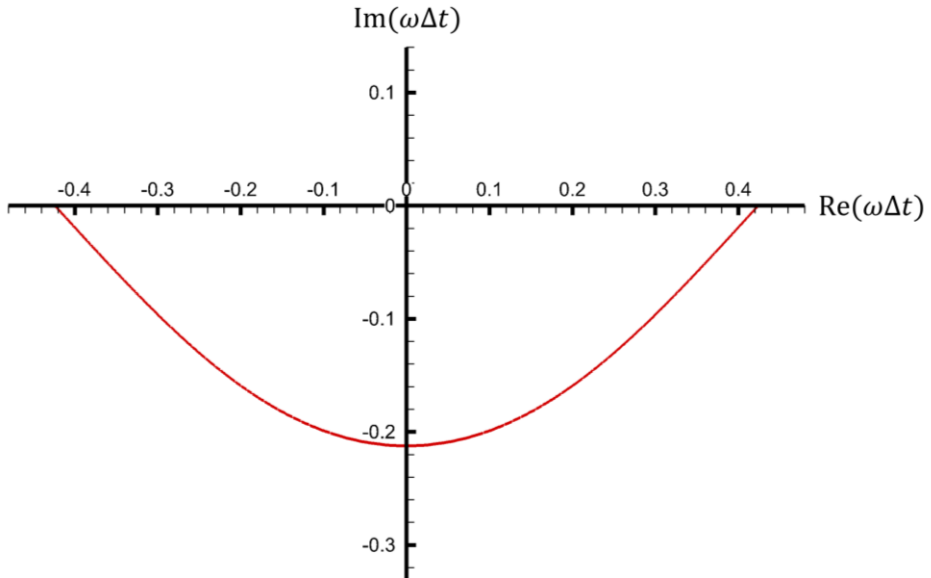


Fig. 3. 3 Region of stability in the complex plane.

From the roots of the dispersion relation of the PML equations in Eq. (2.29), a root that satisfies the condition $\text{Re}(\omega) \geq 0$ is expressed as

$$\omega = \text{Re}(\omega) + i\text{Im}(\omega), \quad (3.17)$$

where the complex value ω becomes a maximum for a given σ_x , σ_y , Δx , Δy , and M when

$$k_x = k_{x,max} \text{ and } k_y = k_{y,max}. \quad (3.18)$$

Thus, the inequality

$$|\omega| \leq \omega_{max}(M, \sigma_{max}, k_{max}, \Delta x, \Delta y) \quad (3.19)$$

holds true. Here, ω_{max} is the maximum physical complex root that qualifies the dispersion relation of the PML equations, which is the function of the Mach number, absorption coefficient, wavenumbers, and grid sizes. By multiplying Δt by the inequality Eq. (3.19), and comparing this with the stability criteria of Fig.3.3, it is straightforward that $\omega_{max}\Delta t$ should be located on the upper side of the stability footprint. This consideration will lead to the condition of determining Δt , not only for the Euler domain, but also for the PML region.

Now we can deduce the relationship between Mach number and maximum absorption coefficient for stability, $\tilde{\sigma}$. Regardless of the profile of absorption function, σ_x or σ_y , the maximum value of it becomes $\sigma_{max} = \tilde{\sigma}(1 - M^2)$ at the end of the PML domain since it smoothly increases. A factor of $(1 - M^2)$ is multiplied since the absorption rate in x-direction is increased by a factor of $1/(1 - M^2)$. For a given Δt , maximum absorption coefficients ($\tilde{\sigma}$) are plotted with respect to Mach number in Fig. 3.4.

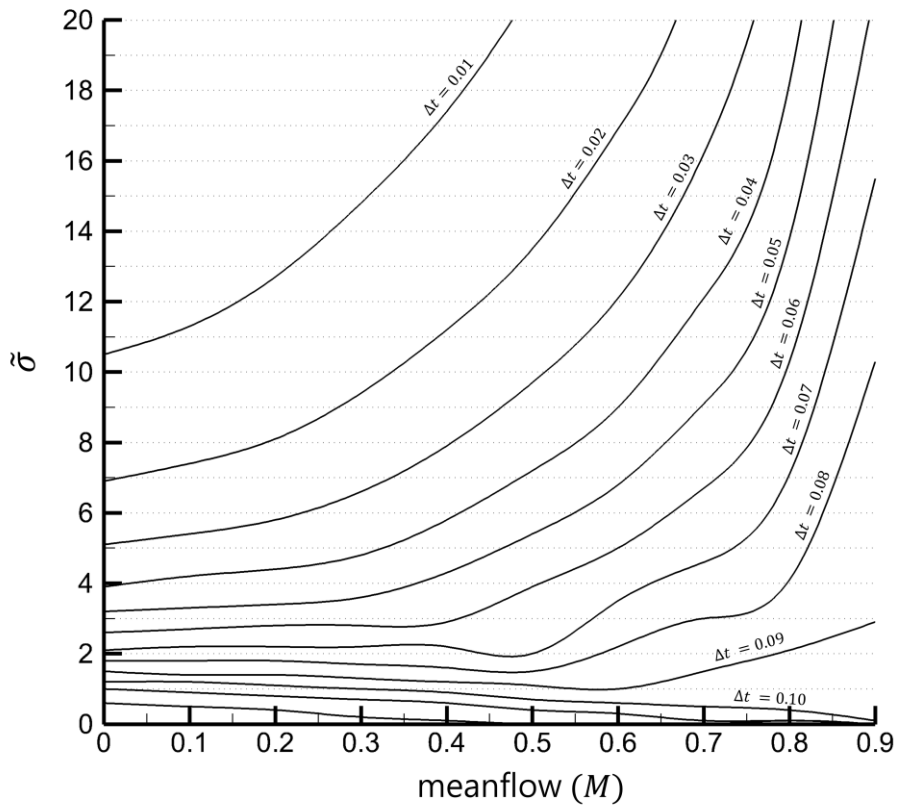


Fig. 3. 4 Maximum stable absorption coefficients with respect to mean flow.

Chapter 4. Non-reflective PML Conditions

4.1 End Condition of PML Boundary

Since there is an apparent discontinuity at the border of the computational domain where the PML region ends, it is inevitable to apply boundary-closure treatment. One way is to use anisotropic schemes [35, 36], which is the method generally adopted for end conditions. In the case of the upwind scheme, however, the imaginary part of the effective wavenumber remains. In the case of a 7-point optimized upwind DRP scheme [4], the imaginary part pertains when $k\Delta x$ is 2.1, which is where $k^*\Delta x$ becomes the maximum wavenumber. Thus, the maximum wavenumber with an imaginary part cannot formulate the inequality $|k^*\Delta x - k\Delta x| < 0.005$ that is necessary for the stability criteria in Fig. 3. Here, we suggest an alternative, so that the stability of the PML is not affected by the imaginary wavenumber of the anisotropic scheme. Since the amount of absorption by the PML in the x-direction is defined as

$$e^{-\int_{x_0}^x \sigma_x dx}, \quad (4.1)$$

the physical value in the PML region will eventually be damped to zero for sufficient PML width. The proper PML width to damp out the solution will be discussed later. If we assume that we provide the proper PML width that makes the value at the endpoint of the PML region to be approximately zero in the numerical calculation, we can say the points after the endpoint are always zero. Actually, this assumption is straightforward because spurious waves would be reflected unless they were sufficiently decayed in the PML region. From this assumption, we can now apply an isotropic scheme at the end of the boundary by setting $(N - 1)/2$ auxiliary null ghost points for an N-point central spatial discretization scheme. The schematic diagrams of the 7-point central and upwind stencils are illustrated in Fig. 4.1. For the conventional way of using the upwind method at the boundary, the stencils stay inside the PML region. In the case of the central stencil,

we set three null-ghost points that have zero values to be extended from the border of the PML region to the outside.

This null-ghost point approach is verified by numerical simulation in the PML region. The following Gaussian pulse, which is $20\Delta x$ away from the PML region, is propagated to the PML:

$$p = \rho = \exp\left[(-\ln 2)\frac{(x - 20)^2 + y^2}{9}\right], u = v = 0. \quad (4.2)$$

In Fig. 4.2, the pressure error of the numerical solution p , and the reference solution p_{ref} , as a function of time is plotted for two selected points located at **(A)** and **(B)** of Fig. 4.1. The pressure error is written as $|p_{ref} - p|$, normalized by p_0 . The reference solution is obtained by using a larger computational domain so that it is not affected by any boundary effects. The absorption function is defined as $\sigma_x = (x/D)^2$ in the PML region, with a width of D . The 7-point DRP central and upwind scheme for the spatial derivatives are used. We find that the pressure error with the central scheme shows even better accuracy than the optimized upwind scheme for both points. This simple but powerful assumption reveals that there is no need to use any other boundary closing treatment, since the acoustic pressure converges into an infinitesimal value at the end of the PML region. Moreover, it reduces the computational cost, since less than $(N + 1)/2$ points are calculated at the endpoints. As a result, by using this approach, we can implement the stability analysis for the PML region without considering the imaginary part of the wavenumber.

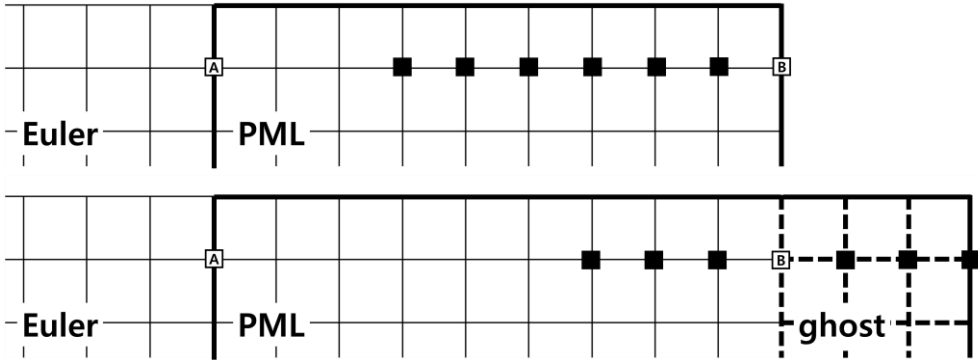


Fig. 4. 1 Schematic diagram of 7-point central (upper) and upwind (lower) stencils located in the PML region

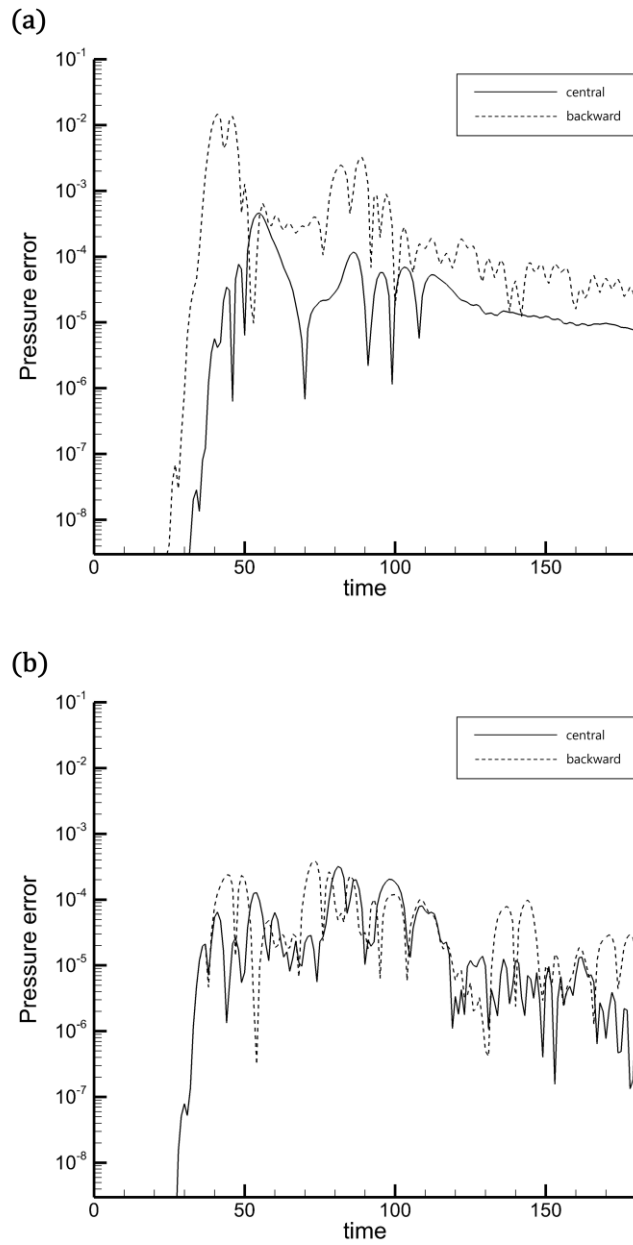


Fig. 4. 2 The evolution of pressure error at the point (A), (a) and (B), (b)

4.2 Analytical Approach on Absorption Coefficient

There are two possible factors that generate spurious reflected waves that affect the accuracy of the PML. One occurs when the decaying rate in the PML domain is too drastic to make the absorption increase smoothly in numerical discretization, and the other occurs when the wave is not sufficiently damped at the endpoint of the PML. From Eq. (2.7), it is shown that the solution in the PML domain is damped by a factor of

$$e^{-\int_{x_0}^x \sigma_x dx}, \quad \sigma_x = \tilde{\sigma}\Gamma(x), \quad (4.3)$$

where $\tilde{\sigma}$ is the absorption coefficient which is a constant value, and $\Gamma(x)$ is the absorption profile. The profile of this absorption function should be such that $\sigma_x(x_0) = \frac{d\sigma_x(x_0)}{dx} = 0$ to be matched at the interface of physical domain and the PML domain.

In this chapter, we will investigate the absorption function that plays an important role in the performance of the PML such that the optimum PML width for the efficiency of computation is determined. There are variety of commonly used absorption profiles such as power-law [37,38] and sine power-law profiles [39] as follows:

$$\Gamma(x) = \left(\frac{x}{D}\right)^n \quad \text{and} \quad \Gamma(x) = \sin^n\left(\frac{\pi}{2D}\right), \quad (4.4)$$

where D is the PML width and n is the positive real value. Thus, we can determine the minimum PML width by appropriate choice of $\tilde{\sigma}$ and n . The power-law profiles are considered in this research for various $\tilde{\sigma}$.

4.2.1 Maximum Absorption Coefficient

Since the Euler equations and the PML equations are different governing equations, they have different analytical solutions. In Fig. 4.3, several points for a 7-point central scheme that use both the Euler and the PML solutions to get partial derivatives are illustrated. If each point is denoted as l , and the solutions to the Euler equations and a set of different solutions to the PML equations with respect to grid point i are f and φ_i , respectively, the gradient at l can be expressed as

$$\left(\frac{\partial \varphi}{\partial x}\right)_l \cong \frac{1}{\Delta x} \left(\sum_{j=-N}^{-l} a_j f_{l+j} + \sum_{j=-l+1}^N a_j \varphi_{l+j} \right), \quad (4.5)$$

where the solution of the PML equations, φ_j , can be analytically expressed as

$$\varphi_j = f_j e^{-\int_0^{j\Delta x} \sigma_{j\Delta x} d(j\Delta x)}. \quad (4.6)$$

By replacing φ_j of Eq. (4.6) into Eq. (4.5),

$$\begin{aligned} \left(\frac{\partial f}{\partial x}\right)_l e^{-\int_0^{l\Delta x} \sigma_{j\Delta x} d(j\Delta x)} \\ \cong \frac{1}{\Delta x} \left(\sum_{j=-N}^{-l} a_j f_{l+j} + \sum_{j=-l+1}^N a_j f_{l+j} e^{-\int_0^{(l+j)\Delta x} \sigma_{j\Delta x} d(j\Delta x)} \right), \end{aligned} \quad (4.7)$$

and applying the Fourier transform,

$$\begin{aligned} i\alpha \tilde{f}(\alpha) &\cong \frac{1}{\Delta x} \left(\sum_{j=-N}^{-l} a_j e^{ij\alpha\Delta x} \right. \\ &\quad \left. + \sum_{j=-l+1}^N a_j e^{ij\alpha\Delta x - \int_0^{(l+j)\Delta x} \sigma_{j\Delta x} d(j\Delta x)} \right) e^{\int_0^{l\Delta x} \sigma_{j\Delta x} d(j\Delta x)} \tilde{f}(\alpha) \\ &\equiv i\alpha_l^* \tilde{f}(\alpha), \end{aligned} \quad (4.8)$$

where α_k^* is denoted as effective wavenumber at grid point k .

In the Euler domain ($\sigma_{j\Delta x} = 0$),

$$\alpha_l^* = \alpha_{l+1}^* = -\frac{i}{\Delta x} \left(\sum_{j=-N}^N a_j e^{ij\alpha\Delta x} \right), \quad (4.9)$$

where, the effective wavenumber is consistent regardless of the positions.

In the PML domain, on the other hand, α_k^* and α_{k+1}^* are

$$\alpha_l^* = -\frac{i}{\Delta x} \left(\sum_{j=-N}^{-l} a_j e^{ij\alpha\Delta x} + \sum_{j=-l+1}^N a_j e^{ij\alpha\Delta x - \int_0^{(l+j)\Delta x} \sigma_{j\Delta x} d(j\Delta x)} \right) e^{\int_0^{l\Delta x} \sigma_{j\Delta x} d(j\Delta x)}. \quad (4.10)$$

and

$$\alpha_{l+1}^* = -\frac{i}{\Delta x} \left(\sum_{j=-N}^{-l-1} a_j e^{ij\alpha\Delta x} + \sum_{j=-l}^N a_j e^{ij\alpha\Delta x - \int_0^{(l+1+j)\Delta x} \sigma_{j\Delta x} d(j\Delta x)} \right) e^{\int_0^{(l+1)\Delta x} \sigma_{j\Delta x} d(j\Delta x)}, \quad (4.11)$$

where α_k^* is not consistent with α_{k+1}^* since the absorption function varies with respect to the grid points. For the consistency of the effective wavenumbers, we assume that the absorption at each grid should be small enough to minimize the discrepancy of α_l^* and α_{l+1}^* . Thus, the maximum discrepancy of effective wavenumbers between two adjacent grid point is denoted as wavenumber error, ε and it is expressed as

$$\varepsilon = \mu \max(|\alpha_{l+1}^* \Delta x - \alpha_l^* \Delta x|), \quad (4.12)$$

where a damping factor, $\mu = e^{-\int_0^{l\Delta x} \sigma_{j\Delta x} d(j\Delta x)}$ is multiplied since the error decreases by a factor of the absorption by PML. To ensure accuracy in the discretized space with the optimized 7-point stencil, we define the value of ε should provide an approximation as good as $\varepsilon \leq 0.005$ up to $\alpha\Delta x = 1.16$. Otherwise, the incident wave will show non-physical solutions at the interface. ε for various absorption profiles are plotted for $0 \leq \alpha\Delta x \leq 1.16$ in Fig. 4.4. We should note that the error becomes larger as the absorption coefficient increases, and an overly large absorption at a grid point that incurs the sharp change of solution can be attributed to the discretization errors. This implies that there is a maximum value of $\tilde{\sigma}$ with respect to the PML width (D) that guarantees

the accuracy at each grid point. Hence, the numerical calculation is conducted to obtain the corresponding maximum absorption coefficient $\tilde{\sigma}_{max}$ for various PML widths. In Fig. 4.5, the allowable maximum absorption coefficients are plotted. It might seem that any size of width is possible as long as $\tilde{\sigma}$ is less than the maximum value, $\tilde{\sigma}_{max}$, but the minimum absorption coefficient exists that sufficiently damp out the solution and it will restrict the width.

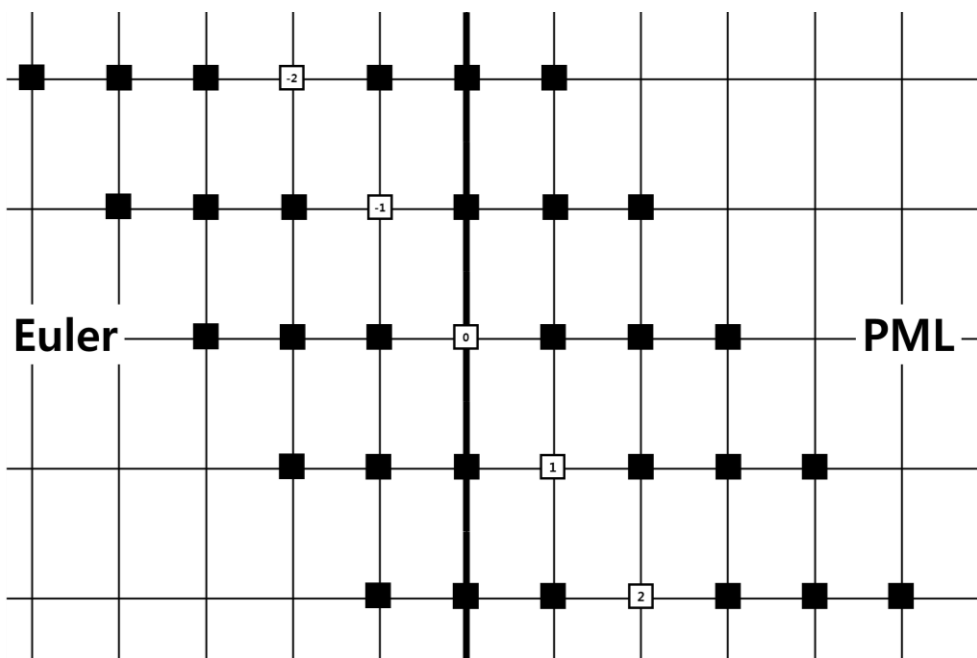


Fig. 4. 3 An illustration of stencils to be used for derivatives near the interface.

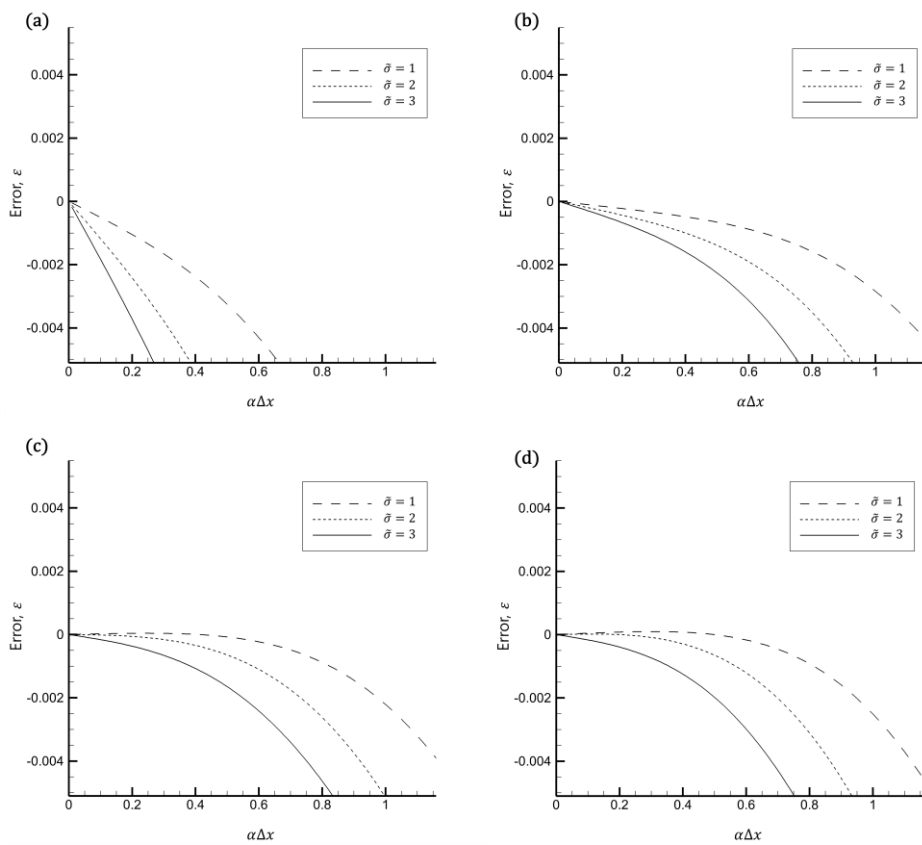


Fig. 4. 4 Wavenumber errors (ϵ) for linear (a), square (b), cubic (c) and quartic (d) absorption profiles.

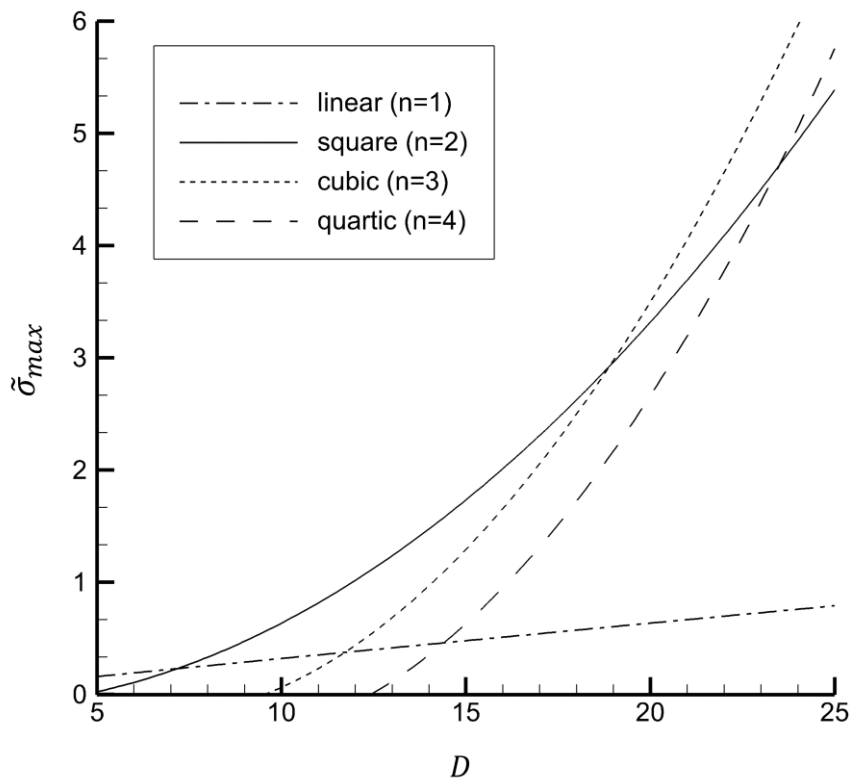


Fig. 4. 5 The maximum absorption coefficients.

4.2.2 Minimum Absorption Coefficient

When the exact solution of acoustic wave of the two-dimensional LEE is written as

$$p(x, y, t) = \frac{p_0}{2\alpha} \int_0^\infty e^{-\xi^2/4\alpha} \cos(\xi t) J_0(\xi \eta) \xi d\xi, \quad (4.13)$$

where $\alpha = (ln2)/9$, $\eta = [(x - Mt)^2 + y^2]^{1/2}$, and J_0 is the Bessel functions of 0, we can also derive the exact solution of the PML equation in the x-direction as

$$p_{pml}(x, y, t) = p(x, y, t) e^{-\int_{\delta_0}^x \sigma_x dx}, \quad (4.14)$$

where σ_x is the absorption coefficient and δ_0 is the first grid point of the PML domain. In general, the absorption coefficient is defined as a smooth function. If we let $\sigma_x = \tilde{\sigma}(x/D)^n$ in which D is the PML width, Eq. (4.14) becomes

$$p_{pml}(x, y, t) = p(x, y, t) e^{-\frac{\tilde{\sigma} x^{n+1}}{(n+1)D^n}}. \quad (4.15)$$

At the endpoint $x = \delta_l$, p_{pml} normalized by p_0 , which is a value at δ_0 , can be written as

$$\frac{p_{pml}(\delta_l, y, t)}{p_0} = \frac{p(\delta_l, y, t)}{p_0} e^{-\frac{\tilde{\sigma} \delta_l^{n+1}}{(n+1)D^n}}. \quad (4.16)$$

From the geometric spreading law of plane wave propagation, the value of p/p_0 can be expressed as $r^{-1/2}$. The results of Eq. (4.16) for various absorption profiles with respect to the PML width (D) are plotted in Fig. 4.6. From this analytical solution, we find that at the endpoint of the PML domain, the wave converges to zero differently with respect to $\tilde{\sigma}$. Since we are dealing with a fourth-order spatial discretization scheme, the perfectly absorbing condition can be defined as $p_{pml}/p_0 < 0.001$. Hence, the minimum value of $\tilde{\sigma}$ that satisfies the perfectly absorbing condition at the end of the boundary can be obtained by numerical calculation. In Fig. 4.7, the minimum absorption coefficient $\tilde{\sigma}_{min}$ is plotted for various PML widths. It is shown that a short width requires a large absorption coefficient since there is not enough length to absorb the outgoing waves and this varies with the power n .

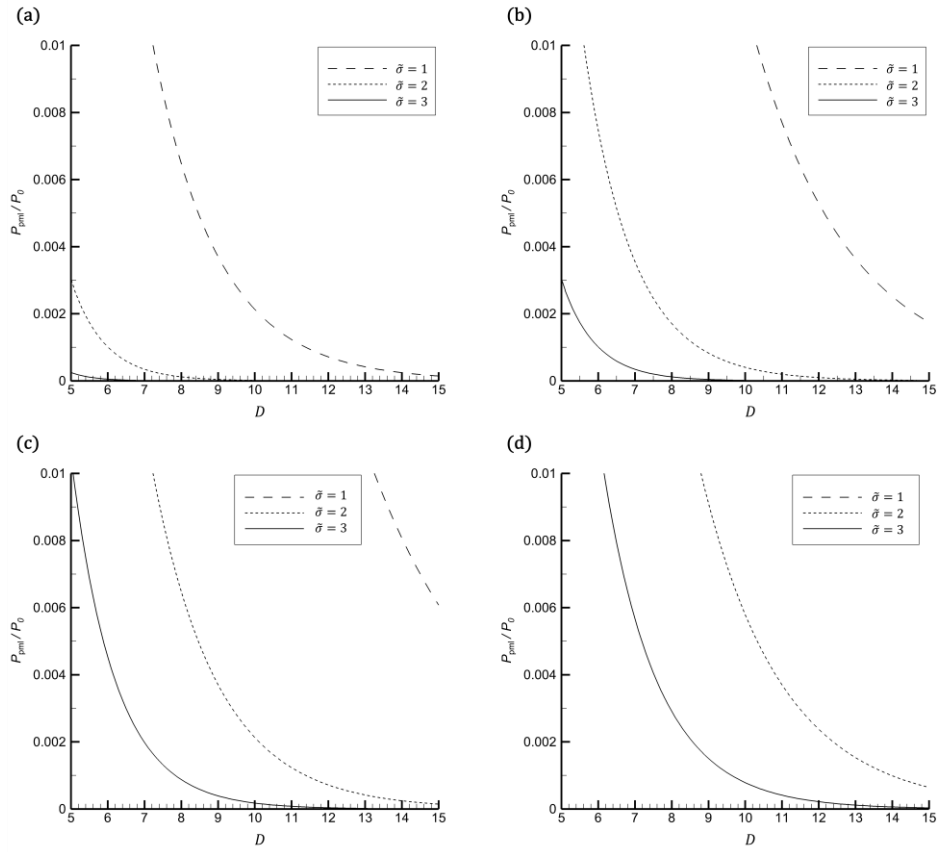


Fig. 4. 6 Pressure value at the end point of the PML domain for linear (a), square (b), cubic (c) and quartic (d) absorption profiles.

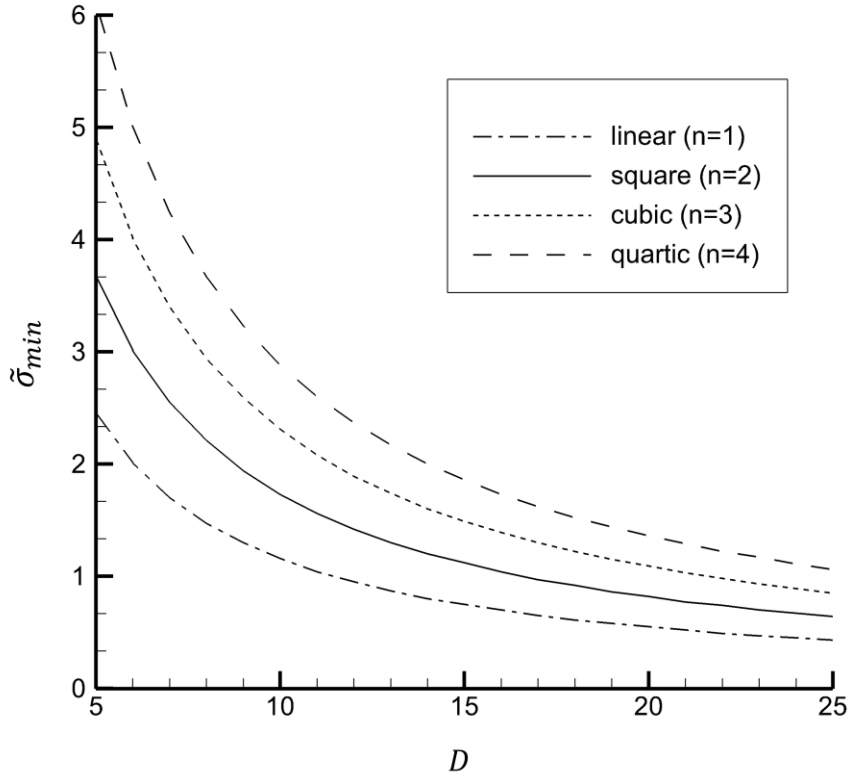


Fig. 4. 7 The minimum absorption coefficients.

Now we can combine the results of the maximum and minimum absorption coefficients in order to deduce the proper range of absorption coefficient in the PML domain. By superimposing Fig. 4.5 on Fig. 4.7, the non-reflective PML conditions for the absorption profiles can be obtained. The optimum PML width that minimizes the width and the range of absorption coefficients are tabulated in table 2. It is found that the square profile has the minimum PML width. The non-reflective PML condition is when the PML width is larger than optimum width and the absorption coefficient is in between $\tilde{\sigma}_{min}$ and $\tilde{\sigma}_{max}$. In the case $\tilde{\sigma} > \tilde{\sigma}_{max}$, it is called over-damped, and there is a discontinuous effect that brings about a spurious wave at the interface of the Euler and the PML domains. In the case of $\tilde{\sigma} < \tilde{\sigma}_{min}$, it is called under-damped, and the solution is reflected, since it is not fully absorbed in the PML domain. Hence, it is recommended to choose D and $\tilde{\sigma}$ inside the non-reflective condition.

Table 2 Optimum PML conditions for various profiles, $\Gamma(x)$

$\Gamma(x)$	Optimum width, $D_{opt}/\Delta x$	Range of $\tilde{\sigma}$
Linear (n=1)	19	$0.50 \leq \tilde{\sigma} \leq 0.52$
Square (n=2)	13	$1.30 \leq \tilde{\sigma} \leq 1.32$
Cubic (n=3)	16	$1.39 \leq \tilde{\sigma} \leq 1.78$
Quartic (n=4)	18	$1.50 \leq \tilde{\sigma} \leq 1.76$

Chapter 5. Numerical Tests

In order to demonstrate the theoretical approach of stability analysis and effectiveness of optimum width prediction put forward so far, numerical examples of acoustic wave absorption are presented in the PML region with predicted PML width (D), absorption coefficient ($\tilde{\sigma}$) and time-step size (Δt).

Two dimensional linearized Euler equations and PML equations in (2.1) and (2.23) are used as governing equations and solved numerically by a finite difference scheme. In particular, 4th order 7-point central difference scheme is used for the entire domain, combined with null-ghost points introduced in chapter 4.1. As time integration, optimized 4-level time discretization method is used. Acoustic source is decayed in PML domain by gradually varying absorption coefficient that is,

$$\sigma_x = \tilde{\sigma}(1 - M^2)\left(\frac{x - \delta_0}{D}\right)^n, \quad \sigma_y = \tilde{\sigma}\left(\frac{y - \delta_0}{D}\right)^n, \quad (5.1)$$

where δ_0 and δ_l refer to the point where PML starts and the thickness of PML domain respectively. A factor of $(1 - M^2)$ is included in σ_x since the absorption rate in x-direction is increased by a factor of $1/(1 - M^2)$, which means it will be larger than that in the y-direction for the same $\tilde{\sigma}$. Specifically, n is 2 for entire simulations. Any artificial damping or filter is not applied in the present work. Unless noted otherwise, the Euler domain is initialized with the following Gaussian pulse:

$$p = \rho = \exp\left[(-\ln 2)\frac{x^2 + y^2}{9}\right], \quad u = v = 0. \quad (5.2)$$

5.1 Stability Analysis Results

In order to demonstrate the stability criteria of PML in chapter 3, the wave propagation in a uniform mean flow is tested. In Fig. 5.1, which is the enlarged curves of Fig. 3.4, the maximum absorption coefficients with respect to mean flow are plotted. Cases 1 and 2 are tested for low Mach number, and Cases 3 and 4 are tested for high Mach number mean flow conditions. The Euler domain is discretized by equidistant $[-40,40] \times [-40,40]$ grids, where $\Delta x = \Delta y = 1$ and $20 \Delta x$ more grids are extended further for PML domains.

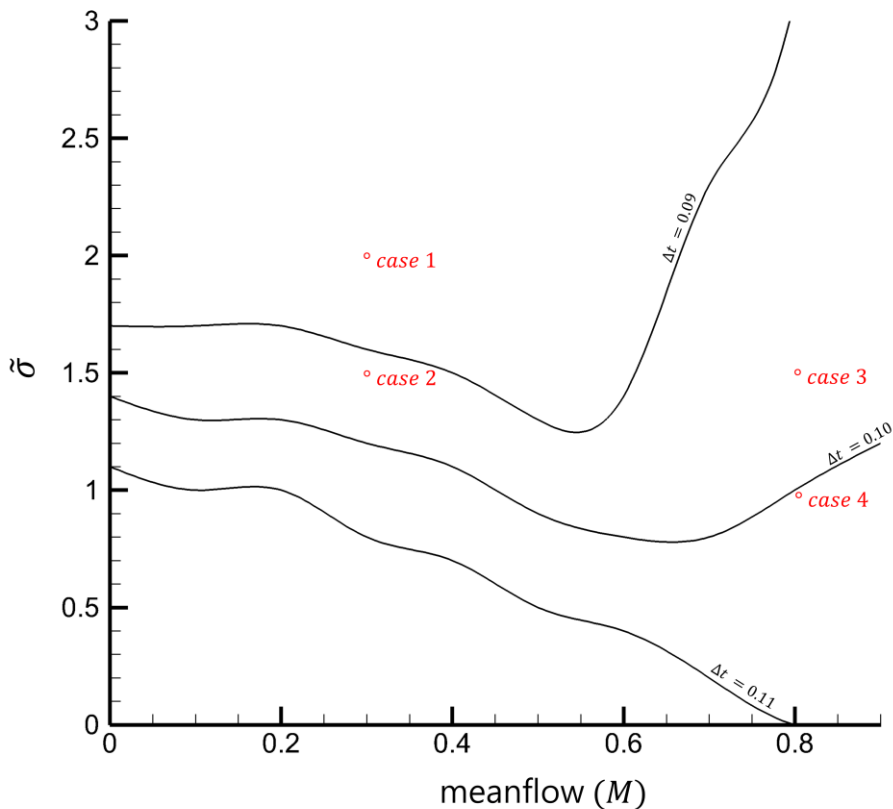


Fig. 5. 1 Region of stability in the complex plane.

5.1.1 Sound Propagating in Low Mach number Uniform Flow

The first example is to show the effect of the absorption coefficient on the stability of PML in low Mach number Uniform flow, $M = 0.3$. We let the time step size $\Delta t = 0.09$ and absorption coefficient of case 1 be $\tilde{\sigma} = 2.0$ while case 2 is $\tilde{\sigma} = 1.5$. According to the stability analysis in Fig. 5.1, the solution of case 1 should diverge while the solution of case 2 should show stable solution. Fig. 5.2 (a) and (b) show the pressure contours of case 1 and 2, respectively. Compared that case 2 shows the stable solution, the spurious waves are detected in the PML domain of case 1.

5.1.2 Sound Propagating in High Mach number Uniform Flow

In the second example, high Mach number Uniform flow, $M = 0.8$ is simulated. Here, we let the time step size be $\Delta t = 0.1$ and absorption coefficient of case 3 be $\tilde{\sigma} = 1.5$ which is higher than the maximum value while case 4 is $\tilde{\sigma} = 1.0$ which is in the stable region from Fig. 5.1. Fig. 5.3 show the pressure contours of case 3 and 4. Compared that case 4 shows the stable solution, the spurious waves are detected in the PML domain of case 3. Thus, it can be said that excellent agreement is observed with the prediction of the time step size.

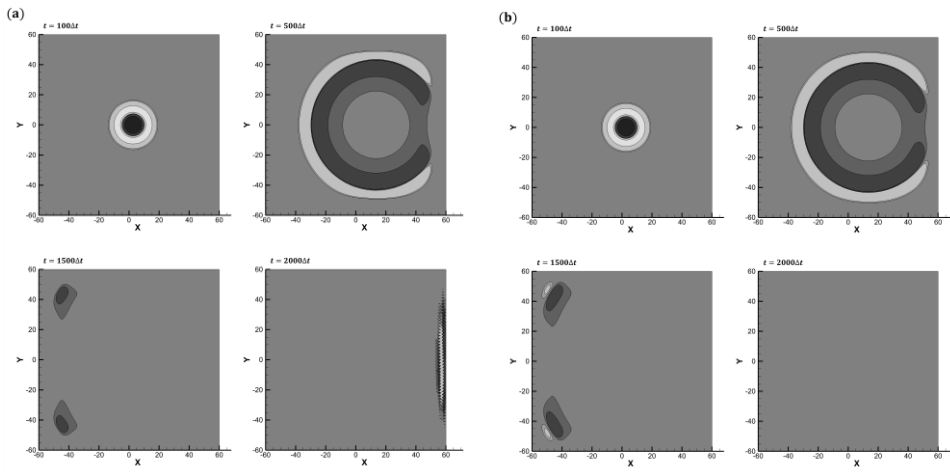


Fig. 5. 2 Pressure contours of case 1 (a) and case 2 (b).

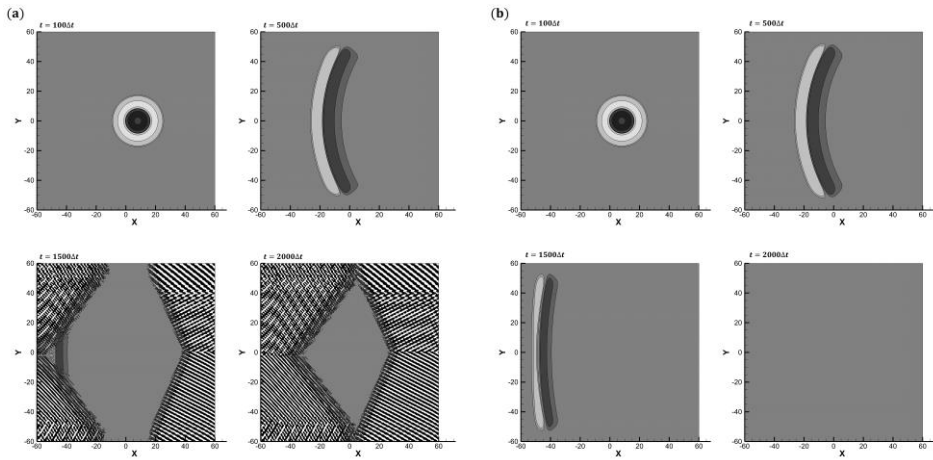


Fig. 5. 3 Pressure contours of case 3 (a) and case 4 (b).

5.2 Accuracy Analysis Results

In order to demonstrate the effectiveness of the optimum-width and absorption coefficient prediction put forward in chapter 4, numerical examples of acoustic wave absorption are presented in the PML domain with a predicted PML width (D) and absorption coefficient ($\tilde{\sigma}$). Simulations are presented in both Cartesian and curvilinear coordinate systems in order to show the effects of absorption coefficients on the performance of PML with the optimum PML width. The simulations are conducted with the square profile in Table 2. For examples of each particular case, over-damped ($\tilde{\sigma} > \tilde{\sigma}_{max}$), under-damped ($\tilde{\sigma} < \tilde{\sigma}_{min}$) conditions and shorter width ($D < D_{opt}$) will be presented.

5.2.1 Sound Propagating in Cartesian Grid System

The wave propagation in a uniform mean flow is tested to validate the optimum PML condition. The Euler domain is discretized by equidistant $[-50,50] \times [-50,50]$ grids, where $\Delta x = \Delta y = 1$ with $D/\Delta x$ more grids extended further for the PML domains and initialized with the following Gaussian pulse:

$$p = \rho = \varepsilon \exp \left[-\frac{(x - x_0)^2 + (y - y_0)^2}{r_0} \right] \quad \text{and } u = v = 0, \quad (5.3)$$

where ε is the pressure perturbation amplitude, $\varepsilon = 1$, r_0 is the characteristic dimension of the pulse, $r_0 = 9/\ln(2)$, and the source position (x_0, y_0) is the centroid of the computational domain. Here, Mach number of the mean flow is $M = 0.5$ and the time step size $\Delta t = 0.05$.

The contour of propagation in the PML domain with square profile at $1000\Delta t$ is shown in Fig. 5.4. The wave is stably absorbed in the PML domain without noticeable reflection at the interface for $\tilde{\sigma} = 1.3$ and $D = 13\Delta x$. Meanwhile, spurious waves are observed in the over-damped ($\tilde{\sigma} = 1.6$) and under-damped ($\tilde{\sigma} = 1.0$) conditions with the same PML width. When the PML width becomes smaller ($D = 10\Delta x$), the solution seems to

be similar to the over-damped case. To further assess the accuracy of optimization as time marches, we plot root mean square error (RMSE) at the position (49,0) in Fig. 5.5. The graph includes four cases of numerical solutions with the reference solution. The reference solution is obtained by using a larger computational domain, so that it is not affected by any boundary effects. It is shown that the RMSE is minimized for $\tilde{\sigma} = 1.3$ and $D = 13\Delta x$ which is the predicted conditions in Table 1.

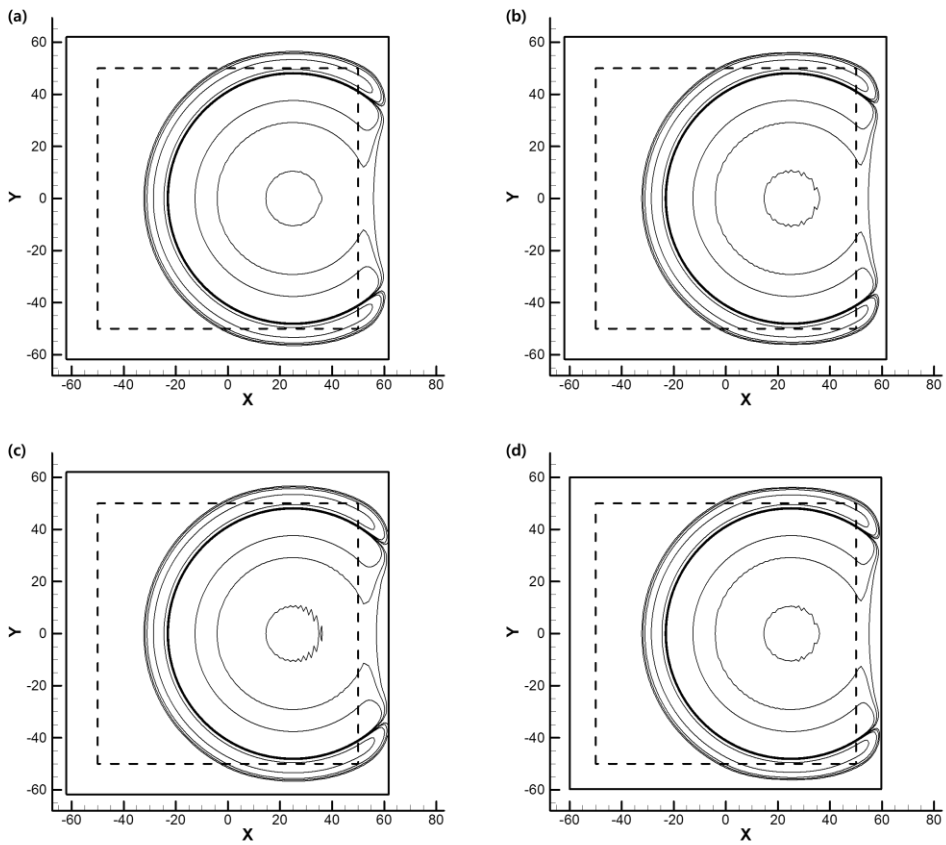


Fig. 5. 4 Contours of the pressure component with the square PML profiles at levels $\pm 0.1, \pm 0.05$, and ± 0.003 . For figures correspond to the PML conditions of $\tilde{\sigma} = 1.3$ (a), $\tilde{\sigma} = 1.6$ (b), $\tilde{\sigma} = 1.0$ (c) with $D = 13\Delta x$ and $\tilde{\sigma} = 1.3$ with $D = 10\Delta x$ (d).

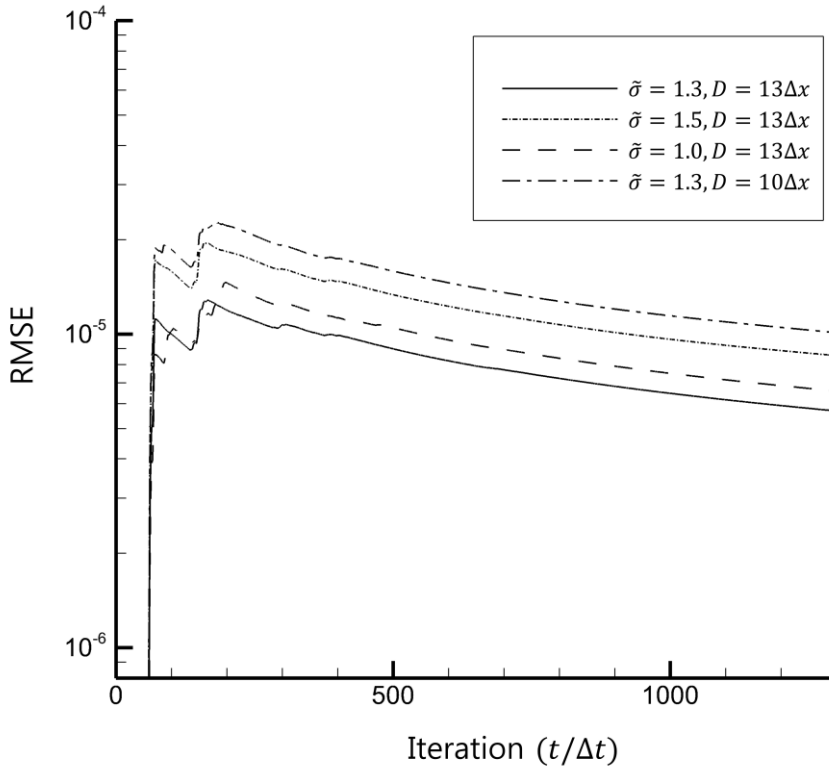


Fig. 5.5 Root mean square error (RMSE) of a Cartesian grid for square PML profiles at (49,0).

5.2.2 Sound Propagating in Curvilinear Grid System

If the computational domain is discretized by curvilinear grids for some particular situations, the PML domain should also be discretized by curvilinear grids accordingly. Thus, we adopt two-dimensional generalized PML equations in Eqs. (2.24) and (2.25). The boundary conditions are described in Fig. 5.6. A detailed analysis of the reflection of acoustic wave from a cylinder wall using solid wall boundary condition by a ghost values has been carried out by Tam and Dong [40]. Since the configuration is symmetric, only the upper half of the domain is considered, and symmetry boundary conditions are

invoked along $\theta = 0^\circ$ and 180° . The dimension of the used computational grid is 50×360 , where $\Delta\xi = \Delta\eta = 1$ with $D/\Delta x$ more grids extended further for the PML domains. The mesh shown in Fig. 5.6 is generated analytically according to the expression:

$$\begin{aligned} r(i) &= x_{min} + \Delta\xi(i - 1) \\ x(i, j) &= r(i)\cos\left(\frac{\pi}{360}j\Delta\eta\right) \\ y(i, j) &= r(i)\sin\left(\frac{\pi}{360}j\Delta\eta\right), \end{aligned} \quad (5.4)$$

where x_{min} determines the diameter of the cylinder and $x_{min} = 20\Delta\xi$ in the simulation.

First, the Gaussian pulse of Eq. (5.3) centered at $(x, y) = (60, 0)$ is initialized without mean flow in the physical domain and the time step size $\Delta t = 0.04$. In Fig. 5.7, an example of the wave propagation in the PML domain with square profiles at $2300\Delta t$ is shown. The wave is stably absorbed in the PML domain without noticeable reflection at the interface for $\tilde{\sigma} = 1.3$ and $D = 13\Delta x$, which is the optimum value in Table 1. Similar to the examples in a Cartesian coordinate system, spurious waves are observed in the over-damped ($\tilde{\sigma} = 1.6$), under-damped ($\tilde{\sigma} = 1.0$) and smaller width ($D = 10\Delta x$) conditions. Root mean square error (RMSE) at the position $(x, y) = (122, 0)$ of numerical solutions for each condition and the reference solution are plotted in Fig. 5.8. It is shown that the RMSE is still minimized for $\tilde{\sigma} = 1.3$ and $D = 13\Delta x$ for curvilinear grid system.

In the second example, we solve the Euler equations with the following source term added to Eq. (5.3):

$$p = \rho = \varepsilon \sin(\Omega t) \exp\left[-\frac{(x - x_0)^2 + (y - y_0)^2}{r_0}\right]. \quad (5.5)$$

Here, the frequency of the source is $\Omega = 0.05\pi$ and other conditions are the same as previous example. The square absorption profile is adopted for this time. Fig. 5.9 shows the pressure contours of the numerical simulation at $t = 5000\Delta t$. The differences

between the numerical and exact solutions [41] along the line $y = 0$ are plotted in Fig. 5.10. Clearly, these two results show that the prediction of accuracy at the interface of the PML domain works well for Gaussian pulse propagation in the curvilinear coordinate system as well.

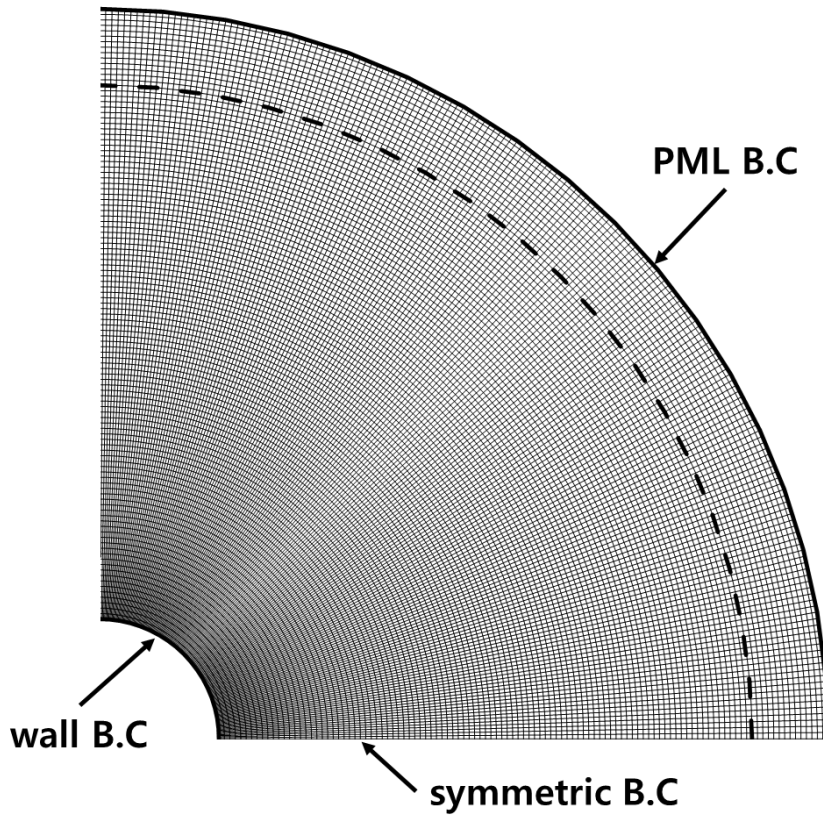


Fig. 5. 6 A curvilinear grid structure with boundary conditions.

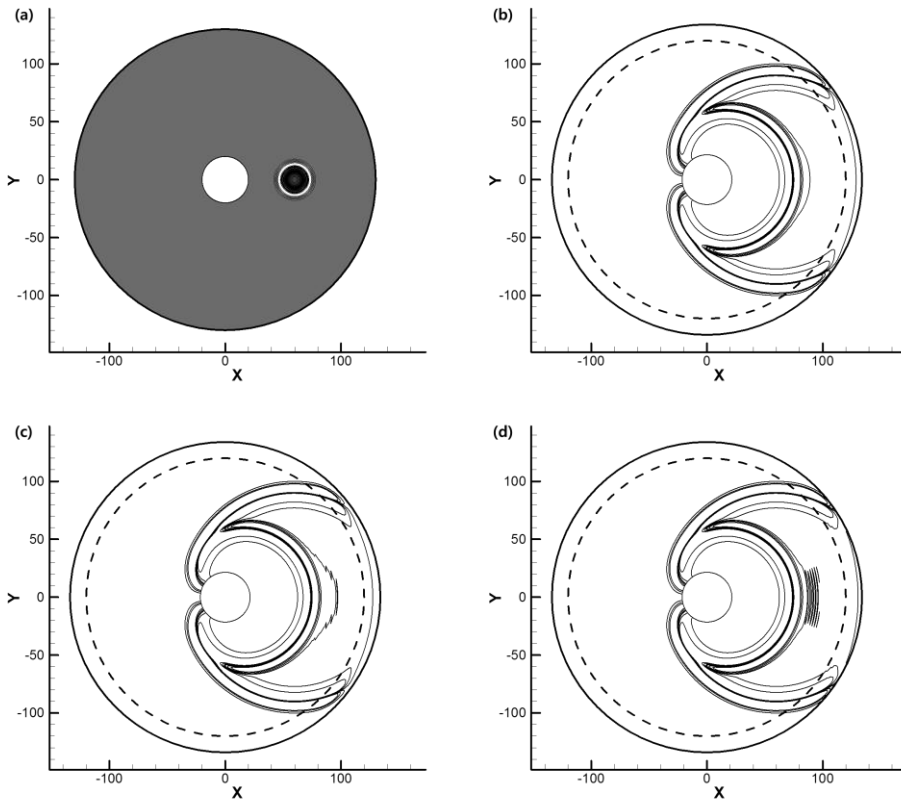


Fig. 5. 7 Contours of the pressure component with the square PML profiles at levels ± 0.1 , ± 0.05 , and ± 0.003 . For figures correspond to the PML conditions of $\tilde{\sigma} = 1.3$ (a), $\tilde{\sigma} = 1.6$ (b), $\tilde{\sigma} = 1.0$ (c) with $D = 13\Delta x$ and $\tilde{\sigma} = 1.3$ with $D = 10\Delta x$ (d).

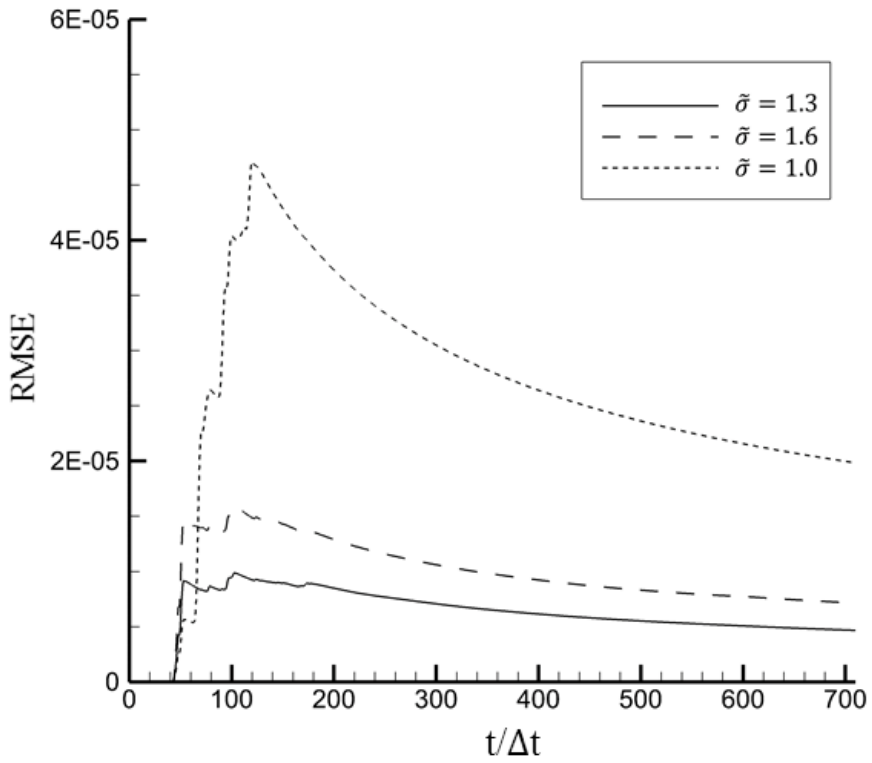


Fig. 5. 8 Root mean square error (RMSE) of pressure in a curvilinear grid for square PML profile at (122,0).

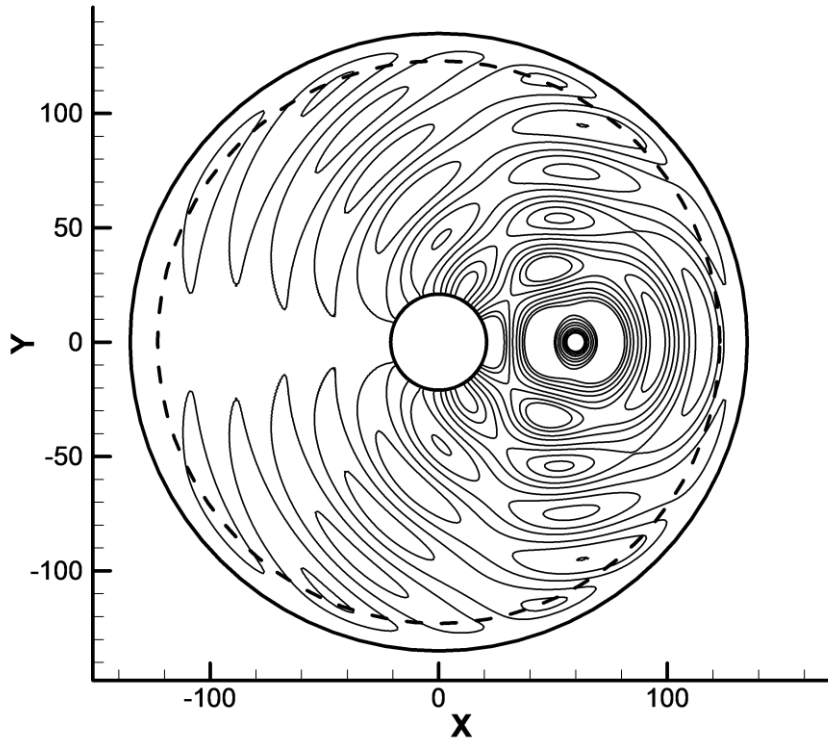


Fig. 5.9 Contours of the sinusoidal wave propagation with the square PML profiles at levels ± 1.0 , ± 0.5 , ± 0.1 , and ± 0.05 .

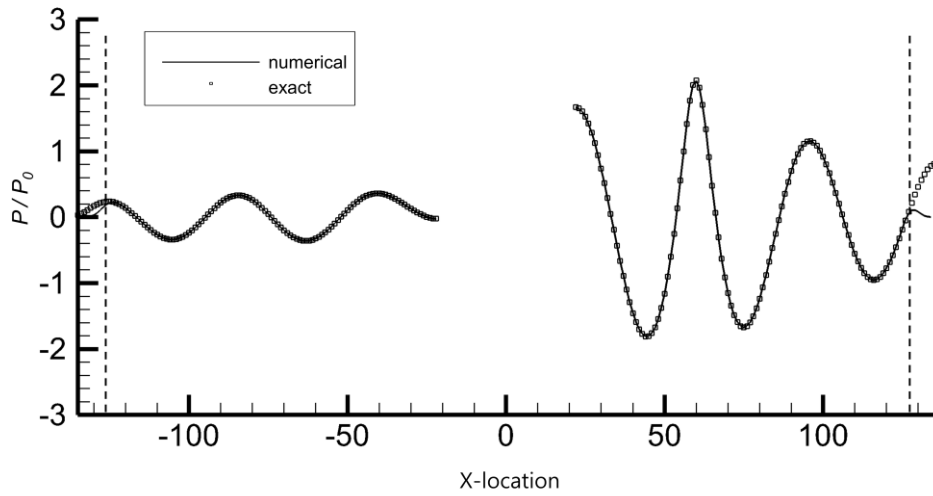


Fig. 5. 10 Solutions of the scattered acoustic field along the line at $y=0$.

Chapter 6. Concluding Remarks

The numerical stability analysis on PML equation by manipulating the dispersion relation of PML equation was discussed. First, we derived the complex stability diagram of particular time integration scheme. Second, the maximum physical root of dispersion relation was found by considering the maximum wavenumber of spatial discretization scheme. Finally, by comparing this two results, the time step limitation was achieved that can ensure the dispersion relation preserving property as well as the convergence. In addition to the stability criteria, we also dealt with the optimum PML width and its corresponding absorption coefficient in order to minimize the computational cost while satisfying the accuracy. In the computational tests reported here, suggested PML width and time step obtained from stability criteria showed a good agreement in the simulation. It was further showed that the stability analysis could also be applied in case of generalized coordinate as well. The proposed stability analysis is expected to be extended to the non-linear PML governing equations in future works.

References

1. Hardin, J. C., and J. R. Ristorcelli. "ICASE/LaRC Workshop on Benchmark Problems in Computational Aeroacoustics." National Aeronautics and Space Administration (1994).
2. Hixon, Ray. "Evaluation of a high-accuracy MacCormack-type scheme using benchmark problems." *Journal of Computational Acoustics* 6.03 (1998): 291-305.
3. Lin, San-Yih, and Yan-Shin Chin. "Comparison of higher resolution Euler schemes for aeroacoustic computations." *AIAA journal* 33.2 (1995): 237-245.
4. Zhuang, M., and R. F. Chen. "Applications of high-order optimized upwind schemes for computational aeroacoustics." *Aiaa Journal* 40.3 (2002): 443-449.
5. Harten, Ami, and Stanley Osher. "Uniformly high-order accurate nonoscillatory schemes. I." *SIAM Journal on Numerical Analysis* 24.2 (1987): 279-309.
6. Ko, D. K., and D. J. Lee. "Development of an efficient fourth-order non-oscillatory scheme for compressible flows." (1998).
7. Shu, Chi-Wang. *Essentially non-oscillatory and weighted essentially non-oscillatory schemes for hyperbolic conservation laws*. Springer Berlin Heidelberg, 1998.
8. Shu, Chi-Wang. *Essentially non-oscillatory and weighted essentially non-oscillatory schemes for hyperbolic conservation laws*. Springer Berlin Heidelberg, 1998.
9. Chang, Sin-Chung. "The method of space-time conservation element and solution element—a new approach for solving the Navier-Stokes and Euler equations." *Journal of computational Physics* 119.2 (1995): 295-324.
10. Stanescu, D., et al. "Multidomain spectral computations of sound radiation from ducted fans." *AIAA journal* 37.3 (1999): 296-302.
11. Lele, Sanjiva K. "Compact finite difference schemes with spectral-like resolution." *Journal of computational physics* 103.1 (1992): 16-42.
12. Tam, Christopher Kw, and Jay C. Webb. "Dispersion-relation-preserving schemes

- for computational aeroacoustics." DGLR/AIAA Aeroacoustics Conference, 14 th, Aachen, Germany. 1992.
13. Berenger, Jean-Pierre. "A perfectly matched layer for the absorption of electromagnetic waves." *Journal of computational physics* 114.2 (1994): 185-200.
 14. Hu, Fang Q. "On absorbing boundary conditions for linearized Euler equations by a perfectly matched layer." *Journal of Computational Physics* 129.1 (1996): 201-219.
 15. Hu, Fang Q. "On perfectly matched layer as an absorbing boundary condition." *AIAA paper* (1996): 96-1664.
 16. Abarbanel, S., D. Gottlieb, and Jan S. Hesthaven. "Well-posed perfectly matched layers for advective acoustics." *Journal of Computational Physics* 154.2 (1999): 266-283.
 17. Whitham, Gerald Beresford. *Linear and nonlinear waves*. Vol. 42. John Wiley & Sons, 2011.
 18. Hu, Fang Q. "A stable, perfectly matched layer for linearized Euler equations in unsplit physical variables." *Journal of Computational Physics* 173.2 (2001): 455-480.
 19. Hagstrom, Thomas, and Igor Nazarov. "Absorbing layers and radiation boundary conditions for shear flow calculations." *AIAA paper* 3298 (2003): 2003.
 20. Hu, Fang Q. "A perfectly matched layer absorbing boundary condition for linearized Euler equations with a non-uniform mean flow." *Journal of Computational Physics* 208.2 (2005): 469-492.
 21. Meza-Fajardo, Kristel C., and Apostolos S. Papageorgiou. "A nonconvolutional, split-field, perfectly matched layer for wave propagation in isotropic and anisotropic elastic media: stability analysis." *Bulletin of the Seismological Society of America* 98.4 (2008): 1811-1836.
 22. Savadatti, Siddharth, and Murthy N. Guddati. "Absorbing boundary conditions for scalar waves in anisotropic media. Part 1: Time harmonic modeling." *Journal of Computational Physics* 229.19 (2010): 6696-6714.
 23. Parrish, Sarah A., and Fang Q. Hu. "PML absorbing boundary conditions for the

- linearized and nonlinear Euler equations in the case of oblique mean flow." *International journal for numerical methods in fluids* 60.5 (2009): 565-589.
24. Nataf, Frédéric. "A new approach to perfectly matched layers for the linearized Euler system." *Journal of Computational Physics* 214.2 (2006): 757-772.
 25. Hu, Fang Q. "Development of PML absorbing boundary conditions for computational aeroacoustics: A progress review." *Computers & Fluids* 37.4 (2008): 336-348.
 26. Velu, Srinivasa Perumal, and Klaus A. Hoffmann. Development and application of perfectly matched layer for numerical boundary treatment. Diss. Wichita State University, College of Engineering, Department of Aerospace Engineering., (2010).
 27. Chew, Weng Cho, and William H. Weedon. "A 3D perfectly matched medium from modified Maxwell's equations with stretched coordinates." *Microwave and optical technology letters* 7.13 (1994): 599-604.
 28. Collino, Francis, and Peter Monk. "The perfectly matched layer in curvilinear coordinates." *SIAM Journal on Scientific Computing* 19.6 (1998): 2061-2090.
 29. Bayliss, Alvin, and Eli Turkel. "Radiation boundary conditions for wave-like equations." *Communications on Pure and applied Mathematics* 33.6 (1980): 707-725.
 30. Hariharan, S. I., J. R. Scott, and K. L. Kreider. "A potential-theoretic method for far-field sound radiation calculations." *Journal of Computational Physics* 164.1 (2000): 143-164.
 31. Tam, Christopher KW. "Computational aeroacoustics: an overview of computational challenges and applications." *International Journal of Computational Fluid Dynamics* 18.6 (2004): 547-567.
 32. Wang, J. L., et al. "Explicit High Accuracy Maximum Resolution Dispersion Relation Preserving Schemes for Computational Aeroacoustics."
 33. Cunha, G., and S. Redonnet. "On the effective accuracy of spectral-like optimized finite-difference schemes for computational aeroacoustics." *Journal of*

- Computational Physics 263 (2014): 222-232.
34. Tam, Christopher KW. Computational aeroacoustics: A wave number approach. Vol. 33. Cambridge University Press, 2012.
 35. Gary, John. "On boundary conditions for hyperbolic difference schemes." *Journal of Computational Physics* 26.3 (1978): 339-351
 36. Li, Yuguo. "Wavenumber-extended high-order upwind-biased finite-difference schemes for convective scalar transport." *Journal of Computational Physics* 133.2 (1997): 235-255
 37. Zhou, D., et al. "The perfectly matched layer boundary condition for scalar finite-difference time-domain method." *Photonics Technology Letters, IEEE* 13.5 (2001): 454-456.
 38. Chew, Weng Cho, and William H. Weedon. "A 3D perfectly matched medium from modified Maxwell's equations with stretched coordinates." *Microwave and optical technology letters* 7.13 (1994): 599-604.
 39. Agrawal, Arti, and Anurag Sharma. "Perfectly matched layer in numerical wave propagation: factors that affect its performance." *Applied optics* 43.21 (2004): 4225-4231.
 40. Tam, Christopher KW, and Zhong Dong. "Wall boundary conditions for high -order finite -difference schemes in computational aeroacoustics." *Theoretical and Computational Fluid Dynamics* 6.5 -6 (1994): 303 -322.
 41. Morris, Philip J. "Scattering of sound from a spatially distributed, spherically symmetric source by a sphere." *The Journal of the Acoustical Society of America* 98.6 (1995): 3536 -3539.

전산공력음향학에서 Perfectly Matched Layer의 안정적인 흡수조건에 관한 연구

서울대학교 대학원

우주항공공학과

정한아침

국문초록

전산공력음향학에서 유출 및 방사 경계조건은 전체 해석결과에 영향을 미칠 수 있다는 면에서 매우 중요하다고 할 수 있다. 이러한 유출 및 방사 경계조건 중 전산전자기학 및 전산공력음향학에서 널리 사용되고 있는 흡수경계조건은 Perfectly Matched Layer(PML)으로, 해석영역의 지배방정식에 흡수계수에 의한 추가적인 항을 더하여 해석영역과 경계영역 사이에서 안정적으로 파동을 흡수할 수 있다. 또한 시간-공간 변환을 통해 음향파의 특성상 기존 PML 조건에서 발생한 다양한 유동조건에서 위상속도(phase velocity)와 군속도(group velocity) 방향의 변화 문제가 해결되었다. 하지만 실제 이산화된 해석영역에서 해석적으로 안정적인 PML 방정식은 시간 및 공간 차분간격과 유동속도 및 흡수계수 변화에 따라 수치적인 불안정성을 발생하는 문제를 갖게 된다.

본 논문에서는 이러한 수치적인 불안정성에 미치는 요인들을 실제 수치기법을 적용하여 연구하였다. 먼저 시간차분간격(time step size)을 위해 PML 방정식의 이산관계(dispersion relation) 관점에서 수치적으로 안정적인 해석

조건을 도출하였다. 또한 유동속도에 따라 PML 영역에서 안정적인 흡수계수 범위 및 최적 너비를 수학적 접근을 통하여 제시하였다. 예측결과를 확인하기 위해 다양한 유동조건뿐 아니라 일반 격자계에서 해석을 진행함으로써 유동속도 및 격자간격의 변화에 따른 시간간격과 흡수계수 및 PML 너비 예측의 정확성을 검증하였다. 이를 통하여 기존에 실험적인 방법에만 의존했던 PML의 해석조건에 대해 차분간격, 유동속도 그리고 흡수계수의 상관관계를 분석하여 PML 해석조건을 예측했다는 점에서 중요한 가치가 있다고 판단된다.

주요 용어: 고해상도 유한차분 (High-order Finite Difference), 이산관계 (Dispersion Relation), 안정성 분석(Stability Analysis), 전산공력음향학 (Computational Aeroacoustics), Perfectly Matched Layer(PML), 이산관계 (Dispersion Relation)

학번 : 2014-20665